공학박사학위논문

# Synthesis and Characterization of Proton Exchange Membranes with Enhanced Hydrophilic-hydrophobic Nanophase Separation

## 친수성-소수성 나노상분리의 향상을 위한 양이온 교환막의 합성에 관한 연구

2023년 2월

서울대학교 대학원

화학생물공학부

안 수 민

# 친수성-소수성 나노상분리의 향상을 위한 양이온 교환막의 합성에 관한 연구

# Synthesis and Characterization of Proton Exchange Membranes with Enhanced Hydrophilic-hydrophobic Nanophase Separation

지도교수 이 종 찬 박사
이 논문을 공학박사학위 논문으로 제출함.
2023년 2월
서울대학교 대학원
화학생물공학부
안 수 민

심민지의 박사학위논문을 인준함.
2023년 2월

| | | |
|---|---|---|
| 위원장 | 오 준 학 | (인) |
| 부위원장 | 이 종 찬 | (인) |
| 위 원 | 유 동 원 | (인) |
| 위 원 | 김 태 호 | (인) |
| 위 원 | 손 은 호 | (인) |

# Synthesis and Characterization of Proton Exchange Membranes with Enhanced Hydrophilic-hydrophobic Nanophase Separation

by

**Su Min Ahn**

**Adviser: Professor Jong-Chan Lee, Ph. D.**

**Submitted in Partial Fulfillment**
**of the Requirements for the Degree of**
**DOCTOR OF PHILOSOPHY**

**February, 2023**

**School of Chemical and Biological Engineering**
**College of Engineering**
**Graduate School**
**Seoul National University**

# Abstract

This study presents the synthesis of hydrocarbon-based proton exchange membranes with enhanced hydrophilic-hydrophobic nanophase separation for proton exchange membrane fuel cell and water electrolysis. Firstly, a multiblock copolymer containing a highly sulfonated poly(phenylene sulfide sulfone) hydrophilic oligomer and a partially fluorinated perfluorocyclobutyl (PFCB)-containing hydrophobic oligomer was synthesized. The sharp contrast between the hydrophilic and hydrophobic moieties induced a well-developed phase separation, which was observed in the transmission electron microscopy images within the polymer electrolyte membrane (PEM). The increased chain mobility from the flexible ether and PFCB groups afforded facile thermal annealing of the membrane. Thermal annealing induced polymer chain packing of the hydrophobic moieties, enhancing the hydrophilic/hydrophobic phase separation. The fabricated membranes exhibited higher proton conductivity compared with those of conventional hydrocarbon PEM possessing a random copolymer architecture, while their dimensional swelling was suppressed. Additionally, under low humidification (a relative humidity (RH) of 50%), the sulfonated–fluorinated membrane achieved a high proton conductivity of up to 41.9 mScm$^{-1}$. A high adhesion strength of 32.7 mNcm$^{-1}$ was also observed, indicating strong interfacial compatibility in the membrane electrode assembly due to its structural affinity for the contacting perfluorosulfonated binder. The enhanced hydrophilic/hydrophobic phase separations facilitated fuel cell performances of 1.13 and 0.61 $Acm^{-2}$ at 0.6 V and 65 °C under 100% and 50% RH conditions, respectively, in addition to achieving stable chemical and physical durabilities.

Secondly, aromatic graft polymer was synthesized for proton exchange membrane by grafting a highly sulfonated poly(phenylene sulfide sulfone) side chain onto a poly(arylene ether sulfone) main chain, thus creating a phase-separated morphology with narrow and co-continuous channels of small hydrophilic ion domains. The unique morphology of the graft PEM induced low hydrogen permeability owing to the restricted domain size, while maintaining high proton conductivity owing to the well-connected hydrophilic channels. Along with durable dimensional, mechanical, and thermo-hydrolytic stabilities, the graft PEM showed effective properties for PEM water electrolysis (PEMWE). The graft PEM afforded a PEMWE performance of 5,329 mA $cm^{-2}$ at 1.9 V, which was 1.88-fold higher than that of Nafion 212, and showed a durable performance without loss for 50 h at a high current density (1,000 mA $cm^{-2}$).

Finally, investigation on structure-property relationship for a series of versatile graft PEMs was conducted for fuel cell and water electrolysis applications. The side chain length and the branching point of the main chain induced different morphology of hydrophilic-hydrophobic nanophase separation, where larger hydrophilic domain size was observed with increased side-chain length. The morphological difference induced distinct properties (water sorption behavior, proton transport behavior, and hydrogen permeability) among graft PEMs with different side chain length. Moreover, the effects of side-chain length and the branching point of the main chain were studied on the properties of PEMs under reduced humidification for fuel cell application and immersion in water at high temperature for water electrolysis application. From these results, we could speculate that short side-chain graft would be favorable in fuel cell due to high proton conductivity at reduced humidification, and long side-chain graft would be favorable to water electrolysis due to reduced swelling and permeability at high-temperature immersion.

**Keywords:** Proton exchange membrane, Hydrophilic-hydrophobic phase separation, Proton exchange membrane fuel cell, Proton exchange membrane water electrolysis, Multiblock copolymer, Graft copolymer

**Student Number:** 2018-32408

# Table of Contents

# Chapter 1

# Introduction

# Chapter 2

# Perfluorocyclobutyl-containing multiblock copolymers to induce enhanced hydrophilic/hydrophobic phase separation and high proton conductivity at low humidity

# Chapter 3

# Design of highly sulfonated aromatic graft polymer with very high proton conductivity and low hydrogen permeability for water electrolysis

# Chapter 4

# Structure-property relationship of versatile aromatic graft proton exchange membrane for fuel cell and water electrolysis

# List of Tables

# List of Figures

# Chapter 1

# Introduction

## 1.1. Proton exchange membrane for fuel cell and water electrolysis

Future hydrogen society employs proton exchange membrane fuel cell (PEMFC) and water electrolysis (PEMWE) for generating electricity and producing hydrogen gas [1]. PEMFC converts chemical energy of a fuel such as hydrogen and an oxidizing agent such as oxygen into electrical energy through redox reaction with water as a byproduct, while PEMWE converts electricity and water into hydrogen and oxygen. Research on PEMFC for fuel cell vehicles have been widely investigated due to their high power densities, good energy conversion efficiencies, and zero-emission levels [2]. Although not as extensive as the PEMFC, research on PEMWE have been reported for future sustainable hydrogen production owing to its inherently high power and compactness, high operational capability under differential pressure, production of pure hydrogen, and fast response to load changes [3]. Both PEMFC and PEMWE utilize proton exchange membrane (PEM), which is the key material for both of the applications, conducting proton and separating gas [4]. Proton exchange membrane (PEM), the key material in PEMWE, requires high proton conductivity ($\sigma$) and low gas permeability to promote proton transport and prevent gas mixing [4]. PEM also requires mechanical strength, dimensional, thermal, and chemical stability [5]. Despite the utilization of commercial perfluorosulfonated Nation for its dimensional and chemical stability, low hydrogen barrier property, low thermal stability, high cost, and detrimental environmental effects hinders the usage for the future hydrogen society [6].

## 1.2. Sulfonated aromatic hydrocarbon proton exchange membrane

Sulfonated aromatic hydrocarbon-PEMs with ion-exchanging sulfonic acid groups have been developed as an alternative to Nafion to reduce the production cost, to increase the thermal stability, and to increase the hydrogen barrier property [7]. The amphiphilic nature of PEM induces a hydrophilic/hydrophobic phase separation, where the proton is transported through hydrophilic channels [8]. The phase separation between the sulfonated hydrophilic moieties and the hydrophobic moieties induce well-connected proton-conducting channels, affecting not only the proton conductivity but also the hydrogen permeability and the dimensional stability [8]. Therefore, an optimized design of hydrophilic-hydrophobic phase separation morphology should be studied to create a durable and efficient PEM applied for PEMFC and PEMWE.

Previously, research on random copolymers, such as sulfonated polyimide (SPI) [9, 10], sulfonated poly(arylene ether sulfone) (SPAES) [11], and sulfonated poly(ether ether ketone) (SPEEK) [12, 13], have demonstrated their effective proton conductions under high humidity conditions. However, due to their insufficient hydrophilic aggregations compared with those of Nafion, random copolymers display inadequate proton conductivity under low humidification [14].

Therefore, to induce sufficient proton conductivity in well-connected proton-conducting channels under wide range of humidification, well-developed phase separation of the hydrophilic and hydrophobic moieties of hydrocarbon PEMs must be achieved [15].

One approach to enhance the phase separation is to develop multiblock copolymers, in which the hydrophilic and hydrophobic blocks are placed next to each other, thus densely arranging the sulfonic acid groups together [16]. Multiblock copolymers containing different hydrophobic and hydrophilic blocks, which incorporated different structural groups, including SPI [17, 18], SPAES [19, 20], and SPEEK [21, 22], have been reported to improve proton conductivity even under low humidity conditions. Another approach is to enhance the phase separation level by augmenting the acidities and densities of the hydrophilic components [23]. Kreuer et al. fabricated highly sulfonated poly(phenylene sulfone) polymers with high acidic density, where high proton conductivity at a high temperature and low humidity was achieved [24].

Despite the improvement in proton conductivity, multiblock copolymer with enlarged hydrophilic domain has been reported to show higher hydrogen permeability compared to the random analog [25]. Although hydrogen permeation occurs in both the hydrophilic and hydrophobic domains of PEM, hydrogen permeates through the water-bearing hydrophilic domains with lower activation energy [26, 27]. Therefore, designing the PEM morphology by promoting high proton conductivity, while maintaining low hydrogen permeability should be investigated.

## 1.3. Motivation

The development of hydrocarbon PEMs have showed advantages in improving proton conductivity and lowering hydrogen permeability. However, further research on balancing the dimensional property and mechanical stability without compromising the proton conductivity and the hydrogen permeability is needed. Enhancement and optimization of hydrophilic-hydrophobic nanophase separation in PEMs are essential for practical and durable operation in PEMFC and PEMWE.

Enhancement of phase separation by increasing the hydrophilicity has been reported to be effective in multiblock copolymers. However, there are only a few research on improving their hydrophobicity [8]. The presence of hydrophobic fluorocarbons in PEMs leads to thermal, mechanical, and chemical stabilities compared with that of hydrocarbons, in addition to the enhancement of the hydrophilic/hydrophobic phase separation [28, 29]. Therefore, a sulfonated–fluorinated multiblock copolymer was developed containing perfluorocyclobutyl (PFCB) and highly sulfonated poly(phenylene sulfide sulfone) moieties as the hydrophobic and hydrophilic oligomers, respectively. The flexible PFCB group facilitated high hydrophobic aggregation, which induced intense phase separation and increased the proton conductivity, even under low humidification. The multiblock copolymer coupled with the super-hydrophilic oligomer generated a well-developed nanophase separation. The cast membrane was subjected to additional thermal annealing treatment to maximize the hydrophilic/hydrophobic phase separations. The partially fluorinated hydrophobic oligomer achieved interfacial compatibility with the Nafion binder in the electrode layer, which imparted the fabricated membrane electrode assembly with reasonable fuel cell performance and durability.

Designing a hydrophilic channel morphology to balance the trade-off between the proton conductivity and the hydrogen permeability is the key to achieving a PEMWE with efficient performance, durability, and safety. We developed a fully aromatic comb-shaped graft PEM applied to PEMWE. Despite its potential for effective morphology in PEMWE, application of fully aromatic graft PEM was reported none for PEMWE and only few for PEMFC due to limited structural design and unwanted crosslinking reaction [30-32]. The graft architecture resembled Nafion, wherein a highly sulfonated side chain was grafted to the hydrophobic main chain, inducing unique and distinct nanophase separation interconnected with hydrophilic domains of restricted size. This morphology proved effective for PEMWE, resulting in a very high proton conductivity and low hydrogen permeability. The balanced property of graft PEM displayed superior mechanical, dimensional, and thermo-hydrolytic stability, resulting in an outstanding PEMWE performance.

The developed aromatic graft PEM was investigated for the structure-property relationship by varying the side chain length and the branching point. Side chain with different lengths were employed to produce graft PEMs of various ion exchange capacities by adjusting the percentage of branching point of the main chain. The variation of side chain length and branching point affected the morphology, producing different behaviors on water uptake, dimensional change, proton conductivity, and hydrogen permeability. The graft PEM with short side chain showed higher proton conductivity at reduced humidity, while the graft PEM with long side chain showed excellent properties at hot-water immersed condition. The structural versatility of graft PEM provides a possible outlook for creating an optimized PEM for targeted properties.

## 1.4. References

[1] J.M. Thomas, P.P. Edwards, P.J. Dobson, G.P. Owen, Decarbonising energy: The developing international activity in hydrogen technologies and fuel cells, Journal of Energy Chemistry, 51 (2020) 405-415.

[2] N. Li, D.W. Shin, D.S. Hwang, Y.M. Lee, M.D. Guiver, Polymer Electrolyte Membranes Derived from New Sulfone Monomers with Pendent Sulfonic Acid Groups, Macromolecules, 43 (2010) 9810-9820.

[3] C.V. Pham, D. Escalera-López, K. Mayrhofer, S. Cherevko, S. Thiele, Essentials of High Performance Water Electrolyzers – From Catalyst Layer Materials to Electrode Engineering, Advanced Energy Materials, 11 (2021) 2101998.

[4] H. Nguyen, C. Klose, L. Metzler, S. Vierrath, M. Breitwieser, Fully Hydrocarbon Membrane Electrode Assemblies for Proton Exchange Membrane Fuel Cells and Electrolyzers: An Engineering Perspective, Advanced Energy Materials, 12 (2022) 2103559.

[5] Y. Wang, Y. Pang, H. Xu, A. Martinez, K.S. Chen, PEM Fuel cell and electrolysis cell technologies and hydrogen infrastructure development – a review, Energy & Environmental Science, 15 (2022) 2288-2328.

[6] Y.S. Kim, Polymer Electrolytes with High Ionic Concentration for Fuel Cells and Electrolyzers, ACS Applied Polymer Materials, 3 (2021) 1250-1270.

[7] M. Adamski, N. Peressin, S. Holdcroft, On the evolution of sulfonated polyphenylenes as proton exchange membranes for fuel cells, Materials Advances, 2 (2021) 4966-5005.

[8] D.W. Shin, M.D. Guiver, Y.M. Lee, Hydrocarbon-Based Polymer Electrolyte Membranes: Importance of Morphology on Ion Transport and Membrane Stability, Chemical Reviews, 117 (2017) 4759-4805.

[9] J. Fang, X. Guo, S. Harada, T. Watari, K. Tanaka, H. Kita, K.-i. Okamoto, Novel Sulfonated Polyimides as Polyelectrolytes for Fuel Cell Application. 1. Synthesis, Proton Conductivity, and Water Stability of Polyimides from 4,4‘-Diaminodiphenyl Ether-2,2‘-disulfonic Acid, Macromolecules, 35 (2002) 9022-9028.

[10] Z. Hu, Y. Yin, S. Chen, O. Yamada, K. Tanaka, H. Kita, K.-I. Okamoto, Synthesis and properties of novel sulfonated (co)polyimides bearing sulfonated aromatic pendant groups for PEFC applications, Journal of Polymer Science Part A: Polymer Chemistry, 44 (2006) 2862-2872.

[11] F. Wang, M. Hickner, Y.S. Kim, T.A. Zawodzinski, J.E. McGrath, Direct polymerization of sulfonated poly(arylene ether sulfone) random (statistical) copolymers: candidates for new proton exchange membranes, Journal of Membrane Science, 197 (2002) 231-242.

[12] T. Kobayashi, M. Rikukawa, K. Sanui, N. Ogata, Proton-conducting polymers derived from poly(ether-etherketone) and poly(4-phenoxybenzoyl-1,4-phenylene),

Solid State Ionics, 106 (1998) 219-225.

[13] B. Liu, G.P. Robertson, D.-S. Kim, M.D. Guiver, W. Hu, Z. Jiang, Aromatic Poly(ether ketone)s with Pendant Sulfonic Acid Phenyl Groups Prepared by a Mild Sulfonation Method for Proton Exchange Membranes, Macromolecules, 40 (2007) 1934-1944.

[14] K.-D. Kreuer, Membrane Materials for PEM-Fuel-Cells: A Microstructural Approach, ECS Proceedings Volumes, 1995-23 (1995) 241-246.

[15] T.J. Peckham, S. Holdcroft, Structure-Morphology-Property Relationships of Non-Perfluorinated Proton-Conducting Membranes, Advanced Materials, 22 (2010) 4667-4690.

[16] T. Higashihara, K. Matsumoto, M. Ueda, Sulfonated aromatic hydrocarbon polymers as proton exchange membranes for fuel cells, Polymer, 50 (2009) 5341-5357.

[17] N. Li, J. Liu, Z. Cui, S. Zhang, W. Xing, Novel hydrophilic–hydrophobic multiblock copolyimides as proton exchange membranes: Enhancing the proton conductivity, Polymer, 50 (2009) 4505-4511.

[18] X. Guo, W. Li, J. Fang, Y. Yin, Synthesis and properties of novel multiblock copolyimides consisting of benzimidazole-groups-containing sulfonated polyimide hydrophilic blocks and non-sulfonated polyimide hydrophobic blocks as proton exchange membranes, Electrochimica Acta, 177 (2015) 151-160.

[19] H.-S. Lee, A. Roy, O. Lane, S. Dunn, J.E. McGrath, Hydrophilic–hydrophobic multiblock copolymers based on poly(arylene ether sulfone) via low-temperature coupling reactions for proton exchange membrane fuel cells, Polymer, 49 (2008) 715-723.

[20] J. Yuk, S. Lee, A.F. Nugraha, H. Lee, S.-H. Park, S.-D. Yim, B. Bae, Synthesis and characterization of multi-block poly(arylene ether sulfone) membranes with highly sulfonated blocks for use in polymer electrolyte membrane fuel cells, Journal of Membrane Science, 518 (2016) 50-59.

[21] B. Bae, K. Miyatake, M. Watanabe, Sulfonated Poly(arylene ether sulfone ketone) Multiblock Copolymers with Highly Sulfonated Block. Synthesis and Properties, Macromolecules, 43 (2010) 2684-2691.

[22] C. Liang, T. Maruyama, Y. Ohmukai, T. Sotani, H. Matsuyama, Characterization of random and multiblock copolymers of highly sulfonated poly(arylene ether sulfone) for a proton-exchange membrane, Journal of Applied Polymer Science, 114 (2009) 1793-1802.

[23] Y. Chang, G.F. Brunello, J. Fuller, M. Hawley, Y.S. Kim, M. Disabb-Miller, M.A. Hickner, S.S. Jang, C. Bae, Aromatic Ionomers with Highly Acidic Sulfonate Groups: Acidity, Hydration, and Proton Conductivity, Macromolecules, 44 (2011) 8458-8469.

[24] M. Schuster, K.-D. Kreuer, H.T. Andersen, J. Maier, Sulfonated

Poly(phenylene sulfone) Polymers as Hydrolytically and Thermooxidatively Stable Proton Conducting Ionomers, Macromolecules, 40 (2007) 598-607.

[25] S.-Y. Han, D.M. Yu, Y.-H. Mo, S.M. Ahn, J.Y. Lee, T.-H. Kim, S.J. Yoon, S. Hong, Y.T. Hong, S. So, Ion exchange capacity controlled biphenol-based sulfonated poly(arylene ether sulfone) for polymer electrolyte membrane water electrolyzers: Comparison of random and multi-block copolymers, Journal of Membrane Science, 634 (2021) 119370.

[26] M. Schalenbach, T. Hoefner, P. Paciok, M. Carmo, W. Lueke, D. Stolten, Gas Permeation through Nafion. Part 1: Measurements, The Journal of Physical Chemistry C, 119 (2015) 25145-25155.

[27] M. Schalenbach, M.A. Hoeh, J.T. Gostick, W. Lueke, D. Stolten, Gas Permeation through Nafion. Part 2: Resistor Network Model, The Journal of Physical Chemistry C, 119 (2015) 25156-25169.

[28] D.S. Kim, G.P. Robertson, M.D. Guiver, Y.M. Lee, Synthesis of highly fluorinated poly(arylene ether)s copolymers for proton exchange membrane materials, Journal of Membrane Science, 281 (2006) 111-120.

[29] A.S. Badami, O. Lane, H.-S. Lee, A. Roy, J.E. McGrath, Fundamental investigations of the effect of the linkage group on the behavior of hydrophilic–hydrophobic poly(arylene ether sulfone) multiblock copolymers for proton exchange membrane fuel cells, Journal of Membrane Science, 333 (2009) 1-11.

[30] Y. Li, X. Zhang, G. He, F. Zhang, Sulfonated poly(phenylene sulfide) grafted polysulfone proton exchange membrane with improved stability, International Journal of Hydrogen Energy, 42 (2017) 2360-2369.

[31] K. Kim, B.-K. Jung, T. Ko, T.-H. Kim, J.-C. Lee, Comb-shaped polysulfones containing sulfonated polytriazole side chains for proton exchange membranes, Journal of Membrane Science, 554 (2018) 232-243.

[32] N. Li, C. Wang, S.Y. Lee, C.H. Park, Y.M. Lee, M.D. Guiver, Enhancement of Proton Transport by Nanochannels in Comb-Shaped Copoly(arylene ether sulfone)s, Angewandte Chemie International Edition, 50 (2011) 9158-9161.

# Chapter 2

# Perfluorocyclobutyl-containing multiblock copolymers to induce enhanced hydrophilic/hydrophobic phase separation and high proton conductivity at low humidity

## 2.1. Introduction

The aggravation of climate change requires an urgent paradigm shift in the automobile industry. Many countries, including South Korea, Canada, the United Kingdom, and the European Union, are ensuring the replacement of internal combustion engine vehicles with zero-emission vehicles, such as fuel cell vehicles, in the near future through powerful measures [1]. The studies of polymer electrolyte membrane fuel cells (PEMFCs) for fuel cell vehicles are interesting because of their high power densities, good energy conversion efficiencies, and zero-emission levels [2]. A polymer electrolyte membrane (PEM), which is an essential component of PEMFCs, conducts protons from the anode to the cathode and separates both electrodes [3]. Nafion, a perfluorosulfonic acid PEM, is commercially available owing to its high mechanical strength and excellent thermal and chemical stabilities [4]. However, it is desirable to develop alternative PEMs owing to the high cost and poor mechanical stability (at high temperature (T >80 °C)) of Nafion [5].

Hydrocarbon PEMs have been highly considered as an alternative to Nafion because of their low production costs and high thermal stabilities [6]. Pioneering research on random copolymers, such as sulfonated polyimide (SPI) [7, 8], sulfonated poly(arylene ether sulfone) (SPAES) [9], and sulfonated poly(ether ether ketone) (SPEEK) [10, 11], have demonstrated their effective proton conductions under high humidity conditions. However, owing to their insufficient hydrophilic aggregations compared with those of Nafion, random copolymers display inadequate proton conductivity under low humidification [12]. PEMs must maintain sufficient proton conductivity in all humidification ranges, even under low humidity conditions; this is crucial for fuel cell vehicles in which humidifiers are generally removed to reduce the volume of the system [13, 14].

To induce sufficient proton conductivity in well-connected proton-conducting channels under low humidification, well-developed phase separation of the hydrophilic and hydrophobic moieties of hydrocarbon PEMs must be achieved [15]. The development of multiblock copolymers in which the hydrophilic and hydrophobic blocks are placed next to each other, thus densely arranging the sulfonic acid groups together, is an effective approach toward enhancing phase separation [16]. Therefore, multiblock copolymers containing different hydrophobic and hydrophilic blocks, which incorporated different structural groups, including SPI [17, 18], SPAES [19, 20], and SPEEK [21, 22], have been synthesized to improve proton conductivity under low humidity conditions.

Further, the phase separation level was enhanced by augmenting the acidities and densities of the hydrophilic components [23]. Kreuer et al. fabricated highly sulfonated poly(phenylene sulfone) polymers with high acidic density. They achieved high proton conductivity at a high temperature and low humidity [24].

Nevertheless, the demand for increased proton conductivities under low humidity conditions has motivated us to synthesize an enhanced phase-separated polymer [25].

There are many studies on the structural designs of multiblock copolymers to improve their hydrophilicity. However, there are only a few research on improving their hydrophobicity [26]. Fluorocarbons are typically known hydrophobic compounds owing to the high electronegativity of fluorine, which limits their interactions with polar molecules, such as water [27]. The presence of hydrophobic fluorocarbons in PEMs imparts them with thermal, mechanical, and chemical stabilities compared with that of hydrocarbons [28]. Further, the utilization of fluorocarbons as the hydrophobic moieties can also enhance the hydrophilic/hydrophobic phase separations of the membrane [29]. However, regarding the enhancement of the hydrophobicity of PEMs, only a few structural designs, such as those employing the perfluoroalkylene [30], decafluorobiphenyl [31, 32], polyvinylidene fluoride [33, 34], $–CF_3$ [2, 35, 36], or $–CF_2–CF_2–$ groups [37, 38], have been reported. Other fluorinated groups have been rarely reported because of their synthetic complications [39]. Among the few structures of fluorinated groups for PEMs, perfluorocyclobutyl (PFCB) has been reported for its thermal stability and excellent solubility [40-43]. Additionally, the cyclopolymerization of trifluorovinyl ether monomers can afford flexible, yet thermally robust, fluorocarbon linkages without requiring special catalysts or initiators [44, 45]. Although there are numerous research on the utilization of PFCB as the hydrophobic segments of random copolymers [46-51], its utilization as a repeating unit in the hydrophobic block of a multiblock copolymer has been rarely reported [52].

In this study, we reported a novel sulfonated–fluorinated multiblock copolymer containing PFCB and highly sulfonated poly(phenylene sulfide sulfone) (sPPSS) moieties as the hydrophobic and hydrophilic oligomers, respectively. The flexible PFCB group facilitated high hydrophobic aggregation, which induced intense phase separation and increased the proton conductivity, even under low humidification. The multiblock copolymer coupled with the super-hydrophilic oligomer generated a well-developed nanophase separation. The cast membrane was subjected to additional thermal annealing treatment to maximize the hydrophilic/hydrophobic phase separations. The partially fluorinated hydrophobic oligomer achieved interfacial compatibility with the Nafion binder in the electrode layer, which imparted the fabricated membrane electrode assembly (MEA) with reasonable fuel cell performance and durability.

## 2.2. Experimental

### Materials

N,N-dimethylacetamide (DMAc), 1-methyl-2-pyrrolidone (NMP), dimethyl sulfoxide (DMSO), acetonitrile, dichloromethane, diphenyl ether, potassium carbonate, cesium carbonate, boron tribromide solution, 4,4′-biphenol (BP), 1,2-dibromotetrafluoroethane (DBTFE), 4-methoxy phenol, and lithium sulfide were purchased from Sigma Aldrich and utilized as received. Sodium chloride (NaCl), magnesium sulfonate, isopropyl alcohol (IPA), hexane, and chloroform were purchased from Samchun Chemicals and utilized as received. Further, decafluorobiphenyl (DFBP) was purchased from Fluorochem, hydrochloric acid (HCl) was purchased from OCI, sulfuric acid (fuming, 65%) was purchased from Merck, and 4,4-difluorodiphenylsulfone (DFDPS) was purchased from Rechem. Furthermore, zinc was purified by HCl, mixed with diethyl ether, and dried at reduced pressure. Additionally, 3,3-disulfonated-4,4′-difluorodiphenylsulfone (SDFDPS) was synthesized from DFDPS, after which it was recrystallized with ethanol/H2O (7:5) and vacuum-dried at 80 °C before it was utilized [53].

## Synthesis of the hydrophilic oligomer: sPPSS

The hydrophilic oligomer, sPPSS, was prepared by the nucleophilic substitution reaction of SDFDPS and lithium sulfide, as shown in Figure 2.1. The molecular weight was controlled by varying the ratio of SDFDPS to lithium sulfide. To prepare sPPSS with a molecular weight of 8700 $\mathrm{gmol}^{-1}$, SDFDPS (19.7 mmol), lithium sulfide (20.8 mmol), and DMAc were mixed in a 100-mL round bottom flask (RBF) and charged with argon. The temperature was increased to 160 °C, and the solution reacted for 12 h. The solution was cooled to 25 °C, after which DFBP (11.2 mmol) and DMAc were added. Next, the temperature was increased from 25 °C to 80 °C for 3 h, and the DFBP-containing solution reacted for 3 h. The product was precipitated by IPA and dried in vacuo at 80 °C.

## Synthesis of hydrophobic monomer: 4,4′-bis(trifluorovinyloxy)biphenyl (TFB)

To obtain monomer (TFB), 4,4′-bis(2-bromotetrafluoroethoxy)biphenyl (BTB) was synthesized, as shown in Figure 2.2, by adding BP (26.9 mmol), cesium carbonate (64.6 mmol), and DMSO in a 250-mL RBF, and the reactor was heated to 50 °C for 1 h under argon atmosphere. Next, DBTFE (134.7 mmol) was added and reacted at 50 °C for 6 h. The solution was extracted with hexane and brine, and the extracted hexane layer was evaporated retrieving white solid. The white solid was purified by column chromatography using hexane as the eluent. The purified product (BTB) was dried at 80 °C in a vacuum oven. BTB (32.2 mmol), zinc (70.8 mmol), and acetonitrile were added in a-250 mL RBF with argon inlet. The temperature was raised to 85 °C with reflux and maintained for 18 h. In order to dissolve zinc, 0.5 M HCl was injected to the solution. The solution was extracted, evaporated, and purified as the same manner as the BTB process. The final product (TFB) was completely dried in a vacuum oven at 80 °C.

## Synthesis of hydrophobic end-capper: 4-(trifluorovinyloxy)methoxybenzene (TFM)

Hydrophobic end-capper, 4-(2-bromotetrafluorothoxy)methoxybenzene (BTM), was synthesized, as shown as Figure 2.3, by adding 4-methoxyphenol (53.5 mmol), cesium carbonate (64.2 mmol), and DMSO in a 250-mL RBF with argon inlet. The solution was heated to 50 ° C and stirred for 1 h. Then, DBTFE (128.4 mmol) was added to the solution and the mixture was heated to 50 °C for 1 h. The solution was extracted with hexane and brine and was evaporated. The product was then purified by column chromatography using hexane as the eluent. The purified product (BTM) was dried sufficiently in vacuo. BTM (46.2 mmol), zinc (73.9 mmol), and acetonitrile were added to a 250-mL RBF, and the temperature was raised to 85 °C with reflux and maintained for 24 h. After adding 0.5 M HCl to dissolve zinc, the solution was extracted, evaporated, and purified as the same manner as the BTM process. The purified product (TFM) was dried in a vacuum oven.

## Synthesis of the hydrophobic oligomer: BP_PFCB

A hydrophobic monomer, 4,4-bis(trifluorovinyloxy)biphenyl (TFB) (22.1 mmol), a hydrophobic end-capper, 4-(trifluorovinyloxy)methoxybenzene (TFM) (4.1 mmol), and diphenyl ether were added to the 100-mL RBF with the complete removals of oxygen and water through lyophilization. The charged solution in sealed RBF was lyophilized by liquid nitrogen in a vacuum, followed by repeated thawing processes in an argon atmosphere. After the lyophilization process, the solution was heated to 250 °C under reflux and maintained for 72 h. After the reaction, the solution was precipitated in methanol and vacuum-dried thoroughly at 80 °C. Next, the dried product was dissolved in chloroform and precipitated in methanol. Thereafter, the purified OCH3_BP_PFCB was sufficiently dried in vacuo at 80 °C.

The demethylation process proceeded with the addition of OCH3_BP_PFCB (0.9

mmol) and dichloromethane to 100-mL RBF in an argon atmosphere. RBF was immersed in an ice bath to lower the temperature. As the reaction proceeded in the ice bath, a boron tribromide solution (9.4 mmol) was added dropwise. After the injection of the boron tribromide solution, the ice bath was removed, after which the solution reacted for 24 h at 25 °C. Thereafter, the obtained solution was precipitated in methanol, washed with deionized water, and vacuum-dried. The dried product was dissolved in chloroform, after which it was precipitated with methanol. Subsequently, the purified product, BP_PFCB, was vacuum-dried.

## Synthesis of the multiblock copolymer: SF-X/Y

BP_PFCB (0.68 mmol), potassium carbonate (3.4 mmol), and NMP were added to 100-mL RBF, as illustrated in Figure 2.1. The temperature of the solution was raised to 140 °C for >1 h, after which it reacted for 30 min. Afterward, the temperature was reduced to 25 °C, and sPPSS, (0.7 mmol) was added. Subsequently, the temperature was slowly raised to 80 °C and maintained for 48 h. The obtained solution was precipitated in IPA and washed with deionized water and IPA. The final multiblock copolymer, SF-X/Y, was sufficiently vacuum-dried at 80 °C.

## Preparation of the membrane

Regarding the pristine membranes, SF-X/Y was dissolved in DMAc (21.5 wt%) and filtered with a 5-μm syringe filter. The filtered solution was cast on a glass plate utilizing a doctor-blade coating. The cast membrane was vacuum-dried for 24 h at 60 °C. For the acid treatment, the dried membrane was immersed in 1.5 M $H_2SO_4$ for 24 h and washed several times with deionized water.

To obtain thermally annealed membranes, SF-X/Y was dissolved in DMAc (21.5 wt%) and filtered. The filtered solution was cast on a glass plate by doctor-blade coating and vacuum-dried for 24 h at 60 °C. Thereafter, the glass plate was immersed in deionized water to remove the membrane from the plate. Further, the free membrane was vacuum-dried at 80 °C to remove the water. The dried membrane was thermally annealed in an oven for 5 h at 150 °C, after which the temperature was slowly reduced. For the acid treatment, the membrane was immersed in 1.5 M $H_2SO_4$ for 24 h after cooling and washed several times with deionized water. All the membranes were 12–15 μm thick in their dry states.

## Gravimetric ion-exchange capacity (IECw)

Acid-treated SF-X/Y (0.035 g) was added to 100 mL of a 0.01 M NaCl aqueous solution and stirred for 24 h to substitute $H^+$ with $Na^+$. $IEC_w$ of the NaCl aqueous solution from which the $H^+$ ions were extracted was measured by the acid titration method employing an autotitrator (Metrohm 794 Basic Titrino). Titrating with a 0.01 M sodium hydroxide (NaOH) aqueous solution, $IEC_w$ was calculated by the following equation:

$$\mathrm{IEC_w(meq/g)} = \frac{\mathrm{V \times C}}{\mathrm{w}},$$

where V is the volume of the aqueous solution of 0.01 M NaOH (mL), which was utilized to titrate to pH of 7; w is the weight of the dried sample (g); and C is the molar concentration of the NaOH aqueous solution, which was utilized for the titration.

## Polymer characterization

To measure the inherent viscosity (IV), SF-X/Y was dissolved in NMP (0.5 $gdL^{-1}$) and filtered with a 5-μm syringe filter. IV was measured in a water bath at 25 °C utilizing a Cannon-Ubbelohde viscometer. The synthesized products were dissolved in deuterated DMSO (DMSO-$d_6$) or $CDCl_3$ before they were utilized for proton and fluorine-19 nuclear magnetic resonance ($^1H$ and $^{19}F$ NMR) characterizations. The $^1H$ and $^{19}F$ NMR spectra were obtained on a Bruker Avance NEO (500 MHz) spectrometer. Fourier transform infrared (FTIR) spectra were obtained from Nicolet 5700 (Thermo) FTIR Spectrometer. The mechanical properties of the membranes were measured using a universal testing machine (UTM, Lloyd Instrument LR5K) at room temperature with a crosshead speed of 5 mmmin$^{-1}$. Samples were prepared as ASTM D638 type V.

## Thermal property

Differential scanning calorimetry (DSC) was performed on a Thermo Plus II DSC 8230 to analyze the glass transition temperature ($T_g$) of SF-X/Y. The temperature was controlled from 0 to 250 °C at the rate of 10 °Cmin$^{-1}$, and $T_g$ was analyzed with the value of the 2nd round of heating. To investigate the degradation temperature ($T_d$) of the multiblock copolymer, thermogravimetric analysis (TGA) (Pyris 1 TGA from Perkin Elmers) was carried out from 25 to 800 °C with a heating rate of 10 °Cmin$^{-1}$ under nitrogen flow of 20 mLmin$^{-1}$.

## Transmission electron microscopy (TEM)

The acid-treated membrane was immersed in an aqueous solution of 0.5 M lead acetate for 24 h to replace the $H^+$ form with the $Pb^{2+}$ form. Lead, which was on the surface of the membrane, was washed with deionized water for 24 h, and the membrane was sufficiently vacuum-dried at 80 °C. The dried membrane was prepared by a Leica EM UC6 ultramicrotome, and the TEM images were obtained on a TECNAI G2 T-20S microscope. Scanning transmission electron microscopy (STEM)/energy-dispersive X-ray spectroscopy (EDS) elemental mapping images were obtained from Tecnai G2 F30 instrument.

## Small-angle X-ray-scattering analysis (SAXS)

To investigate the morphology of the membranes (the $H^+$ form), SAXS measurements were conducted at the Pohang Accelerator Laboratory (PAL), Pohang, Republic of Korea, utilizing the PLS-II 3C beamline. The scattering vector was calculated by the following equation:

$$q = \frac{4\pi}{l(\sin 2\theta)},$$

where l is the wavelength of the Cu Kα radiation ($\lambda$ = 1.541 Å) and 2θ is the scattering angle. Further, the inter-domain space (d) was calculated by the following equation:

$$d = \frac{2\pi}{q_{max}},$$

where $q_{max}$ is the maximum q-value ($10^{-10}$ $m^{-1}$).

## Oxidation stability

The oxidation stability of the membranes were investigated by ex situ Fenton test. Using the Fenton's reagent we have created ($H_2O_2$ 3 wt%, 2 ppm $FeSO_4$), the membranes were tested at 60 °C for 6 h. Gel permeation chromatography (GPC) was utilized to measure the number average molecular weight ($M_n$) before and after the Fenton test. The reduction percentage was calculated by the following equation:

$$\text{Reduction } \% = \frac{\mathrm{M}_{\mathrm{n,initial}} - \mathrm{M}_{\mathrm{n,final}}}{\mathrm{M}_{\mathrm{n,initial}}} \times 100\%.$$

Gel permeation chromatography (YL9120 UV/Vis Detector) with YL9112 Isocratic pump and Shodex KF-805L column was used to determine number average molecular weight ($M_n$). The flow rate of the eluent (HPLC grade DMAc with 0.05 M LiBr) was 1.0 $\mathrm{mLmin^{-1}}$. Calibration was conducted using polystyrene standards.

## Water sorption analysis

The acid-treated membrane was prepared and cut into a size of 2 cm × 2 cm. After immersing the cropped membrane in deionized water for 24 h at 25 °C, its weight, length, and thickness were measured. The dimensions (the weight, length, and thickness) of the dried membrane were measured by dehydrating it in a vacuum for

24 h at 50 °C. The membrane was re-immersed in deionized water for 24 h and measured again. By substituting the average measured values into the following equations, the water uptake and dimensional swelling percentage were obtained.

$$\Delta l = \frac{l_{wet} - l_{dry}}{l_{dry}} \times 100(\%)$$

$$\Delta t = \frac{t_{wet} - t_{dry}}{l_{dry}} \times 100(\%)$$

$$\Delta V = \frac{V_{wet} - V_{dry}}{V_{dry}} \times 100(\%)$$

$$\text{Water Uptake (wt\%)} = \frac{w_{wet} - w_{dry}}{w_{dry}} \times 100(\%),$$

where $l_{wet}$, $t_{wet}$, and $V_{wet}$ are the length, thickness, and volume of the wet film, respectively; $l_{dry}$, $t_{dry}$, and $V_{dry}$ represent the length, thickness, and volume of the dry film, respectively; $w_{wet}$ and $w_{dry}$ represent the weights of the wet and dry films, respectively.

The hydration number (λ) was calculated as the average number of water molecules per sulfonic acid group in the hydrated state, as follows [54]:

$$\lambda = \frac{[H_2O]}{[SO_3 -]} = \frac{\text{water uptake (\%)} \times 10}{18 \times \text{IEC(mmol/g)}}$$

$$[-SO_3H] = \frac{W_{dry}(g)}{Vol_{wet}(cm^3)} \times IEC_w \ (meqg^{-1}).$$

The volumetric IEC ($IEC_v$) represents the concentration of the sulfonic acid group per unit volume in the dry state.

$$\mathrm{IEC_v(meq\ \ cm^{-3}) = IEC_w(meq\ \ g^{-1}) \times density}$$

## Proton conductivity

To measure the proton conductivity in the wet state, AC impedance spectroscopy (ACIS) was performed by the 4-probe method at 25 °C and relative humidity (RH) of 100% utilizing a Solatron-1280 impedance/gain-phase analyzer (Solatron), and the frequency was measured with conversion in the range of 0.1–10,000 Hz. The value of the calculated impedance was converted to the proton-conductivity value through the following equation:

$$\mathrm{Proton\ \ Conductivity\ \ (S\ \ cm^{-1})} = \sigma = \frac{1}{\mathrm{R}} \times \frac{\mathrm{L}}{\mathrm{A}},$$

where R is the measured impedance value (Ω), L is the distance between the measured electrodes, and A is the cross-sectional area ($cm^2$) of the ion-exchange membrane that was utilized for the measurement.

The “effective” proton mobility ($\mu_{eff}$) is the normalized proton conductivity value after the removal of the effect of the acid concentration. It can be calculated by the following equation:

$$\mu_{\mathrm{eff}} = \frac{\sigma}{F \times [-SO_3H]},$$

where F is Faraday’s constant and σ ($Scm^{-1}$) is the proton conductivity at 25 °C and 100% RH.

The proton conductivities under different humidity conditions were measured by the 4-probe method utilizing a BT 301 (a PGZ 301 dynamic EIS voltammeter, Bekktech) system at 80 °C.

## Interfacial bonding strength

The SF-X/Y membrane and Nafion were hot-pressed face to face at 130 °C and 100 $kgfcm^{-2}$. The T-peel adhesion test in which the ends of the two different membranes were pulled apart, was performed to measure the interfacial bonding strength with a universal testing machine (Lloyd Instruments, LR5K) at 25 °C and a crosshead speed of 10 $mmmin^{-1}$.

## Fuel cell performance

MEA was fabricated with the acid-treated membrane utilizing commercial gas-diffusion layers (JNT30-A3 JNTG), which were coated with Pt/C and the Nafion binder (40 wt% Pt/C, Tenaka). The Pt loadings of the anode and cathode were 0.3 ± 0.05 mgcm$^{-2}$ each, and the geometric active area of MEA was 25 cm$^2$. The fabricated MEA was sandwiched in two carved graphite channels with a serpentine-type flow path. The performance of the single-cell was assessed at the PEMFC test station (Scitech Korea, Republic of Korea). Fully humidified hydrogen and air were injected into the anode and cathode, respectively, in a 1.5:2 stoichiometry. Before the evaluation, the single-cell was activated under a hydrogen–air test condition for 12 h at a voltage of 0.6 V. The cell polarization curve was obtained via the voltage sweep method with a step change of 0.05 V per 25 s at 65 °C by varying RH by 100% and 50% without backpressure. The electrochemical impedance spectroscopy (EIS) was carried out in a galvanostatic mode (Biologic, SP-300). An AC sinus signal (20% amplitude) was applied to a fixed current of 25 A (frequency range from 10 mHz to 10 MHz).

## Chemical and physical durabilities

To conduct the open-circuit voltage (OCV) hold test, hydrogen and air in a 10:10 ratio (set to achieve 0.2 mAcm$^{-2}$) were continuously fed to the cell at 90 °C and 30% employing a fuel-cell test station (Z010-100, SCITECH KOREA). The humidity (wet/dry) cycling tests were conducted by alternatively feeding RH 130% and 0% air (2000 sccm) into MEA for 2 min at 80 °C.

## 2.3. Results and discussion

### Synthesis of SF-X/Y

SF-X/Y was prepared by the polycondensations of the hydrophilic sPPSS and hydrophobic BP_PFCB oligomers (X and Y are the molecular weights (kDA) of the sulfonated and fluorinated oligomers, respectively). The hydrophilic oligomer, sPPSS, was designed to comprise one sulfonic acid group per benzene group in a repeating unit, thus generating a very high acidic density. sPPSS was synthesized by the nucleophilic polycondensation reaction of SDFDPS and lithium sulfide, followed by an end-capping reaction with DFBP. The molecular weight was controlled by adjusting the molar feed ratios of SDFDPS and lithium sulfide. The end-capping reaction was verified by the detection of fluorine in $^{19}$F-NMR (Figure 2.4b) at −131, −137, −138, −149, and −161 ppm. The molecular weight was determined by end-group analysis (Figure 2.5). The hydrophilic oligomers were obtained with targeted molecular weights of 5.4, 8.7, and 12.7 kDa.

The hydrophilic oligomer, sPPSS, was synthesized by the nucleophilic polycondensation reaction, as shown in Figure 2.1. According to the $^{1}$H NMR result (Figure 2.4), the protons, which were adjacent to the electron-withdrawing sulfone group and the sulfonic acid group, were detected at 8.31, 7.79, and 7.27 ppm. The original hydrophilic oligomer, sPPSS, has its limits on obtaining molecular weight through end group analysis due to the overlapping of the $^1$H NMR peaks between the end group and the polymer repeat unit. Therefore, a supplementary end-capper, 4-tert-butylphenol, was reacted to a small portion of existing decafluorobiphenyl(DFBP)-ended sPPSS to obtain precise oligomer length. The reaction was maintained at 80 °C for 3 h. $^{19}$F NMR (Figure 2.5b) verified the disappearance of fluorine, para position to the original DFBP-ended sPPSS, at 149.45 ppm, assuring complete end-capping reaction of the oligomer. In $^1$H NMR (Figure 2.5a), methoxy protons (d′) of the end-capper and protons (a′, b′, and c′) of the repeat unit were integrated and calculated for the molecular weight of the hydrophilic oligomer. The end group analysis from the $^1$H NMR resulted in molecular weights of 5.4 kDa, 8.7 kDa, and 12.7 kDa for hydrophilic oligomer.

The synthetic pathway for obtaining the partially fluorinated hydrophobic oligomer (BP_PFCB). TFB containing a trifluorovinyl ether group was polymerized via thermal [2π + 2π] cycloaddition to produce TFM-terminated oligomers. The detailed information on the hydrophobic monomer (TFM) and the hydrophobic end-capper (TFB) are shown in Figures 2.6 and 2.7, respectively. This is the first report on the synthesis of hydrophobic oligomers with targeted molecular weights by controlling the molar feed ratios of TFB and TFM. The end-capping reaction was confirmed by the disappearances of trifluorovinyl fluorines of TFB and TFM at −120 ppm and the appearances of the PFCB fluorines at −130 ppm in the $^{19}$F NMR (Figure 2.8b) spectra. Further, the molecular weight of the hydrophobic oligomer was obtained by end-group analysis by comparing the integration of the methoxy protons (peak s′) of the end group and the aromatic protons (peaks o′ and p′) of the repeating unit in the $^{1}$H NMR result (Figure 2.8a). The hydrophobic oligomers with targeted molecular weights of 5, 8, and 11.7 kDa were obtained. After the initial polymerization of the hydrophobic oligomer, demethylation was performed with a boron tribromide solution to impart it with functional reactivity. The demethylation process was confirmed by the disappearance of the methoxy peak from the $^{1}$H NMR spectrum at 3.69 ppm (Figure 2.4c). Additionally, the remaining proton peaks in the $^{1}$H NMR spectrum (Figure 2.4c) and the PFCB peak in the $^{19}$F-NMR spectrum (Figure 2.4d) were unchanged, thereby confirming that no side reaction had occurred.

BTB was synthesized by nucleophilic substitution reaction of BP and BPTFE, and the synthesis was successfully confirmed in $^{1}$H NMR (Figure 2.6a) and $^{19}$F NMR (Figure 2.6b). TFB was further synthesized through elimination reaction of BTB by zinc, and was confirmed by peaks shifting upfield in the $^{1}$H NMR owing to the shielding effect of the double bond. In addition, the $^{19}$F NMR exhibited disappearance of fluorines (5′ and 6′) in BTB and appearance of new fluorines (7′, 8′, and 9′) in TFB, confirming successful synthesis of the hydrophobic monomer.

Hydrophobic end-capper (TFB) was synthesized and utilized in polymerization of BP_PFCB to provide functional terminal for hydrophobic oligomer. TFB was synthesized through nucleophilic substitution reaction of 4-methoxyphenol and DBTFE and elimination reaction by zinc. In $^{19}$F NMR (Figure 2.7b), fluorines of BTM at 67.89 ppm (10′) and 86.16 ppm (11′) disappeared and fluorines of TFM at −120.57 ppm (12′), −127.57 ppm (13′), and −133.31 ppm (14′) appeared, indicating the formation of double bonds.

The hydrophobic oligomer, BP_PFCB, was polymerized via thermal [2π + 2π] cycloaddition using the hydrophobic monomer (TFM) and the hydrophobic end-capper (TFB). In the $^{1}$H NMR result (Figure 2.8a), the aromatic protons, which confirmed the successful reaction of the hydrophobic oligomer without a by-product or side reaction, were obtained at 7.11 and 7.39 ppm.

Methoxy ended hydrophobic oligomer, BP_PFCB_OCH$_3$, was used in the end group analysis calculation to obtain oligomer length. From $^{1}$H NMR (Figure 2.8a), protons (s′) at the methoxy end group and protons (o′ and p′) at the repeating unit were integrated and calculated for molecular weight of the oligomer. The calculation from the $^{1}$H NMR resulted in molecular weights of 5 kDa, 8 kDa, and 11.7 kDa for hydrophobic oligomer.

SF-X/Y containing the PFCB groups were synthesized via the condensation polymerization of the DFBP group of the hydrophilic oligomer and the hydroxy group of the hydrophobic oligomer. The highly reactive DFBP groups ensured that the reaction proceeded at 80 °C by minimizing the crosslinking of the DFBP groups and preventing the ether–ether exchange reaction [55]. The structure of SF-X/Y was verified by $^1$H NMR (Figure 2.4e) and Fourier-transform infrared (FTIR) spectroscopy (Figure 2.9). The FTIR spectrum of the hydrophobic oligomer (BP_PFCB) displayed characteristic peaks for PFCB ring at 957 $cm^{-1}$ and phenyl ring at 1495 $cm^{-1}$. The sulfonic acid group was confirmed with the presence of the $SO_2$ symmetric stretch at 1067 $cm^{-1}$ and OH stretch at 3500 $cm^{-1}$. Further, the disappearance of fluorine at −149.46 ppm (the para position) to the DFBP group in $^{19}$F-NMR (Figure 2.4f) indicated the completion of the reaction. SF-X/Y with different $IEC_w$ values were polymerized by changing the molecular weights of the hydrophilic and hydrophobic oligomers. All SF-X/Y exhibited inherent viscosities of >1 $dLg^{-1}$, which indicated that high molecular weights were obtained. The general properties of SF-5.4/5, SF-8.7/8, and SF-12.7/11.7 with $IEC_w$ of 1.67, 1.89, and 2.01 $meqg^1$, respectively, are summarized in Table 2.1. BPSH 50 was compared as a reference hydrocarbon membrane [56]. SF-X/Y were soluble in common polar aprotic solvents and were cast into membranes by DMAc.

The stress–strain curves of SF-X/Y (Figure 2.10 and Table 2.2) revealed a sufficiently high tensile strength of 48.85 MPa, and a reasonable value of the percentage strain at break (11.56%–23.27%) was achieved by a careful balance between the rigid sulfone groups of the hydrophilic oligomer and the flexible ether-rich PFCB moieties of the hydrophobic oligomer.

## Thermal annealing and the morphological property

Thermal annealing above the $T_g$ can reorganize polymer chains to reach the thermodynamically preferred, nanostructured arrangement [57]. Previous studies indicated that thermal annealing could modify the morphological architecture of the membrane by mechanically reducing the unfavorable swelling behavior without compromising IEC and proton conductivity [58]. Owing to the high $T_g$ of conventional aromatic hydrocarbon PEMs, such as SPI, SPAES, and SPEEK, they are thermally annealed at very high temperatures (>200 °C) or with the aid of a solvent [59]. Nevertheless, those previous methods are still associated with complications, such as restricted polymer chain motion, undesirable side reactions, modified thermal history, and limited reproducibility. It was reported that PFCB containing polymers possess relatively low $T_g$ (106–144 °C) [60] because of the flexible ether and PFCB groups, and this relatively low $T_g$ facilitates successful thermal annealing at a low temperature without any assistance. DSC was conducted to determine $T_g$ of SF-X/Y, as shown in Figure 2.11. $T_g$ of SF-5.4/5, SF-8.7/8, and SF-12.7/11.7 lie around 150 °C, which is lower than the $T_g$ values of typical hydrocarbon membranes (>200 °C) [35]. The TGA curves (Figure 2.12) confirmed that the degradation of the polymer commenced at 450 °C, and this confirmed the high thermal stability of SF-X/Y. There was a wide margin between the low $T_g$ (150 °C) and high $T_d$ (450 °C) values, which afforded abundant freedom for morphological modification. The SF-X/Y samples were thermally annealed for 5 h at 150 °C; thus, they were named SF-X/Y_ann. Through thermal annealing, the flexible ether and PFCB groups with relatively high mobility induced thermodynamically favorable polymer chain packing of the hydrophobic moieties, strengthening the contrast between the hydrophilic moieties. The thermally induced polymer chain packing led to an increased $IEC_v$ of SF-X/Y_ann, which represented the concentration of sulfonic acid groups per unit volume, than that of SF-X/Y at the same $IEC_w$ (Figure 2.13 and Table 2.1). Put differently, given the same gravimetric number of the ion-exchanging group, SF-X/Y_ann could adjust into a more densified configuration of the sulfonic acid groups.

The TEM images of SF-X/Y and SF-X/Y_ann are shown in Figures 2.14 and 2.15 at 50 and 100 nm scales to investigate the phase separation between the hydrophilic and hydrophobic domains, respectively. Due to the electron density difference, the dark portion indicates the hydrophilic domain composed of lead-stained sulfonic acid groups, while the light portion indicates the hydrophobic one. A sharp contrast was observed in the phase separation between the hydrophilic and hydrophobic domains of all the membranes. As the hydrophilic block length increased, the size and connectivity of the hydrophilic agglomerates also increased. In addition, the thermally annealed SF-X/Y_ann (Figures 2.14b and d) revealed very evident phase separation with increased connectivity and contrast of the hydrophilic moieties compared to pristine SF-X/Y (Figures 2.14a and c).

STEM/EDS analysis was conducted to observe the elemental images of Pb and F. In the high-angle annular dark-field (HAADF) STEM image, the light portion indicates the hydrophilic domain and the dark portion indicates the hydrophobic one. SF-12.7/11.7_ann (Figure 2.16d) showed a diagonally separated Pb signals, a "proton conducting pathway" of lead-stained sulfonated groups. Compared to the SF-12.7/11.7 (Figure 2.16c), the thermally annealed SF-12.7/11.7_ann showed a clearer, more distinct phase separation. Although it was difficult to interpret the dispersion of Pb signals for the pristine SF-5.4/5 (Figure 2.16a), owing to the smaller channels, the Pb signals were relatively concentrated for the annealed SF-5.4/5_ann (Figure 2.16b).

SAXS analysis was performed to quantitatively investigate the morphological properties of SF-X/Y and SF-X/Y_ann. As shown in Figure 2.17, SF-12.7/11.7 exhibited the d-spacing (30.31 nm) was greater than that of SF-5.4/5 (21.61 nm). The thermally annealed SF-X/Y_ann exhibited a slight difference in the d-spacing compared with that of pristine SF-X/Y.  However, owing to the polymer chain packing of the hydrophobic moieties, the increase of intensity was observed for SF-X/Y_ann. This finding corresponds to that of the TEM images, which revealed that the increase in contrast for the thermally annealed membrane was more pronounced than the increase in ionic domain size.

## Oxidation stability

The oxidation stabilities of the membranes were analyzed by the Fenton test, and the changes in the number average molecular weight ($M_n$) were determined by GPC, as shown in Table 2.3. The degradation mechanism of the Fenton test is described as the attack of the polymer chain by in situ-formed hydroxyl and hydroperoxyl radicals, which cause the breakdown of its backbone into small pieces [61]. The reduction percentages of SF-X/Y and SF-X/Y_ann ranged from −48.0% to −66.7%, while that of BPSH 50 was −75.3%, indicating a greater reduction. Additionally, BPSH 50 was completely disintegrated after the Fenton test, while SF-X/Y and SF-X/Y_ann were relatively intact, as shown in Figure 2.18.

## Water uptake and dimensional property

The water uptake of PEM affects its proton conductivity and mechanical stability. An appropriate level of water uptake is crucial to achieving high ion conductivity, while an excessive level will cause excessive swelling and reduce its proton conductivity owing to the dilution effect of acid [62]. The water uptake and dimensional properties of the membranes were analyzed (Figure 2.19). As observed, the water uptakes of SF-X/Y and SF-X/Y_ann were higher than that of Nafion 212 (20.5 %), although they were lower than that of BPSH 50 (115%). The water uptake of SF-X/Y increased with $IEC_w$ since the additional sulfonic acid groups increased its water retention capacity. The water uptake of SF-8.7/8 (68.8%) was 1.7 times higher than that of SF-5.4/5 (40.4%), and the water uptake of SF-12.7/11.7 (91.7%) was 1.3 times higher than that of SF-8.7/8. Further, thermally annealed SF-X/Y_ann exhibited a lower water uptake compared with that of pristine SF-X/Y, which correspond to increased $IEC_v$ and reduced $\lambda$ (Table 1). The thermal annealing of the membranes caused the densification of acid, which increased the concentration of the ions while moderating the number of water molecules per sulfonic acid group. SF-5.4/5_ann, SF-8.7/8_ann, and SF-12.7/11.7_ann exhibited water uptake capacities of 34.4%, 59%, and 83.7%, respectively.

The dimensional swellings of SF-X/Y and SF-X/Y_ann were higher than that of Nafion 212 (30.7%) and lower than that of BPSH 50 (95%). Dimensional swelling increases with increasing block length within SF-X/Y, as demonstrated by their water uptake capacities. SF-12.7/11.7_ann with an $IEC_w$ value of 2.01 $meqg^{-1}$ exhibited the highest dimensional swelling (94.2%), which was slightly lower than that of hydrocarbon-based BPSH 50 (95%) with a smaller $IEC_w$ value (1.96 $meqg^{-1}$). SF-8.7/8 and SF-5.4/5 exhibited lower-dimensional swellings of 68% and 59.1%, respectively. All the pristine membranes exhibited anisotropic swelling, where Δt was more dominant than Δl, as commonly reported for multiblock PEMs [63]. The Δt values of SF-X/Y were 4.0–7.2 times higher than their Δl ones. Interestingly, thermally annealed SF-X/Y_ann exhibited different behaviors at different block lengths. SF-5.4/5_ann possessed a much smaller Δt (17.1%) and a slightly larger Δl (8.1%) compared with those (42.1% and 5.8%) of SF-5.4/5, respectively, thus exhibiting an increased isotropic behavior and lowered dimensional swelling since the aggregation of hydrophilic $SO_3H$ via thermal annealing allowed the hydrophobic moieties in the matrix to further suppress the dimensional swelling behavior. SF-8.7/8_ann demonstrated a similar trend as SF-5.4/5_ann, but the reduction in Δt decreased with a decreasing reduction in ΔV. Conversely, SF-12.7/11.7_ann exhibited a similar Δt value (48.7%) to that of SF-12.7/11.7 (49.3%) and underwent similar dimensional changes. A membrane with a low block length exhibited a more distinct improvement after thermal annealing than did a membrane with a high block length.

## Proton conductivity under full humidification

The proton conductivity was measured under full humidification to analyze proton conduction as a function of $IEC_w$ under a hydrated condition (Figure 2.20a). The proton conductivities of SF-X/Y increased with $IEC_w$ from 0.112 to 0.127 $Scm^{-1}$ because the increase in the number of ion-exchange groups promoted enhanced connectivity between the $SO_3H$ agglomerates. Comparing the prepared multiblock copolymers to a random copolymer (BPSH 50) at the same $IEC_w$ (1.96 $meqg^{-1}$), the estimated proton conductivities of SF-X/Y and SF-X/Y_ann were 0.123 and 0.13 $Scm^{-1}$, which were higher than that of BPSH 50 (0.109 $Scm^{-1}$), respectively. Remarkably, SF-5.4/5 with lower $IEC_w$ (1.67 $meqg^{-1}$) exhibited higher proton conductivity of 0.112 $Scm^{-1}$ compared with BPSH 50 with higher $IEC_w$ (1.96 $meqg^{-1}$). According to the previous discussion on the water sorption behavior, SF-X/Y achieved relatively limited water uptake and $\lambda$ compared with BPSH 50. Thus, it was concluded that the high proton conductivity of SF-X/Y was not induced by the absorption of water. Put differently, the improved proton conductivity was caused by the generation of effective proton-conducting channels from the multiblock architecture. By densely locating the $SO_3H$ groups together, multiblock copolymers can create more defined and connected hydrophilic domains compared to the isolated domains of random copolymers, thus improving the proton transport [21].

Although pristine SF-X/Y exhibited reasonable proton conductivities, thermal annealing further enhanced them. The thermally annealed membranes, SF-5.4/5, SF-8.7/8, and SF-12.7/11.7, achieved higher proton conductivities of 0.12, 0.129, and 0.131 $Scm^{-1}$ compared with 0.112, 0.118, and 0.127 $Scm^{-1}$ of their pristine counterparts at corresponding $IEC_w$ values, respectively. Nevertheless, the increase in the proton conductivity of SF-X/Y_ann was not caused by the difference in $IEC_w$. $IEC_v$, which is the concentration of the sulfonic acid group per unit volume, was plotted as a function of $IEC_w$, as shown in Figure 2.13, and SF-X/Y_ann exhibited higher $IEC_v$ than did SF-X/Y. Thermal annealing can modify a membrane into a more densified configuration of sulfonic acid groups by reducing the spatial proximity of the neighboring acid groups, which could increase the proton conductivity while suppressing the excessive swelling behavior.

$\mu_{eff}$ was investigated (Figure 2.20b) to examine the effect of thermal annealing quantitatively and extensively on the development of a proton transport channel. $\mu_{eff}$ is a normalized value of proton conductivity from which the effect of the acid concentration has been removed [64]. One of the valuable factors that affect $\mu_{eff}$ is the water content of the membrane [65]. To eliminate this factor, $\mu_{eff}$ was examined as a function of $\lambda$, which is the number of water molecules per sulfonic acid group.

By analyzing $\mu_{eff}$ as a function of $\lambda$, other factors, such as the dissociation of acid from $SO_3^-$, tortuosity, and the spatial proximity of the membrane morphology, which affected $\mu_{eff}$, were considered [66]. SF-X/Y and SF-X/Y_ann exhibited $\mu_{eff}$ of 0.68–0.96 $cm^2s^{-1}V^{-1}$, while Nafion 212 and BPSH 50 exhibited $\mu_{eff}$ of 0.66 and 0.8 $cm^2s^{-1}V^{-1}$, respectively. Noteworthily, at $\lambda$ of almost 1/3, SF-X/Y and SF-X/Y_ann exhibited higher $\mu_{eff}$ compared with BPSH 50, inferring that the multiblock copolymer membranes possessed a better acid dissociation degree and a more favorable membrane morphology than the random copolymer (BPSH 50). SF-X/Y_ann exhibited higher $\mu_{eff}$ than those of pristine membranes at the same $\lambda$. At 21 mol $H_2O$ $mol^{-1}$ $–SO_3H$, SF-X/Y exhibited an estimated $\mu_{eff}$ of 0.86 $cm^2$ $s^{-1}V^{-1}$, while SF-X/Y_ann exhibited an estimated $\mu_{eff}$ of 0.90 $cm^2$ $s^{-1}V^{-1}$. Since the extents of the dissociation of the acid groups in SF-X/Y and SF-X/Y_ann were similar, it was inferred that the morphology of the thermally modified membrane exhibited better connectivity and closer proximity with the neighboring acid groups through the densification of the sulfonic acid groups.

## Proton conductivity under low humidification

Previous analyses of the morphology, water uptake, $IEC_v$, proton conductivity, and $\mu_{eff}$ of SF-X/Y multiblock copolymers have established that they possess well-connected proton-conducting channels with highly nanophase-separated structures, and this effect could be amplified by annealing. To determine if these beneficial features could ensure the desired proton conductivity in a high-temperature/low-humidity environment, the proton conductivities of SF-X/Y and SF-X/Y_ann were measured at 80 °C, while the humidity conditions were changed from RH of 30% to 70%. As shown in Figure 2.21, the proton conductivities of SF-X/Y and SF-X/Y_ann increased with increasing $IEC_w$ under the humidity conditions. Notably, SF-X/Y and SF-X/Y_ann exhibited higher proton conductivities than did BPSH 50, even at RH of 30%. BPSH 50 exhibited proton conductivity of 2.3 $mScm^{-1}$, while SF-5.4/5, the lowest conducting membrane among the SF-X/Y membranes, exhibited a 2.1-fold higher proton conductivity (4.7 $mScm^{-1}$). Particularly, SF-5.4/5 with $IEC_w$ of 1.67 $meqg^{-1}$ exhibited proton conductivity, which was 1.6–2.1 times higher than that of a random copolymer (BPSH 50) with $IEC_w$ of 1.96 $meqg^{-1}$ in all the humidity ranges. Moreover, SF-12.7/11.7 exhibited higher proton conductivity than perfluorinated Nafion 212 at RH of 40% and above.

Similar to the analysis of the proton conductivity under full humidification, thermal annealing further improved the proton conductivity of the membrane under reduced humidity conditions. Particularly, the proton conductivity of SF-5.4/5_ann with the lowest block length was significantly improved by thermal annealing. At RH of 30%–70%, the proton conductivity of SF-5.4/5 was 4.7-75.8 $mScm^{-1}$, whereas that of SF-5.4/5_ann was 8.1–89.1 mScm$^{-1}$, which was an approximately 1.4-fold improvement at RH of 50%. Regarding SF-X/Y_ann with a higher block length, a relatively moderate improvement in its proton conductivity was confirmed after thermal annealing. Nevertheless, SF-12.7/11.7_ann notably exhibited very good proton conductivity under all the measured humidity conditions. Additionally, SF_12.7/11.7_ann exhibited almost the same proton conductivity level (10.1 mScm$^{-1}$) as those of the state-of-the-art fluorine-based Nafion 212 (10.5 mScm$^{-1}$) even under a low humidity condition (30%).

## Interfacial bonding strength

A proper interface configuration between the membrane and electrodes is an essential prerequisite for improving fuel cell performance. Although excellent properties have been occasionally observed from employing non-perfluorinated membranes as PEMs [67], their applications as ionomers in electrodes are still limited. We assumed that this was caused by the severely low gas permeability, which caused an insufficient transfer of gas in the electrode layer [68]. Therefore, perfluorinated ionomers must still be utilized as the ionomer binders even after applying non-fluorinated PEM. However, existing hydrocarbon-based PEMs are known to exhibit very poor compatibility with the perfluorinated ionomer binder in the electrode layer [69]. Thus, the development of a strong membrane–electrode interface is challenging, and this could hinder the performance of the fuel cell. In this study, SF-X/Y was expected to exhibit improved interfacial properties with the perfluorinated ionomer binder in MEA owing to the presence of the fluorinated structure of PFCB in the hydrophobic block.

To quantitatively analyze the compatibility of our membrane with the perfluorinated polymer, SF-12.7/11.7 and Nafion 212 were hot-pressed at the same temperature (130 °C) and pressure (100 kgfcm$^{-2}$) under the MEA transfer condition, and the interfacial bonding strength was investigated by the T-peel test [70]. For comparison, BPSH 50 and Nafion 212 were also hot-pressed against the studied Nafion 212. The membrane containing BPSH 50 without a fluorine-based structure exhibited a negligible adhesion strength (0 mNcm$^{-1}$ averagely), whereas SF-12.7/11.7 exhibited a significantly higher adhesion strength (32.7 mNcm$^{-1}$) (the first sample in SF-12.7/11.7), as shown in Figure 2.22. Although the adhesion strength of SF-12.7/11.7 was lower than that (the first sample in Nafion 212) of the perfluorinated Nafion 212 (37.6 mNcm$^{-1}$), there was a considerable increase in the adhesion strength of SF-12.7/11.7 compared with that of an existing hydrocarbon-based membrane (BPSH 50). This result confirmed that the compatibility of SF-12.7/11.7 with the binder in the electrode layer increased after the introduction of a fluorinated structure. The structural affinity of partially fluorinated SF-X/Y with the perfluorosulfonated binder of the electrode could enhance the interfacial compatibility and reduce the interfacial resistance during the operation of the fuel cell.

## Fuel cell performance

The current–voltage polarization curves of SF-12.7/11.7, SF-12.7/11.7_ann, Nafion 212, and Nafion 211 were drawn (Figure 2.23). The membranes were fabricated into MEAs by the catalyst-coated membrane (CCM) method. At RH of 100%, SF-12.7/11.7 (1.04 $\mathrm{Acm^{-2}}$ compared at 0.6 V hereafter) and SF-12.7/11.7_ann MEAs (1.13 $\mathrm{Acm^{-2}}$) demonstrated better fuel cell performances than did Nafion 212 MEA (1.02 $\mathrm{Acm^{-2}}$). Further, the performance of SF-12.7/11.7_ann MEA was similar to that of Nafion 211 MEA (1.21 $\mathrm{Acm^{-2}}$). At RH of 50%, SF-12.7/11.7 (0.48 $\mathrm{Acm^{-2}}$) and SF-12.7/11.7_ann (0.61 $\mathrm{Acm^{-2}}$) also exhibited better fuel cell performances than did Nafion 212 (0.46 $\mathrm{Acm^{-2}}$). Furthermore, Nafion 211 achieved a slightly higher performance (0.69 $\mathrm{Acm^{-2}}$) than the SF membranes.

Although SF-X/Y and SF-X/Y_ann exhibited higher proton conductivity than the Nafion membranes, the results of their fuel cell performances were similar. Electrochemical impedance spectroscopy (EIS) was performed to compare the SF membranes with Nafion 211 MEAs (Figure 2.24). In the Nyquist plot, the bulk resistance ($R_b$) in the high-frequency region is proportional to the membrane resistance, whereas the charge-transfer resistance ($R_{ct}$) is mainly determined by the interfacial properties of the membrane and electrodes. SF-12.7/11.7 MEA exhibited a lower $R_b$ than did Nafion 211 MEA because of its smaller membrane resistance. $R_{ct}$ of SF-12.7/11.7 MEA was 1.1-fold higher than that of Nafion 211. Despite the low $R_b$, SF-12.7/11.7 MEA demonstrated limited interfacial compatibility at the membrane–electrode interface, which increased $R_{ct}$, compared with perfluorinated Nafion 211. Although the interfacial compatibility was improved by the incorporation of a partially fluorinated structure, we admit that the interfacial compatibility between the perfluorinated ionomer binders in MEA was insufficient compared with that in Nafion. Thus, further research is required to resolve this limitation.

As the thickness of Nafion decreased, the fuel cell performance improved. Figure 2.23a showed the fuel cell performance of Nafion 211 MEA, and the value is almost as close as the performance of SF-12.7/11.7 MEA. The EIS analysis (Figure 2.24) of the unit cell was performed to analyze the reason behind SF-12.7/11.7 exhibiting similar performance compared to Nafion 211 despite the higher proton conductivity. The x-intercept in the high frequency region represents the bulk resistance ($R_b$), which is known to be proportional to membrane resistance. On the other hand, the size of the semicircle is the charge transfer resistance ($R_{ct}$), which is mainly determined from the interfacial properties of the membrane and the electrode. The x-intercept of SF-12.7/11.7 observed in the high frequency region is smaller than that of Nafion 211, indicating the $R_b$, mainly the membrane resistance, is smaller than that of Nafion 211. This confirms that SF-12.7/11.7 has lower $R_b$ compared to Nafion 211 as expected. The diameter of the semicircle is 1.1-fold larger for SF-12.7/11.7 than that of Nafion 211, indicating the $R_{ct}$, which arises from the interface between the membrane and the electrode, is larger than that of Nafion 211. Even though SF-12.7/11.7 exhibits smaller membrane resistance than Nafion 211, the $R_{ct}$ generated at the membrane-electrode interface is higher than that of Nafion 211. As a result, the two membranes exhibit similar fuel cell performance.

Although SF-12.7/11.7 is partially fluorinated, thus better interfacial compatibility to the perfluorinated binder than hydrocarbon-based membrane is assumed, it still shows limitation when compared to perfluorinated membrane such as Nafion 211. To fabricate membrane electrode assembly (MEA), perfluorinated ionomer binder is used in the electrode layer to ensure sufficient gas transfer in the electrode layer. However, the perfluorinated ionomer has limited interfacial compatibility to non-perfluorinated membranes. In this paper, we attempted to reduce interfacial resistance by incorporating partially fluorinated structure. From the previous discussions, we drew a conclusion that the PFCB containing structure has helped interfacial compatibility to perfluorinated structure, Nafion, in some level. However, despite our effort of incorporating partially fluorinated structure, we admit the limitation of having insufficient compatibility between the perfluorinated ionomer binders in MEA compared to Nafion.

## Chemical and physical durabilities

The OCV hold test is an accelerated in situ chemical durability test for fuel cells, which is conducted under OCV conditions in an actual fuel cell. SF-12.7/11.7 endured >1000 h of the OCV hold test (Figure 2.25a), which is significant compared with 175–280 h endured by perfluorinated Nafion 212 [71, 72] and 750 h by random copolymer [73].

The current density of the hydrogen permeability of SF-12.7/11.7 was obtained under wet/dry cycling conditions employing LSV measurements (Figure 2.25b). SF-12.7/11.7 maintained a current density of $\leq 2$ mAcm$^{-2}$ until 8080 cycles, although the current density exceeded 10 mAcm$^{-2}$ at 10,000 cycles due to the deterioration of the interface between the membrane and electrodes. Put differently, the membrane maintained physical durability for up to 8080 cycles, after which it failed, indicating that its physical durability requires further improvement. Nevertheless, SF-12.7/11.7 exhibited relatively high physical durability among the hydrocarbon-containing PEMs [68, 72, 74, 75]. For example, the physical durability of the SPAES-50 random copolymer, which was prepared by this research team, was evaluated under similar conditions, and the failure of the membrane was observed within 290 cycles [74].

## 2.4. Conclusion

Multiblock copolymers with distinct phase separation between their highly sulfonated sPPSS hydrophilic and fluorinated BP_PFCB hydrophobic moieties were fabricated to deliver high proton conductivities under low humidity conditions and to eventually achieve high fuel cell performance. Additionally, low $T_g$ ensured that thermal annealing was possible at a low temperature because of the presence of the flexible ether and PFCB groups, which afforded great freedom for chain mobility, thus causing the desirable aggregation of $SO_3H$. The SF-X/Y multiblock copolymers were synthesized with high molecular weights of >1 $dLg^{-1}$ and $IEC_w$ of 1.67–2.01 $meqg^{-1}$. Compared with hydrocarbon-based PEMs (BPSH 50), SF-X/Y and SF-X/Y_ann demonstrated higher proton conductivity even with lower-dimensional swelling and water uptake owing to the effective hydrophilic/hydrophobic phase separation, which was observed in the TEM images. Further, the membrane was modified via thermal annealing to maximize the densification of the sulfonic acid groups, thereby achieving higher proton conductivity while maintaining lower or similar dimensional swelling compared with those of the pristine SF-X/Y membranes. SF-X/Y and SF-X/Y_ann exhibited proton conductivity (as high as 41.9 $mScm^{-1}$) under a low humidity condition (50%). The structural affinity of the partially fluorinated membrane for the perfluorosulfonated binder of the electrode generated a reasonable interfacial bonding strength in the membrane–electrode interface. The high proton conductivity with interfacial compatibility enhanced the performance of the fuel cell (SF-12.7/11.7_ann = 1.13 Acm$^{-2}$ at 0.6 V, 65 °C, and 100% RH) and delivered stable chemical and physical durabilities.

## 2.5. References

[1] I. Burch, J. Gilchrist, Survey of global activity to phase out internal combustion engine vehicles, in, Center of Climate Protection, Santa Rosa, CA, USA, 2020.

[2] N. Li, D.W. Shin, D.S. Hwang, Y.M. Lee, M.D. Guiver, Polymer Electrolyte Membranes Derived from New Sulfone Monomers with Pendent Sulfonic Acid Groups, Macromolecules, 43 (2010) 9810-9820.

[3] N. Li, M.D. Guiver, Ion Transport by Nanochannels in Ion-Containing Aromatic Copolymers, Macromolecules, 47 (2014) 2175-2198.

[4] J. Han, K. Kim, J. Kim, S. Kim, S.-W. Choi, H. Lee, J.-j. Kim, T.-H. Kim, Y.-E. Sung, J.-C. Lee, Cross-linked highly sulfonated poly(arylene ether sulfone) membranes prepared by in-situ casting and thiol-ene click reaction for fuel cell application, Journal of Membrane Science, 579 (2019) 70-78.

[5] H. Lee, J. Han, K. Kim, J. Kim, E. Kim, H. Shin, J.-C. Lee, Highly sulfonated polymer-grafted graphene oxide composite membranes for proton exchange membrane fuel cells, Journal of Industrial and Engineering Chemistry, 74 (2019) 223-232.

[6] K. Nakabayashi, K. Matsumoto, M. Ueda, Synthesis and properties of sulfonated multiblock copoly(ether sulfone)s by a chain extender, Journal of Polymer Science Part A: Polymer Chemistry, 46 (2008) 3947-3957.

[7] J. Fang, X. Guo, S. Harada, T. Watari, K. Tanaka, H. Kita, K.-i. Okamoto, Novel Sulfonated Polyimides as Polyelectrolytes for Fuel Cell Application. 1. Synthesis, Proton Conductivity, and Water Stability of Polyimides from 4,4‘-Diaminodiphenyl Ether-2,2‘-disulfonic Acid, Macromolecules, 35 (2002) 9022-9028.

[8] Z. Hu, Y. Yin, S. Chen, O. Yamada, K. Tanaka, H. Kita, K.-I. Okamoto, Synthesis and properties of novel sulfonated (co)polyimides bearing sulfonated aromatic pendant groups for PEFC applications, Journal of Polymer Science Part A: Polymer Chemistry, 44 (2006) 2862-2872.

[9] F. Wang, M. Hickner, Y.S. Kim, T.A. Zawodzinski, J.E. McGrath, Direct polymerization of sulfonated poly(arylene ether sulfone) random (statistical) copolymers: candidates for new proton exchange membranes, Journal of Membrane Science, 197 (2002) 231-242.

[10] T. Kobayashi, M. Rikukawa, K. Sanui, N. Ogata, Proton-conducting polymers derived from poly(ether-etherketone) and poly(4-phenoxybenzoyl-1,4-phenylene), Solid State Ionics, 106 (1998) 219-225.

[11] B. Liu, G.P. Robertson, D.-S. Kim, M.D. Guiver, W. Hu, Z. Jiang, Aromatic Poly(ether ketone)s with Pendant Sulfonic Acid Phenyl Groups Prepared by a Mild Sulfonation Method for Proton Exchange Membranes, Macromolecules, 40 (2007) 1934-1944.

[12] K.-D. Kreuer, Membrane Materials for PEM-Fuel-Cells: A Microstructural

Approach, ECS Proceedings Volumes, 1995-23 (1995) 241-246.

[13] S. Martin, P.L. Garcia-Ybarra, J.L. Castillo, Long-term operation of a proton exchange membrane fuel cell without external humidification, Applied Energy, 205 (2017) 1012-1020.

[14] G. Wang, Y. Yu, H. Liu, C. Gong, S. Wen, X. Wang, Z. Tu, Progress on design and development of polymer electrolyte membrane fuel cell systems for vehicle applications: A review, Fuel Processing Technology, 179 (2018) 203-228.

[15] T.J. Peckham, S. Holdcroft, Structure-Morphology-Property Relationships of Non-Perfluorinated Proton-Conducting Membranes, Advanced Materials, 22 (2010) 4667-4690.

[16] T. Higashihara, K. Matsumoto, M. Ueda, Sulfonated aromatic hydrocarbon polymers as proton exchange membranes for fuel cells, Polymer, 50 (2009) 5341-5357.

[17] N. Li, J. Liu, Z. Cui, S. Zhang, W. Xing, Novel hydrophilic–hydrophobic multiblock copolyimides as proton exchange membranes: Enhancing the proton conductivity, Polymer, 50 (2009) 4505-4511.

[18] X. Guo, W. Li, J. Fang, Y. Yin, Synthesis and properties of novel multiblock copolyimides consisting of benzimidazole-groups-containing sulfonated polyimide hydrophilic blocks and non-sulfonated polyimide hydrophobic blocks as proton exchange membranes, Electrochimica Acta, 177 (2015) 151-160.

[19] H.-S. Lee, A. Roy, O. Lane, S. Dunn, J.E. McGrath, Hydrophilic–hydrophobic multiblock copolymers based on poly(arylene ether sulfone) via low-temperature coupling reactions for proton exchange membrane fuel cells, Polymer, 49 (2008) 715-723.

[20] J. Yuk, S. Lee, A.F. Nugraha, H. Lee, S.-H. Park, S.-D. Yim, B. Bae, Synthesis and characterization of multi-block poly(arylene ether sulfone) membranes with highly sulfonated blocks for use in polymer electrolyte membrane fuel cells, Journal of Membrane Science, 518 (2016) 50-59.

[21] B. Bae, K. Miyatake, M. Watanabe, Sulfonated Poly(arylene ether sulfone ketone) Multiblock Copolymers with Highly Sulfonated Block. Synthesis and Properties, Macromolecules, 43 (2010) 2684-2691.

[22] C. Liang, T. Maruyama, Y. Ohmukai, T. Sotani, H. Matsuyama, Characterization of random and multiblock copolymers of highly sulfonated poly(arylene ether sulfone) for a proton-exchange membrane, Journal of Applied Polymer Science, 114 (2009) 1793-1802.

[23] Y. Chang, G.F. Brunello, J. Fuller, M. Hawley, Y.S. Kim, M. Disabb-Miller, M.A. Hickner, S.S. Jang, C. Bae, Aromatic Ionomers with Highly Acidic Sulfonate Groups: Acidity, Hydration, and Proton Conductivity, Macromolecules, 44 (2011) 8458-8469.

[24] M. Schuster, K.-D. Kreuer, H.T. Andersen, J. Maier, Sulfonated

Poly(phenylene sulfone) Polymers as Hydrolytically and Thermooxidatively Stable Proton Conducting Ionomers, Macromolecules, 40 (2007) 598-607.

[25] M. Schuster, T. Rager, A. Noda, K.D. Kreuer, J. Maier, About the Choice of the Protogenic Group in PEM Separator Materials for Intermediate Temperature, Low Humidity Operation: A Critical Comparison of Sulfonic Acid, Phosphonic Acid and Imidazole Functionalized Model Compounds, Fuel Cells, 5 (2005) 355-365.

[26] D.W. Shin, M.D. Guiver, Y.M. Lee, Hydrocarbon-Based Polymer Electrolyte Membranes: Importance of Morphology on Ion Transport and Membrane Stability, Chemical Reviews, 117 (2017) 4759-4805.

[27] S. Munekata, Fluoropolymers as coating material, Progress in Organic Coatings, 16 (1988) 113-134.

[28] D.S. Kim, G.P. Robertson, M.D. Guiver, Y.M. Lee, Synthesis of highly fluorinated poly(arylene ether)s copolymers for proton exchange membrane materials, Journal of Membrane Science, 281 (2006) 111-120.

[29] A.S. Badami, O. Lane, H.-S. Lee, A. Roy, J.E. McGrath, Fundamental investigations of the effect of the linkage group on the behavior of hydrophilic–hydrophobic poly(arylene ether sulfone) multiblock copolymers for proton exchange membrane fuel cells, Journal of Membrane Science, 333 (2009) 1-11.

[30] T. Mochizuki, M. Uchida, K. Miyatake, Simple, Effective Molecular Strategy

for the Design of Fuel Cell Membranes: Combination of Perfluoroalkyl and Sulfonated Phenylene Groups, ACS Energy Letters, 1 (2016) 348-352.

[31] X. Chen, H. Lü, Q. Lin, X. Zhang, D. Chen, Y. Zheng, Partially fluorinated poly(arylene ether)s bearing long alkyl sulfonate side chains for stable and highly conductive proton exchange membranes, Journal of Membrane Science, 549 (2018) 12-22.

[32] L. Assumma, H.-D. Nguyen, C. Iojoiu, S. Lyonnard, R. Mercier, E. Espuche, Effects of Block Length and Membrane Processing Conditions on the Morphology and Properties of Perfluorosulfonated Poly(arylene ether sulfone) Multiblock Copolymer Membranes for PEMFC, ACS Applied Materials & Interfaces, 7 (2015) 13808-13820.

[33] P. Gode, J. Ihonen, A. Strandroth, H. Ericson, G. Lindbergh, M. Paronen, F. Sundholm, G. Sundholm, N. Walsby, Membrane Durability in a PEM Fuel Cell Studied Using PVDF Based Radiation Grafted Membranes, Fuel Cells, 3 (2003) 21-27.

[34] Y. Yang, Z. Shi, S. Holdcroft, Synthesis of poly[arylene ether sulfone-b-vinylidene fluoride] block copolymers, European Polymer Journal, 40 (2004) 531-541.

[35] Y. Chen, J.R. Rowlett, C.H. Lee, O.R. Lane, D.J. VanHouten, M. Zhang, R.B. Moore, J.E. McGrath, Synthesis and characterization of multiblock partially

fluorinated hydrophobic poly(arylene ether sulfone)-hydrophilic disulfonated poly(arylene ether sulfone) copolymers for proton exchange membranes, Journal of Polymer Science Part A: Polymer Chemistry, 51 (2013) 2301-2310.

[36] J. Ahn, R. Shimizu, K. Miyatake, Sulfonated aromatic polymers containing hexafluoroisopropylidene groups: a simple but effective structure for fuel cell membranes, Journal of Materials Chemistry A, 6 (2018) 24625-24632.

[37] Z. Shi, S. Holdcroft, Synthesis and Proton Conductivity of Partially Sulfonated Poly([vinylidene difluoride-co-hexafluoropropylene]-b-styrene) Block Copolymers, Macromolecules, 38 (2005) 4193-4201.

[38] O. Danyliv, C. Gueneau, C. Iojoiu, L. Cointeaux, A. Thiam, S. Lyonnard, J.-Y. Sanchez, Polyaromatic ionomers with a highly hydrophobic backbone and perfluorosulfonic acids for PEMFC, Electrochimica Acta, 214 (2016) 182-191.

[39] T. Okazoe, Overview on the history of organofluorine chemistry from the viewpoint of material industry, Proc Jpn Acad Ser B Phys Biol Sci, 85 (2009) 276-289.

[40] D.W. Smith, D.A. Babb, H.V. Shah, A. Hoeglund, R. Traiphol, D. Perahia, H.W. Boone, C. Langhoff, M. Radler, Perfluorocyclobutane (PFCB) polyaryl ethers: versatile coatings materials, Journal of Fluorine Chemistry, 104 (2000) 109-117.

[41] B. Farajidizaji, K.E. Shelar, G. Narayanan, K.M. Mukeba, B. Donnadieu, C.U. Pittman Jr, A. Sygula, D.W. Smith Jr, Acenaphthylene-derived perfluorocyclobutyl

aromatic ether polymers, Journal of Polymer Science Part A: Polymer Chemistry, 57 (2019) 1270-1274.

[42] J. Zhou, Y. Tao, X. Chen, X. Chen, L. Fang, Y. Wang, J. Sun, Q. Fang, Perfluorocyclobutyl-based polymers for functional materials, Materials Chemistry Frontiers, 3 (2019) 1280-1301.

[43] D.-J. Kim, B.-J. Chang, J.-H. Kim, S.-B. Lee, H.-J. Joo, Sulfonated poly(fluorenyl ether) membranes containing perfluorocyclobutane groups for fuel cell applications, Journal of Membrane Science, 325 (2008) 217-222.

[44] D.W. Smith, D.A. Babb, Perfluorocyclobutane Aromatic Polyethers. Synthesis and Characterization of New Siloxane-Containing Fluoropolymers, Macromolecules, 29 (1996) 852-860.

[45] G. Qian, D.W. Smith, B.C. Benicewicz, Synthesis and characterization of high molecular weight perfluorocyclobutyl-containing polybenzimidazoles (PFCB–PBI) for high temperature polymer electrolyte membrane fuel cells, Polymer, 50 (2009) 3911-3916.

[46] K.-S. Lee, M.-H. Jeong, Y.-J. Kim, S.-B. Lee, J.-S. Lee, Fluorinated Aromatic Polyether Ionomers Containing Perfluorocyclobutyl as Cross-Link Groups for Fuel Cell Applications, Chemistry of Materials, 24 (2012) 1443-1453.

[47] S.-B. Lee, Y.-J. Kim, U. Ko, C.-M. Min, M.-K. Ahn, S.-J. Chung, I.-S. Moon, J.-S. Lee, Sulfonated poly(arylene ether) membranes containing

perfluorocyclobutyl and ethynyl groups: Increased mechanical strength through chain extension and crosslinking, Journal of Membrane Science, 456 (2014) 49-56.

[48] G.J.D. Kalaw, J.A.N. Wahome, Y. Zhu, K.J. Balkus, I.H. Musselman, D.-J. Yang, J.P. Ferraris, Perfluorocyclobutyl (PFCB)-based polymer blends for proton exchange membrane fuel cells (PEMFCs), Journal of Membrane Science, 431 (2013) 86-95.

[49] J. Hong, L. Bi, S. Li, G. Jia, Y. Zhu, G. Li, Z. Huang, Design and synthesis of reactive polymers containing perfluorocyclobutyl (PFCB) and hydroxyl moieties for post-functionalization of PFCB aryl ether polymers, Polymer, 93 (2016) 37-43.

[50] S.-Y. Moon, J.-H. Kim, B.-J. Chang, Branched poly(biphenylene-co-sulfone)ether ion exchange membranes containing perfluorocyclobutane groups for fuel cell applications, Journal of Applied Polymer Science, 137 (2020) 48373.

[51] C. Marestin, X. Thiry, S. Rojo, E. Chauveau, R. Mercier, Synthesis of sulfonate ester and sulfonic acid-containing poly(arylene perfluorocyclobutane)s (PFCB) by direct copolymerization of a sulfonate ester-containing precursor, Polymer, 108 (2017) 179-192.

[52] R. Jiang, T. Fuller, S. Brawn, C. Gittleman, Perfluorocyclobutane and poly(vinylidene fluoride) blend membranes for fuel cells, Electrochimica Acta, 110 (2013) 306-315.

[53] M. Ueda, H. Toyota, T. Ouchi, J.-I. Sugiyama, K. Yonetake, T. Masuko, T.

Teramoto, Synthesis and characterization of aromatic poly(ether sulfone)s containing pendant sodium sulfonate groups, Journal of Polymer Science Part A: Polymer Chemistry, 31 (1993) 853-858.

[54] N. Li, S.Y. Lee, Y.-L. Liu, Y.M. Lee, M.D. Guiver, A new class of highly-conducting polymer electrolyte membranes: Aromatic ABA triblock copolymers, Energy & Environmental Science, 5 (2012) 5346-5355.

[55] X. Yu, A. Roy, S. Dunn, A.S. Badami, J. Yang, A.S. Good, J.E. McGrath, Synthesis and characterization of sulfonated-fluorinated, hydrophilic-hydrophobic multiblock copolymers for proton exchange membranes, Journal of Polymer Science Part A: Polymer Chemistry, 47 (2009) 1038-1051.

[56] T. Wang, T. Li, J. Aboki, R. Guo, Disulfonated Poly(arylene ether sulfone) Random Copolymers Containing Hierarchical Iptycene Units for Proton Exchange Membranes, Frontiers in Chemistry, 8 (2020) 674.

[57] C. Sinturel, M. Vayer, M. Morris, M.A. Hillmyer, Solvent Vapor Annealing of Block Polymer Thin Films, Macromolecules, 46 (2013) 5399-5415.

[58] Y. Chen, R. Guo, C.H. Lee, M. Lee, J.E. McGrath, Partly fluorinated poly(arylene ether ketone sulfone) hydrophilic–hydrophobic multiblock copolymers for fuel cell membranes, International Journal of Hydrogen Energy, 37 (2012) 6132-6139.

[59] C.H. Lee, K.-S. Lee, O. Lane, J.E. McGrath, Y. Chen, S. Wi, S.Y. Lee, Y.M.

Lee, Solvent-assisted thermal annealing of disulfonated poly(arylene ether sulfone) random copolymers for low humidity polymer electrolyte membrane fuel cells, RSC Advances, 2 (2012) 1025-1032.

[60] J. Ghim, H.-S. Shim, B.G. Shin, J.-H. Park, J.-T. Hwang, C. Chun, S.-H. Oh, J.-J. Kim, D.-Y. Kim, Isomer Structure−Optical Property Relationships for Naphthalene-Based Poly(perfluorocyclobutyl ether)s, Macromolecules, 38 (2005) 8278-8284.

[61] F. Mack, K. Aniol, C. Ellwein, J. Kerres, R. Zeis, Novel phosphoric acid-doped PBI-blends as membranes for high-temperature PEM fuel cells, Journal of Materials Chemistry A, 3 (2015) 10864-10874.

[62] T.J. Peckham, J. Schmeisser, S. Holdcroft, Relationships of Acid and Water Content to Proton Transport in Statistically Sulfonated Proton Exchange Membranes: Variation of Water Content Via Control of Relative Humidity, The Journal of Physical Chemistry B, 112 (2008) 2848-2858.

[63] C.F. Kins, E. Sengupta, A. Kaltbeitzel, M. Wagner, I. Lieberwirth, H.W. Spiess, M.R. Hansen, Morphological Anisotropy and Proton Conduction in Multiblock Copolyimide Electrolyte Membranes, Macromolecules, 47 (2014) 2645-2658.

[64] M. Maalouf, C.-N. Sun, B. Pyle, M. Emery, G.M. Haugen, S.J. Hamrock, T.A. Zawodzinski, Factors enabling high mobility of protons and water in perfluorosulfonate membranes under low hydration conditions1, International

Journal of Hydrogen Energy, 39 (2014) 2795-2800.

[65] E. Spohr, P. Commer, A.A. Kornyshev, Enhancing Proton Mobility in Polymer Electrolyte Membranes: Lessons from Molecular Dynamics Simulations, The Journal of Physical Chemistry B, 106 (2002) 10560-10569.

[66] T.J. Peckham, J. Schmeisser, M. Rodgers, S. Holdcroft, Main-chain, statistically sulfonated proton exchange membranes: the relationships of acid concentration and proton mobility to water content and their effect upon proton conductivity, Journal of Materials Chemistry, 17 (2007) 3255-3268.

[67] S. Yuk, J. Yuk, T.-H. Kim, Y.T. Hong, D.-H. Lee, J. Hyun, S. Choi, G. Doo, D.W. Lee, H.-T. Kim, External reinforcement of hydrocarbon membranes by a three-dimensional interlocking interface for mechanically durable polymer electrolyte membrane fuel cells, Journal of Power Sources, 415 (2019) 44-49.

[68] S. Yuk, M.-J. Choo, D. Lee, H. Guim, T.-H. Kim, D.G. Lee, S. Choi, D.-H. Lee, G. Doo, Y.T. Hong, H.-T. Kim, Three-Dimensional Interlocking Interface: Mechanical Nanofastener for High Interfacial Robustness of Polymer Electrolyte Membrane Fuel Cells, Advanced Materials, 29 (2017) 1603056.

[69] S.-W. Nam, D.M. Yu, T.-H. Kim, J.Y. Lee, S.Y. Nam, Y.T. Hong, Synthesis and properties of bonding layer containing flexible and fluorinated moieties for hydrocarbon-based membrane electrode assemblies, International Journal of Hydrogen Energy, 41 (2016) 10884-10895.

[70] D.M. Yu, T.-H. Kim, J.Y. Lee, S. Yoon, Y.T. Hong, Thin bonding layer using sulfonated poly(arylene ether sulfone)/PVdF blends for hydrocarbon-based membrane electrode assemblies, Electrochimica Acta, 173 (2015) 268-275.

[71] V.D. Cong Tinh, D. Kim, Enhancement of oxidative stability of PEM fuel cell by introduction of HO• radical scavenger in Nafion ionomer, Journal of Membrane Science, 613 (2020) 118517.

[72] J.Y. Lee, D.M. Yu, T.-H. Kim, S.J. Yoon, Y.T. Hong, Multi-block copolymers based on poly(p-phenylene)s with excellent durability and fuel cell performance, Journal of Membrane Science, 492 (2015) 209-219.

[73] S. Park, H. Lee, S.-H. Shin, N. Kim, D. Shin, B. Bae, Increasing the Durability of Polymer Electrolyte Membranes Using Organic Additives, ACS Omega, 3 (2018) 11262-11269.

[74] D.M. Yu, S.-W. Nam, S. Yoon, T.-H. Kim, J.Y. Lee, S.Y. Nam, Y.T. Hong, Edge protection using polyacrylonitrile thin-films for hydrocarbon-based membrane electrode assemblies, Journal of Industrial and Engineering Chemistry, 28 (2015) 190-196.

[75] H.Y. Jeong, D.-S. Yang, J.H. Han, J.Y. Lee, S. So, D.H. Suh, S.K. Hong, Y.T. Hong, T.-H. Kim, Novel interfacial bonding layers with controlled gradient composition profile for hydrocarbon-based membrane electrode assemblies, Journal of Power Sources, 398 (2018) 1-8.

**Table 2.1.** General properties of SF-X/Y, SF-X/Y_ann, Nafion 212, and BPSH 50

| **Samples** | **IV**[a] **($dLg^{-1}$)** | **IEC$_w$**[b] **($meqg^{-1}$)** | **IEC$_v$**[c] **($meqcm^{-3}$)** | **$\lambda$**[d] **(molH$_2$O mol$^{-1}$SO$_3$H)** | **Proton Conductivity ($mScm^{-1}$)** | |
|---|---|---|---|---|---|---|
| | | | | | **25 °C, RH 100%** | **80 °C, RH 50%** |
| **SF-5.4/5** | 2.20 | 1.67 | 2.26 | 13.45 | 112 | 24.3 |
| **SF-5.4/5_ann** | | | 2.38 | 11.45 | 120 | 34.0 |
| **SF-8.7/8** | 1.50 | 1.89 | 2.41 | 20.21 | 118 | 34.0 |
| **SF-8.7/8_ann** | | | 2.66 | 17.33 | 129 | 34.2 |
| **SF-12.7/11.7** | 1.60 | 2.01 | 2.58 | 25.35 | 127 | 38.3 |
| **SF-12.7/11.7_ann** | | | 2.81 | 23.14 | 131 | 41.9 |
| **Nafion 212** | - | 0.91 | 1.72 | 12.53 | 84 | 27.8 |
| **BPSH 50** | - | 1.96[e] | 2.48 | 32.60[e] | 109[e] | 13.1 |

[a] Measured at 25 °C

[b] Measured by acid titration

[c] IEC$_v$ = IEC$_w$ × density in the dry state

[d] Hydration number = [H$_2$O]/[SO$_3$–] at 25 °C

[e] The value was obtained from reference [56]

**Table 2.2.** Tensile strength and elongation of SF-X/Y and SF-X/Y_ann

| **Samples** | **Tensile Strength (MPa)** | **Elongation (%)** |
|---|---|---|
| **SF-5.4/5** | 48.59 | 11.56 |
| **SF-5.4/5_ann** | 50.80 | 7.79 |
| **SF-8.7/8** | 48.85 | 17.23 |
| **SF-8.7/8_ann** | 55.41 | 12.49 |
| **SF-12.7/11.7** | 47.19 | 23.27 |
| **SF-12.7/11.7_ann** | 53.38 | 20.77 |

**Table 2.3.** Oxidation stability of SF-X/Y, SF-X/Y_ann, and BPSH 50

| **Samples** | **$M_{\text{n initial}}$[a] (g mol$^{-1}$)** | **$M_{\text{n final}}$[b] (g mol$^{-1}$)** | **Reduction %[c]** |
|---|---|---|---|
| **SF-5.4/5** | 59754 | 23131 | −61.29 |
| **SF-5.4/5_ann** | | 2289 | −61.69 |
| **SF-8.7/8** | 52790 | 425996 | −50.76 |
| **SF-8.7/8_ann** | | 27452 | −48.00 |
| **SF-12.7/11.7** | 69729 | 23192 | −66.74 |
| **SF-12.7/11.7_ann** | | 27693 | −60.28 |
| **BPSH 50** | 115637 | 28602 | −75.27 |

[a] $M_{\text{n initial}} = M_n$ (GPC) before the Fenton test

[b] $M_{\text{n final}} = M_n$ (GPC) after the Fenton test

[c] Reduction % = $-(M_{\text{n initial}} - M_{\text{n final}})/(M_{\text{n initial}})$ x 100%

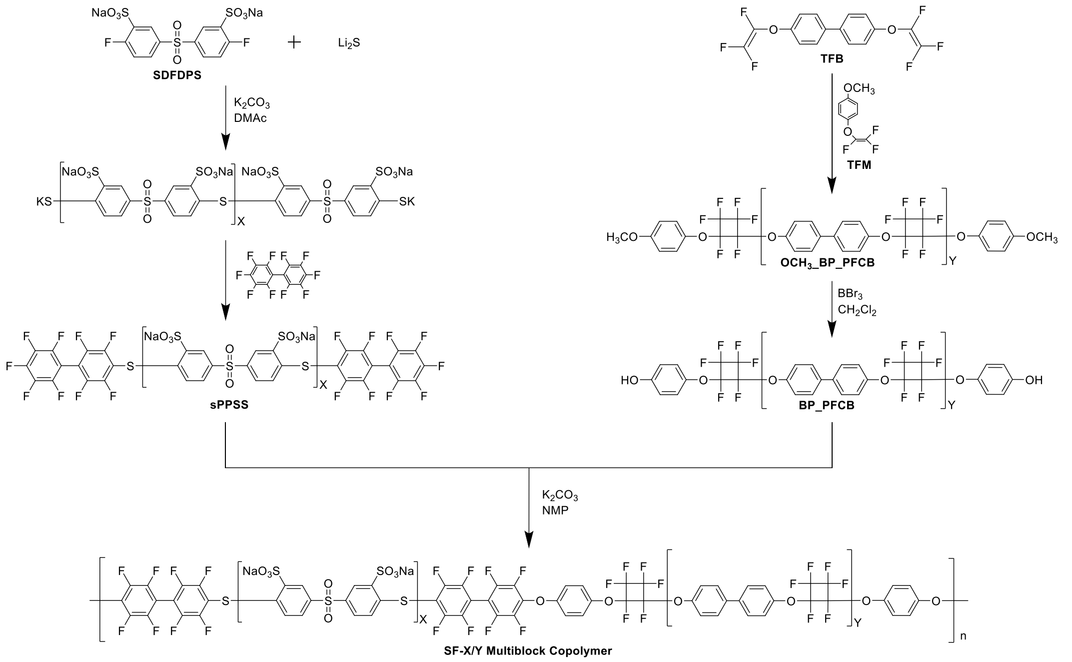

**Figure 2.1.** Synthesis of SF-X/Y multiblock copolymer

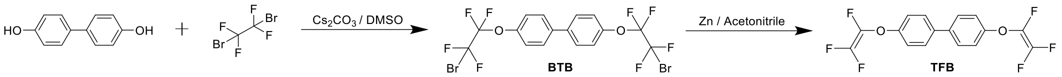

**Figure 2.2.** Synthesis of hydrophobic monomer: 4,4′-bis(trifluorovinyloxy)biphenyl (TFB)

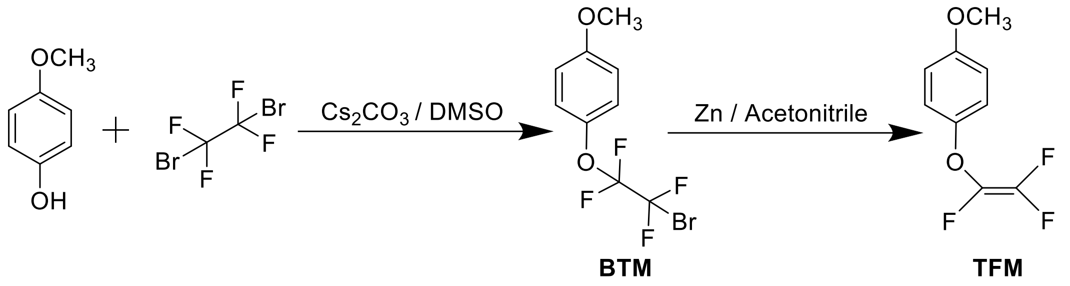

**Figure 2.3.** Synthesis of hydrophobic end-capper: 4-(trifluorovinyloxy)methoxybenzene (TFM)

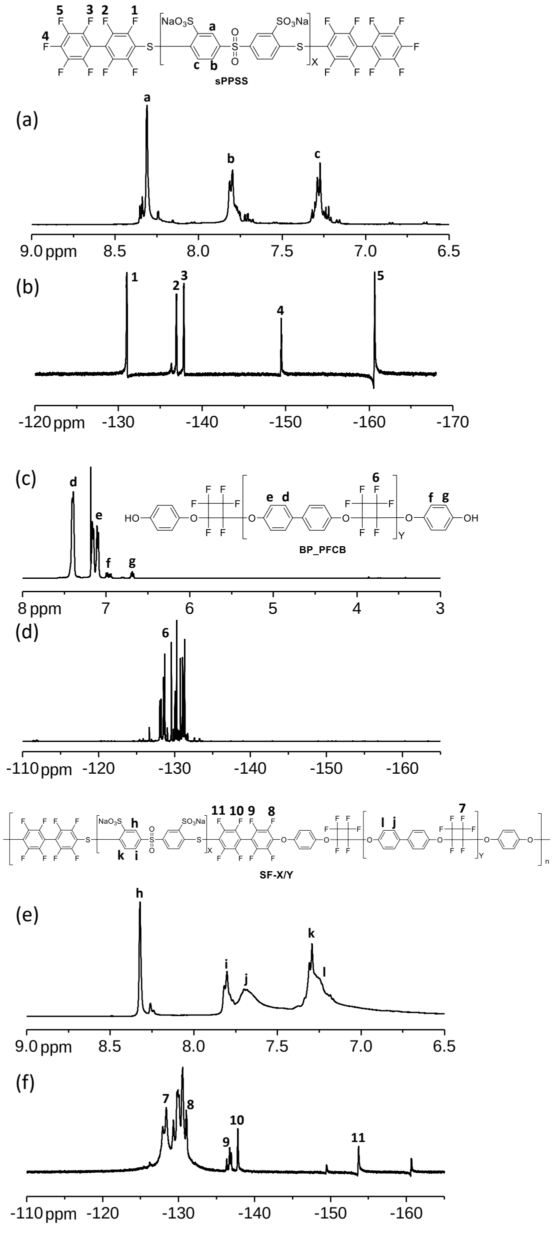

**Figure 2.4.** (a) $^1$H and (b) $^{19}$F NMR of the hydrophilic oligomer (sPPSS) (c) $^1$H and (d) $^{19}$F NMR of the hydrophobic oligomer (BP_PFCB) (e) $^1$H and (f) $^{19}$F NMR of the multiblock copolymer (SF-X/Y)

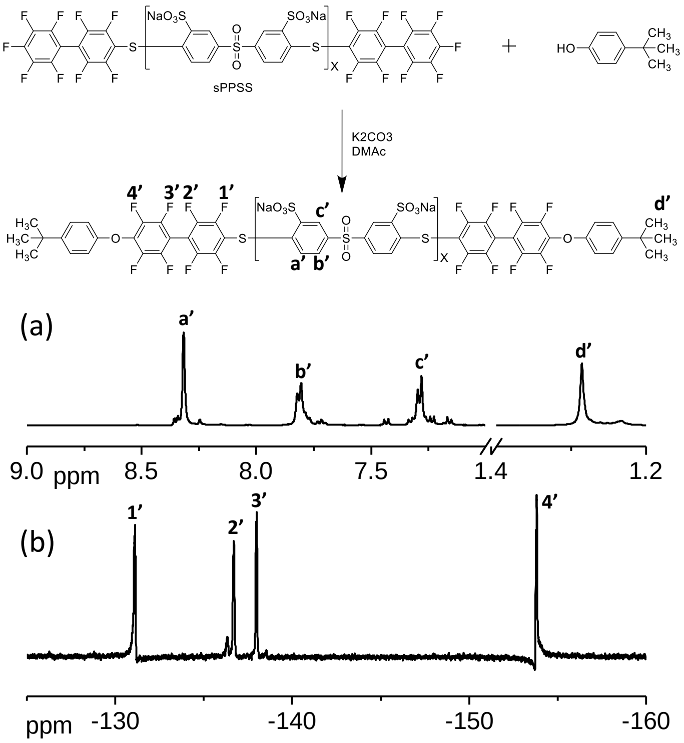

**Figure 2.5.** (a) $^1$H NMR and (b) $^{19}$F NMR of hydrophilic oligomer: sPPSS with end-capper

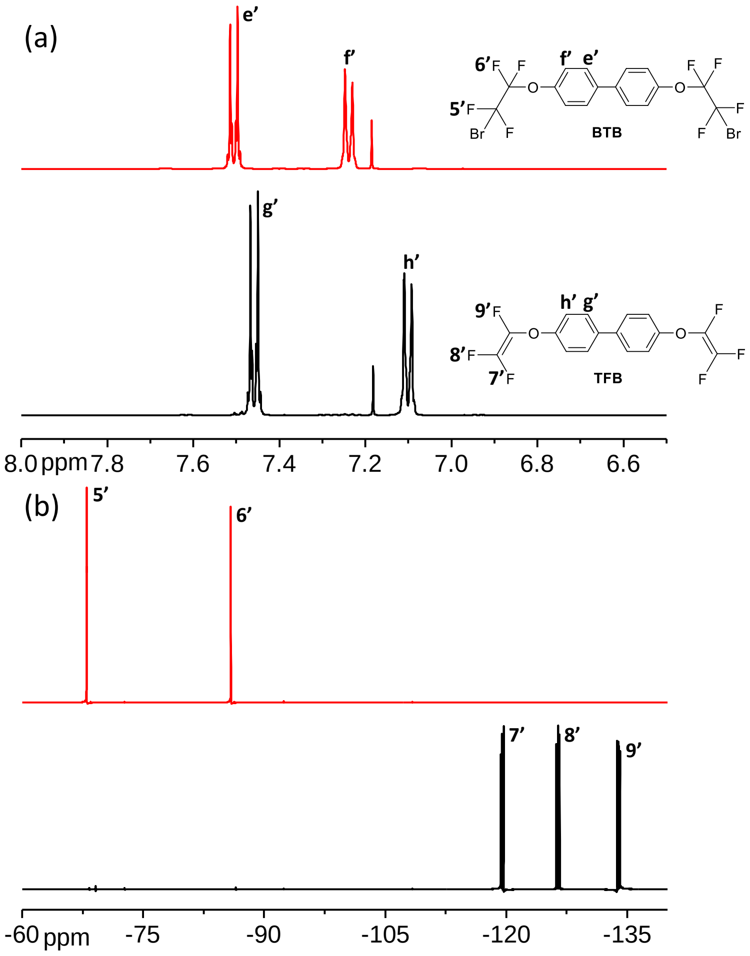

**Figure 2.6.** (a) $^{1}$H NMR and (b) $^{19}$F NMR of hydrophobic monomer: BTB and TFB

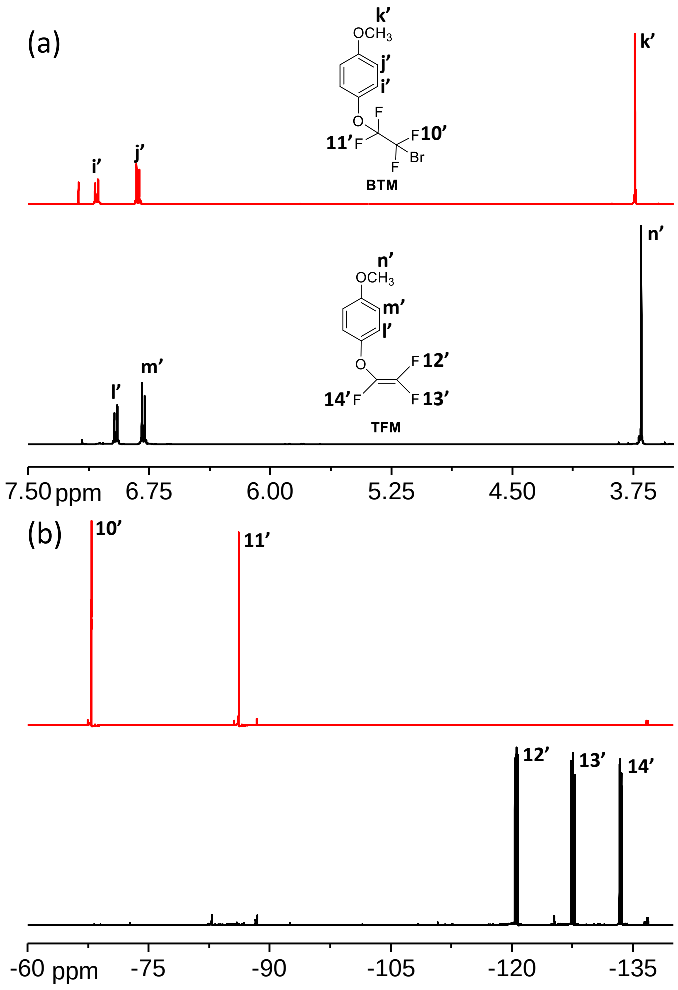

**Figure 2.7.** (a) $^{1}$H NMR and (b) $^{19}$F NMR of hydrophobic end-capper: BTM and TFM

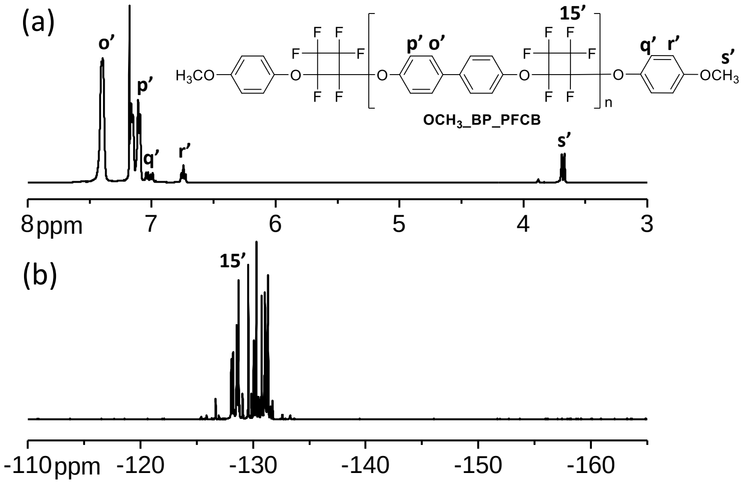

**Figure 2.8.** (a) $^{1}H$ NMR and (b) $^{19}F$ NMR of hydrophobic oligomer: BP_PFCB_OCH3

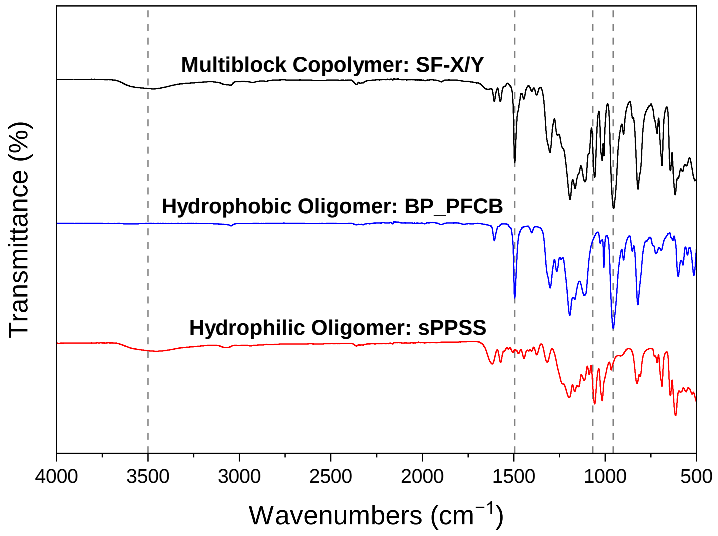

**Figure 2.9.** FTIR spectra of hydrophilic oligomer (sPPSS), hydrophobic oligomer (BP_PFCB), and multiblock copolymer (SF-X/Y)

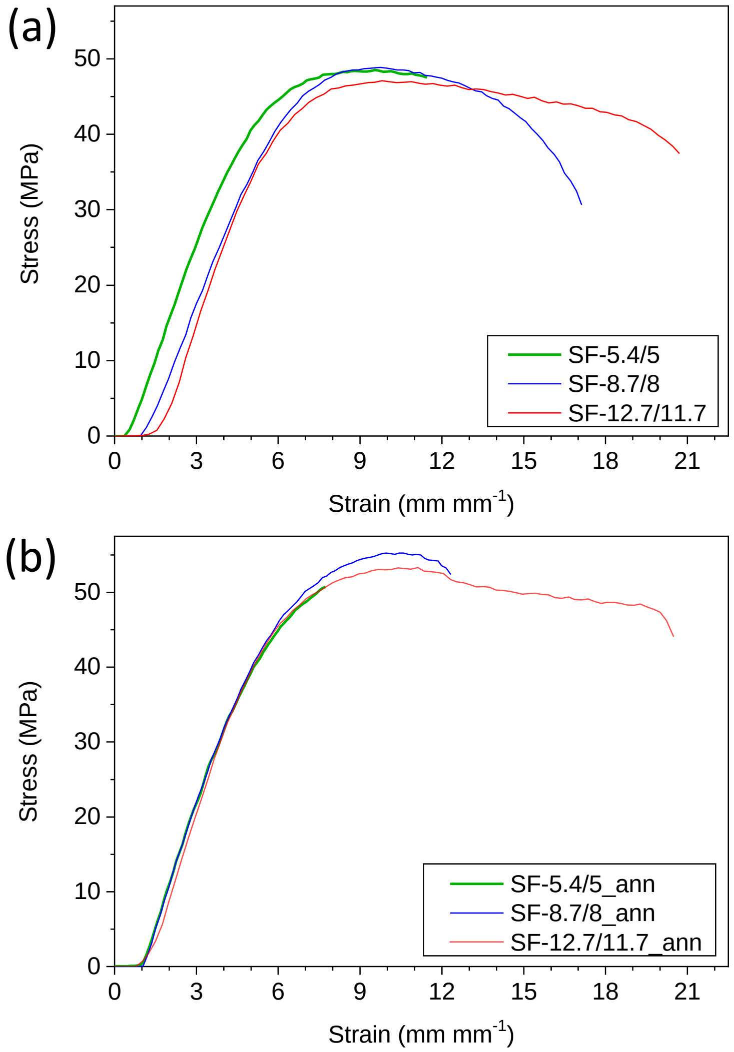

**Figure 2.10.** Stress-strain curves of (a) SF-X/Y and (b) SF-X/Y_ann

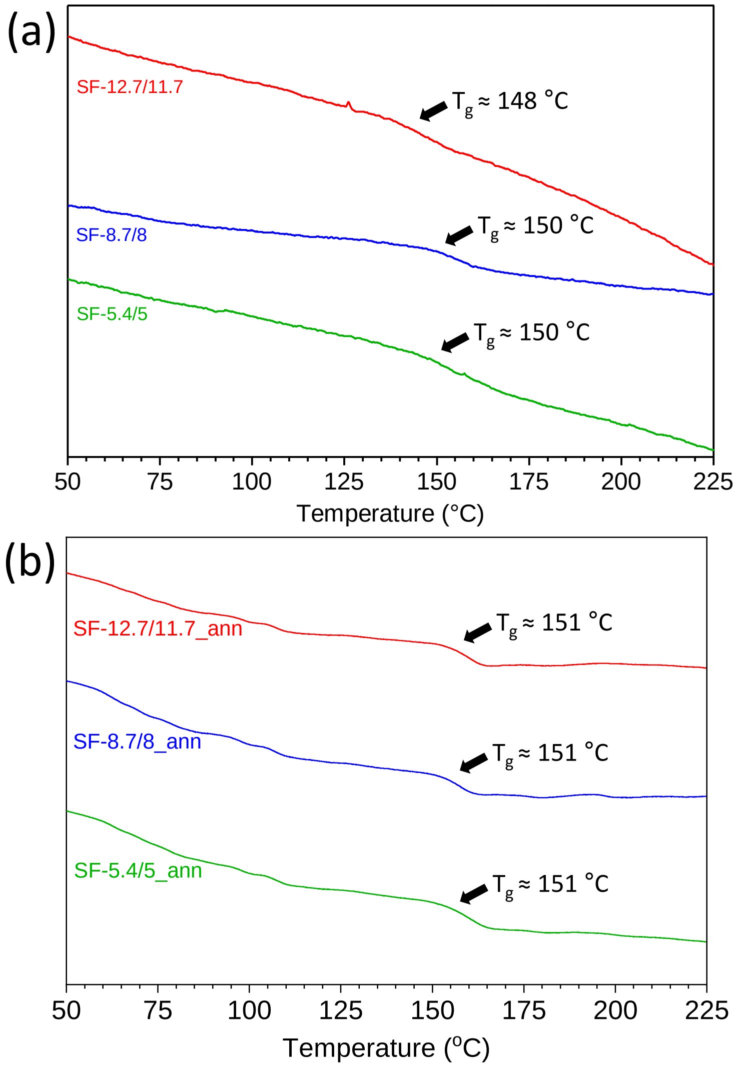

**Figure 2.11.** DSC curves of (a) SF-X/Y and (b) SF-X/Y_ann with $T_g$

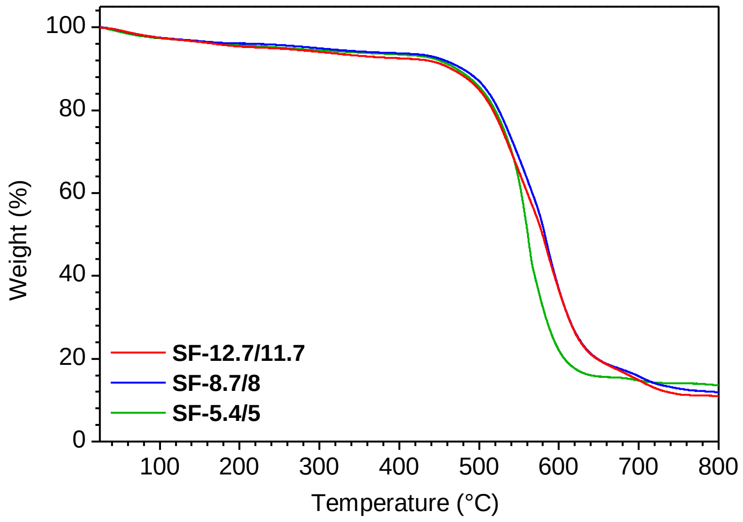

**Figure 2.12.** TGA curves of SF-X/Y polymer

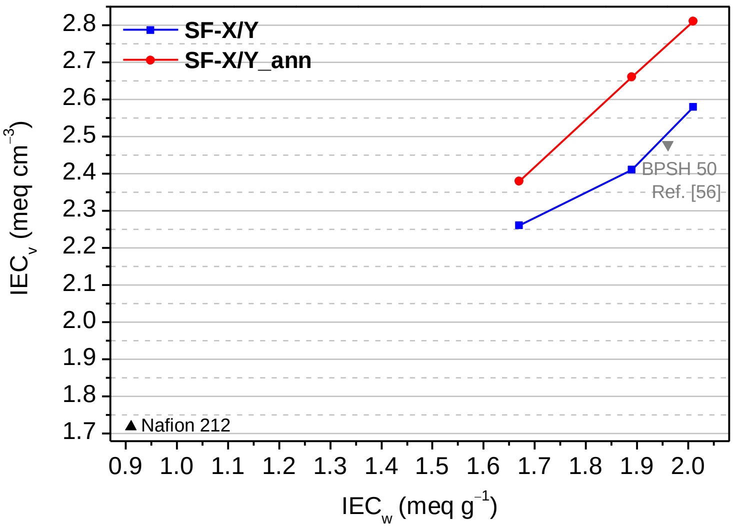

**Figure 2.13.** Volumetric IEC (IEC$_v$), representing the concentration of sulfonic acid group per unit volume, as a function of gravimetric IEC (IEC$_w$)

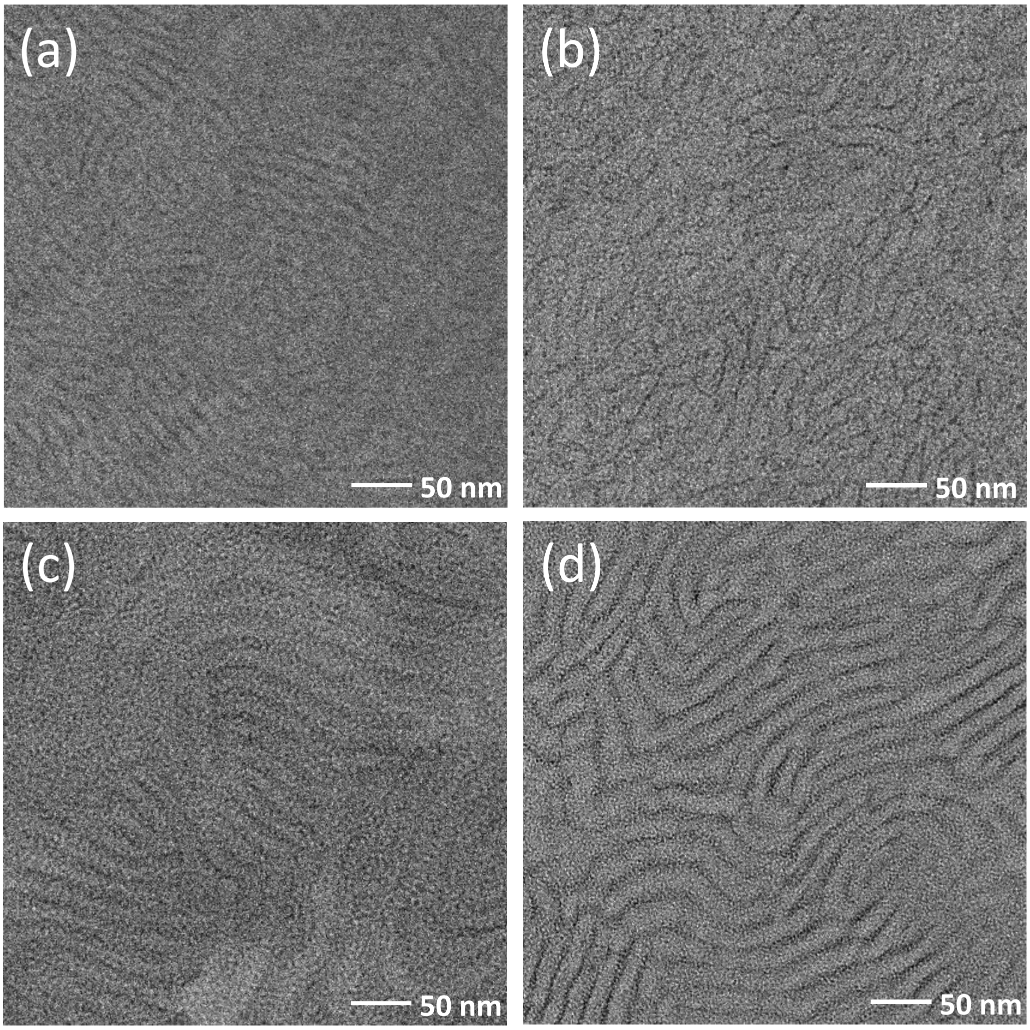

**Figure 2.14.** TEM images of (a) SF-5.4/5, (b) SF-5.4/5_ann, (c) SF-12.7/11.7, and (d) SF-12.7/11.7_ann in the scale of 50 nm

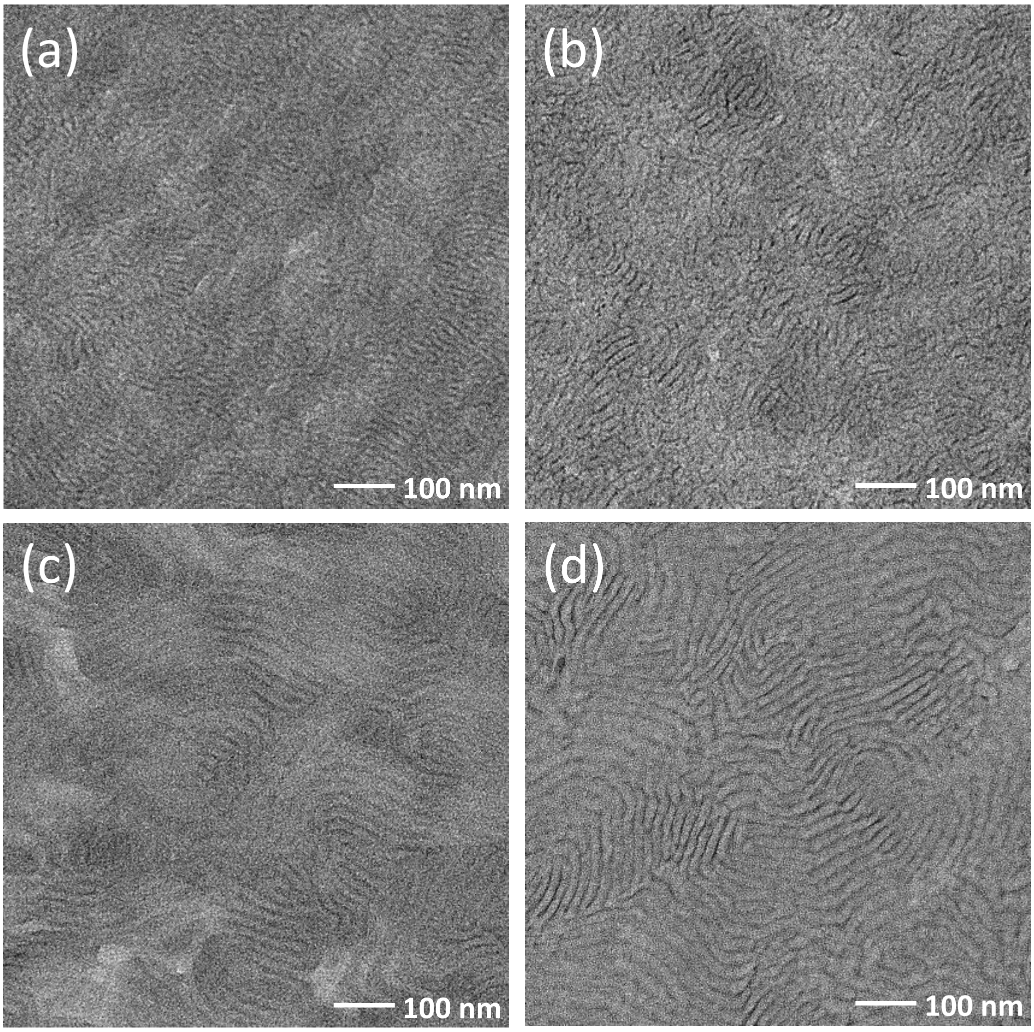

**Figure 2.15.** TEM images of (a) SF-5.4/5, (b) SF-5.4/5_ann, (c) SF-12.7/11.7, and (d) SF-12.7/11.7_ann in the scale of 100 nm

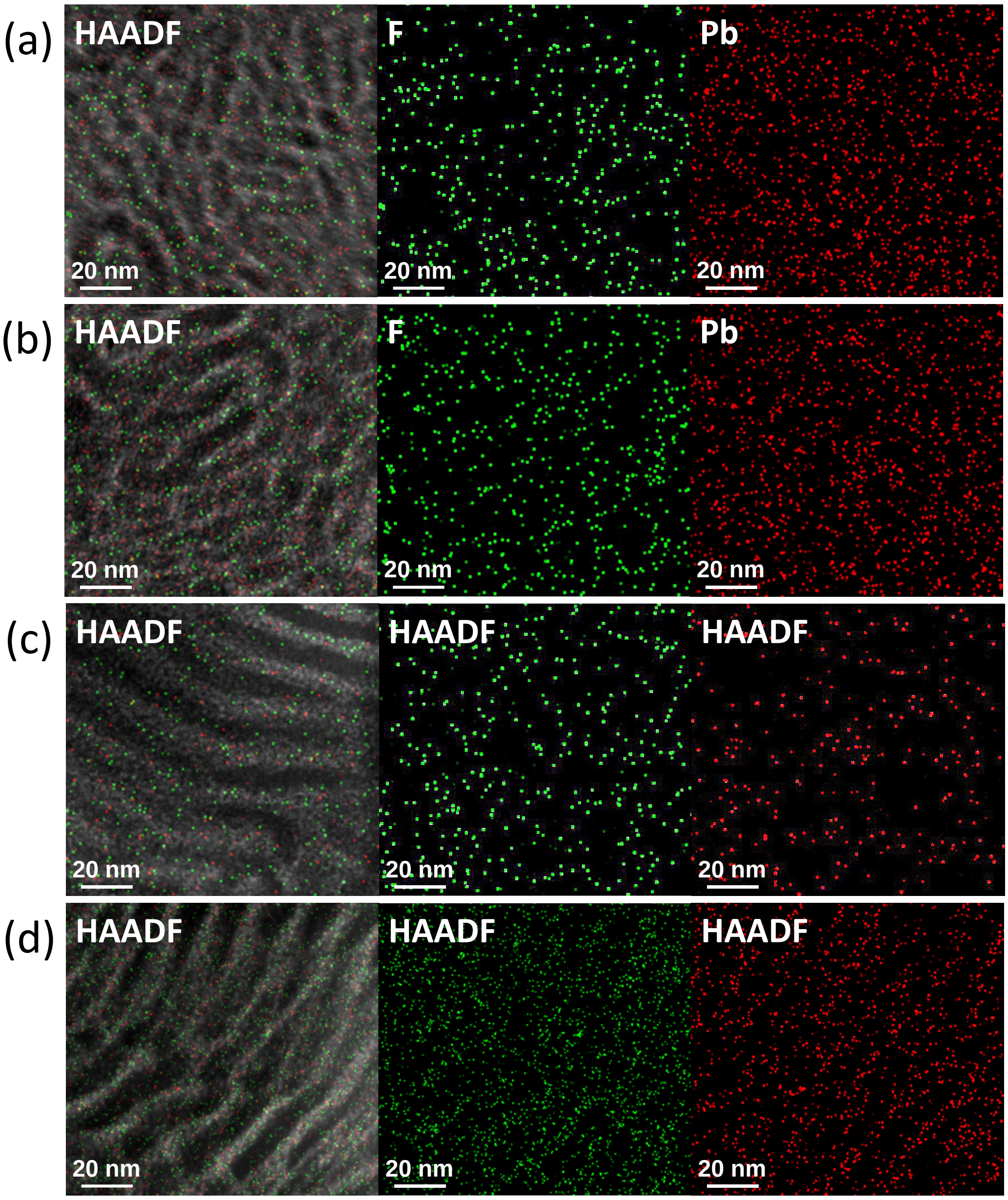

**Figure 2.16.** HAADF and EDS mapping (F and Pb) images of (a) SF-5.4/5, (b) SF-5.4/5_ann, (c) SF-12.7/11.7, and (d) SF-12.7/11.7_ann in the scale of 20 nm

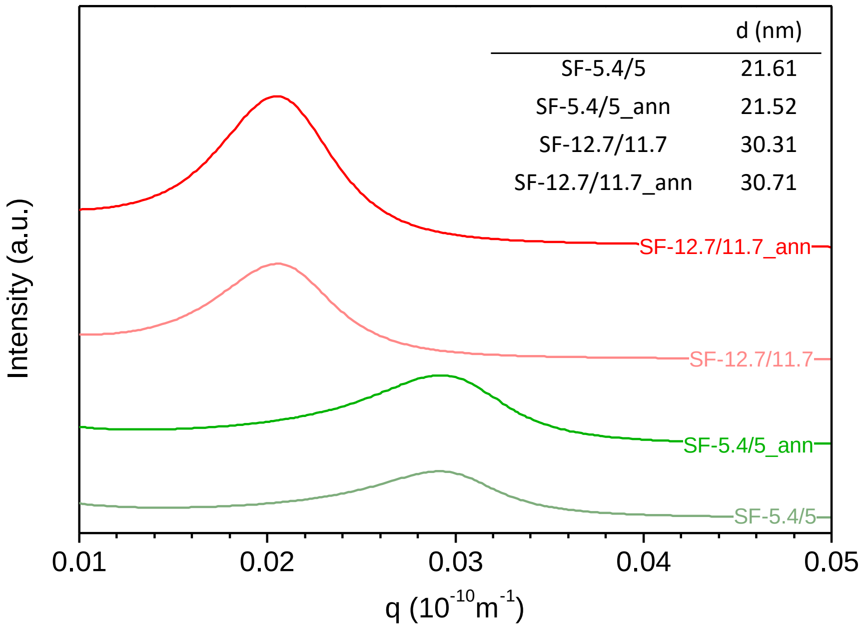

**Figure 2.17.** SAXS analyses of SF-5.4/5, SF-5.4/5_ann, SF-12.7/11.7, and SF-12.7/11.7_ann

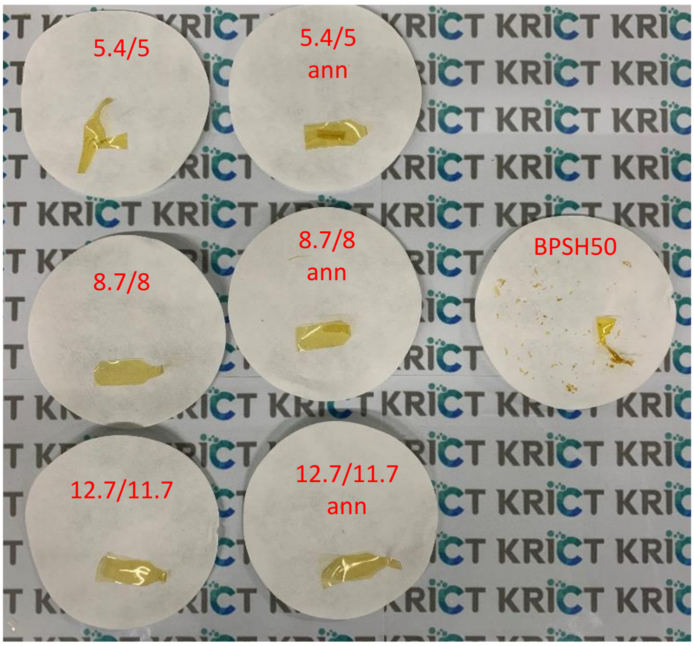

**Figure 2.18.** SF-X/Y, SF-X/Y_ann, and BPSH 50 after Fenton test

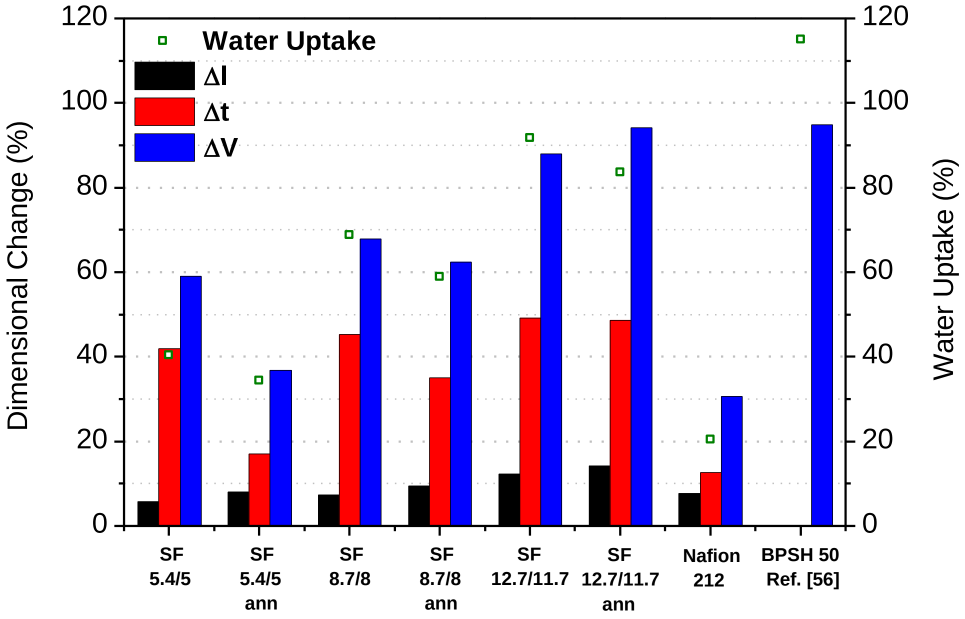

**Figure 2.19.** Water uptake capacities and dimensional changes in SF-X/Y, SF-X/Y_ann, Nafion 212, and BPSH 50 at 25 °C

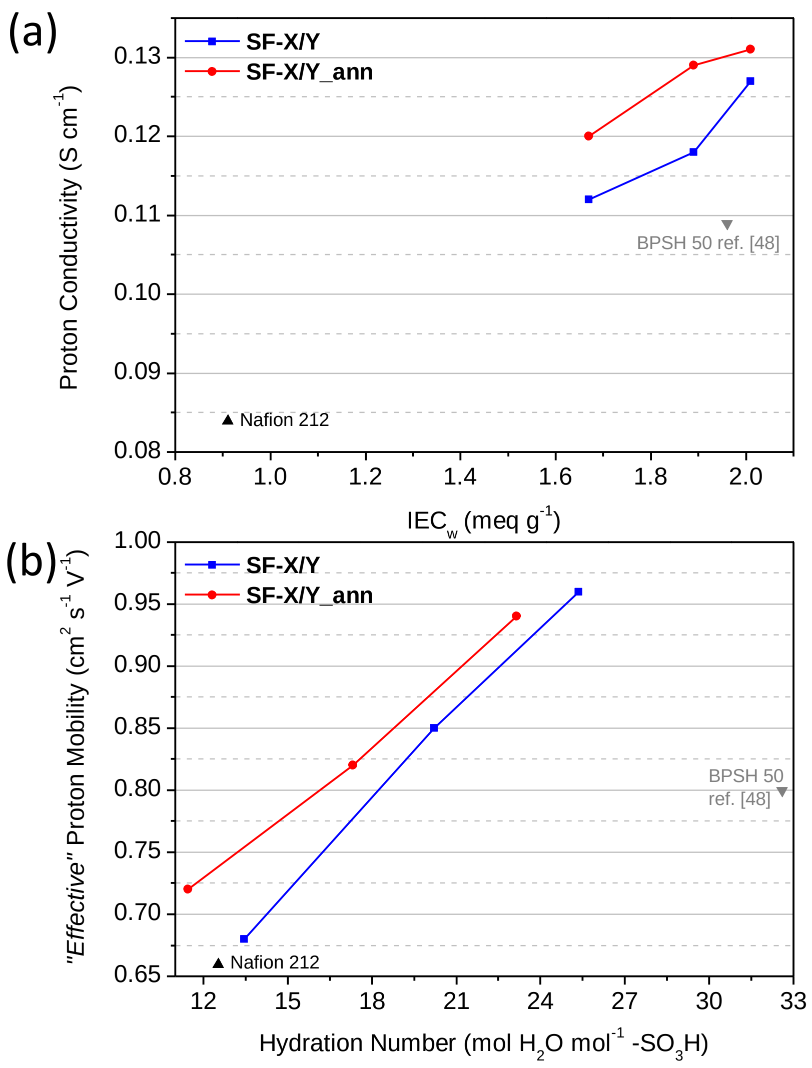

**Figure 2.20.** (a) Proton conductivities as a function of $IEC_w$ and (b) $\mu_{eff}$ values as a function of $\lambda$ for SF-X/Y, SF-X/Y_ann, Nafion 212, and BPSH 50 at 25 °C and RH of 100%

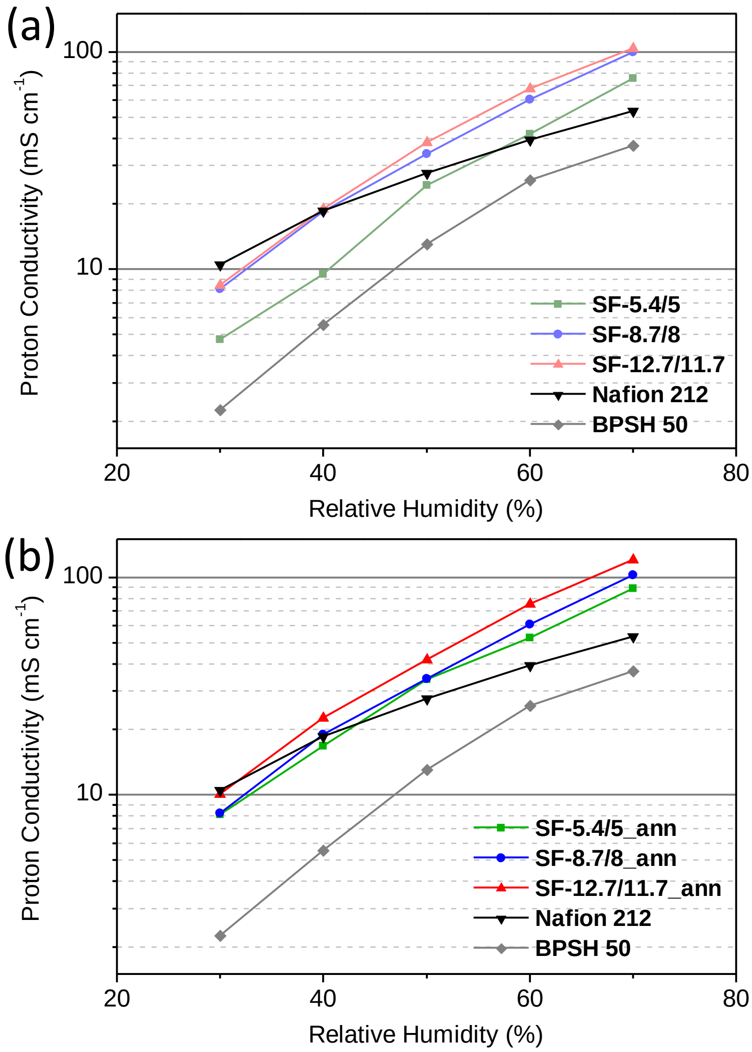

**Figure 2.21.** Proton conductivities of (a) SF-X/Y and (b) SF-X/Y_ann at 80 °C and low humidifications

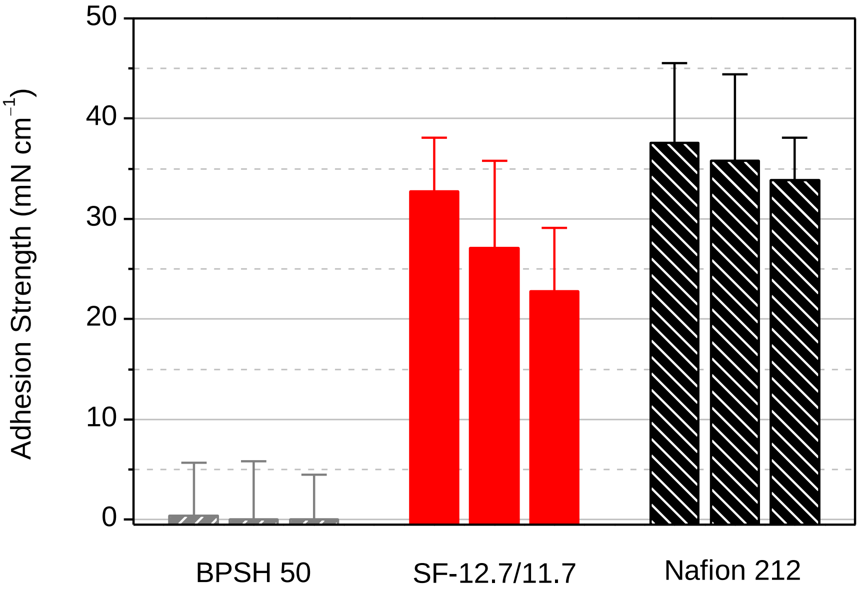

**Figure 2.22.** Interfacial bond strengths of BPSH 50, SF-12.7/11.7, and Nafion 212 against hot-pressed Nafion 212, as measured by the T-peel test

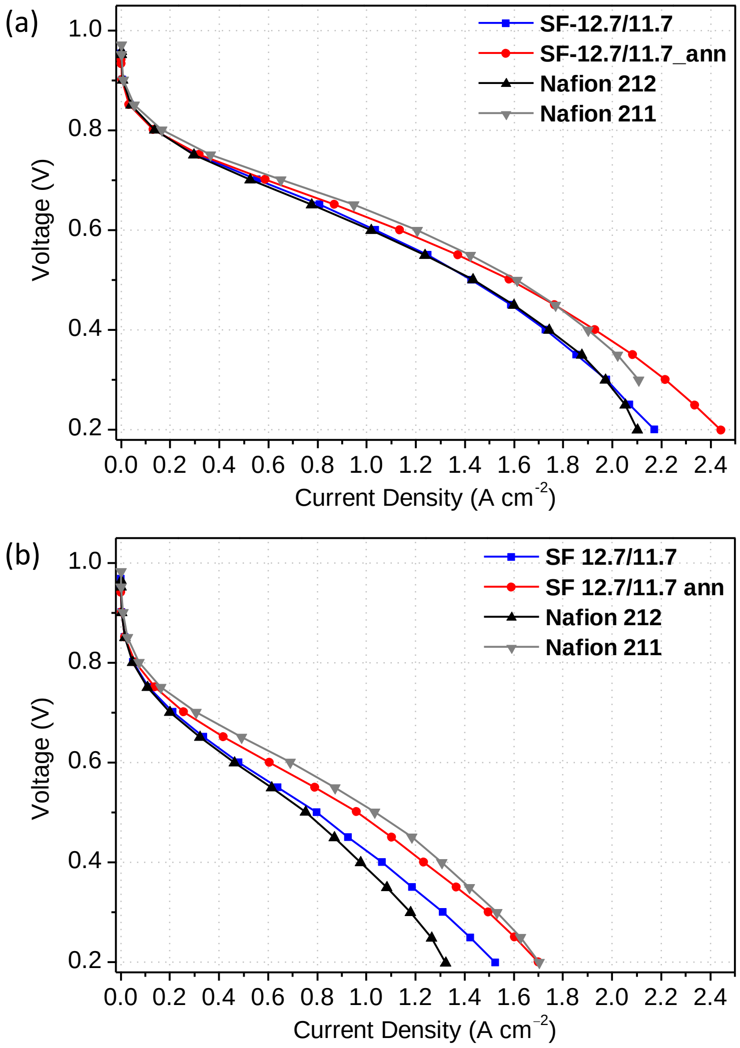

**Figure 2.23.** Polarization curves of MEAs containing SF-12.7/11.7 (0.33 mgPtcm$^{-2}$ CCM), SF-12.7/11.7_ann (0.34 mgPtcm$^{-2}$ CCM), Nafion 212 (0.34 mgPtcm$^{-2}$ CCM), and Nafion 211 (0.31 mgPtcm$^{-2}$ CCM) at 65 °C and RH of (a) 100% and (b) 50% Note: active area = 25 cm$^2$, 1.5/2.0 ($H_2$/Air)

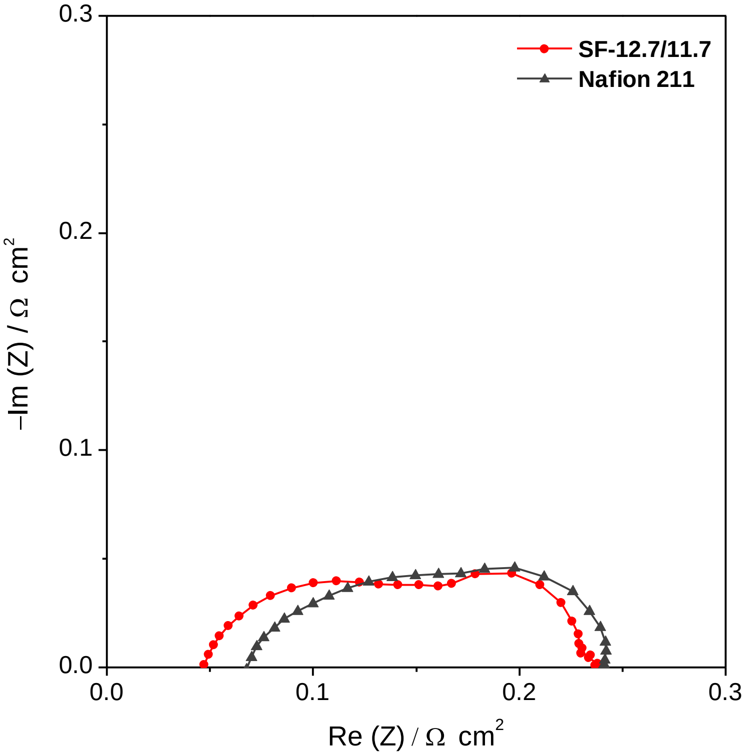

**Figure 2.24.** Nyquist plots of MEAs with SF-12.17/11.7 (0.33 mgPtcm$^{-2}$ CCM) and Nafion 211 (0.34 mgPtcm$^{-2}$ CCM) at 65 °C, RH of 100% Note: active area 25 cm$^2$, 1.5/2.0 ($H_2$/Air)

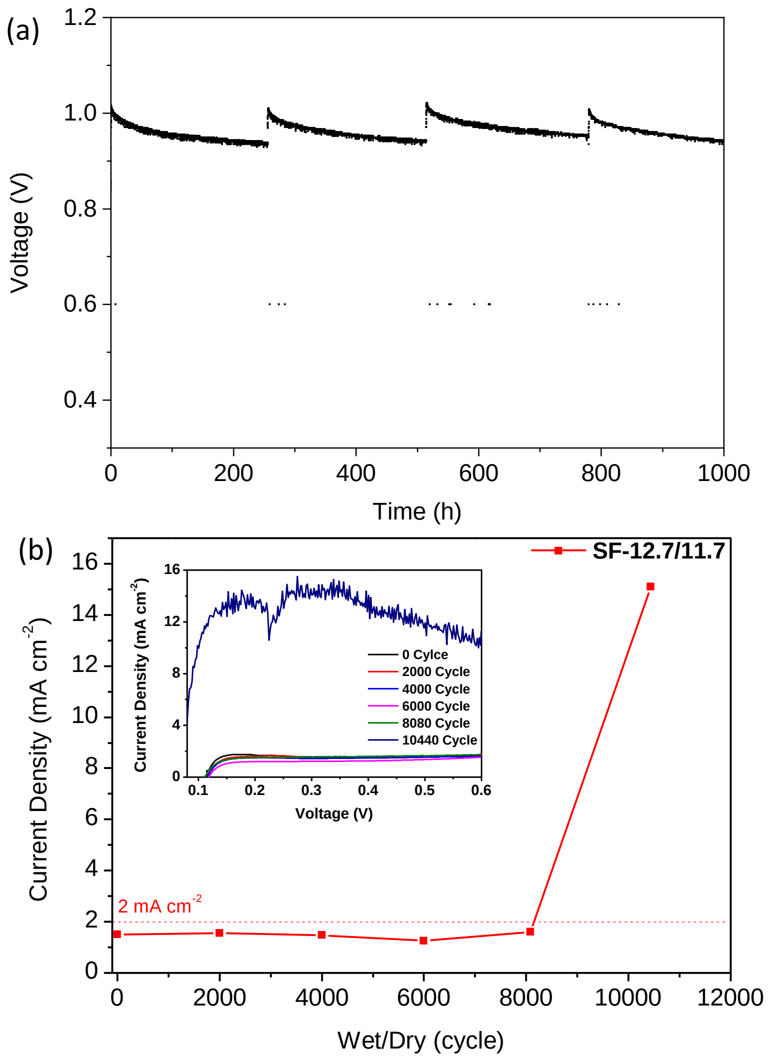

**Figure 2.25.** (a) OCV hold test for SF-12.7/11.7 MEA. (b) Evolution of the hydrogen crossover current density of SF-12.7/11.7 MEA during humidity-conditioned (wet/dry) cycling test and LSV measurements for designated cycles

# Chapter 3

# Design of highly sulfonated aromatic graft polymer with very high proton conductivity and low hydrogen permeability for water electrolysis

## 3.1. Introduction

Proton exchange membrane water electrolysis (PEMWE) produces green hydrogen from renewable energy, which is stored, redistributed, and converted back to electrical energy [1]. PEMWE is a promising technology for future sustainable hydrogen production owing to its inherently high power and compactness, high operational capability under differential pressure, production of pure hydrogen, and fast response to load changes [2]. However, under fluctuating conditions when directly coupled to renewable energy, especially under a low load operation, the hydrogen in oxygen can exceed the safety limit of 2% and develop into explosive anodic mixtures, leading to serious safety and durability issues [3]

Proton exchange membrane (PEM), the key material in PEMWE, requires high proton conductivity (σ) and low gas permeability to promote proton transport and prevent gas mixing [4]. PEMWE operation demands durable-dimensional and thermo-hydrolytic stabilities of PEM [5]. Gas permeability is determined by the diffusion coefficient, solubility, structure, glass transition temperature ($T_g$), and crystallinity of the polymer [6]. Permeability is also affected by the liquid water being subjected to PEMWE, which functions as a plasticizer, lowering $T_g$ and increasing PEM permeability [7]. The amphiphilic nature of PEM induces a hydrophilic/hydrophobic phase separation, where the proton is transported through hydrophilic channels [8]. Although hydrogen permeation occurs in both the hydrophilic and hydrophobic domains of PEM, hydrogen permeates through the water-bearing hydrophilic domains with lower activation energy [9, 10]. Therefore, designing the PEM morphology by promoting high σ, while maintaining low hydrogen permeability ($P_{H2}$) is the key to achieving a PEMWE with efficient performance, durability, and safety.

Commercial Nafion exhibits excellent σ and dimensional stability, but high $P_{H2}$ derived from high diffusion coefficient and low $T_g$ remains an issue [11, 12]. Aromatic hydrocarbon-PEM has emerged as an attractive option for reducing $P_{H2}$, owing to its superior hydrogen barrier properties [13]. Thus far, few studies have focused on the structural design of PEM, considering $P_{H2}$, σ, dimensional stability, and mechanical strength [14-17]. Recently, Han et al. reported a random copolymer with low $P_{H2}$, but a large dimensional change was observed in heated water where sufficient σ was acquired [16]. A multiblock copolymer with larger hydrophilic domains showed high σ and dimensional stability, but $P_{H2}$ was inferior to the random analog [16].

Herein, we present a fully aromatic comb-shaped graft PEM (G-sPSS-X, X = ion exchange capacity, IEC) applied to PEMWE. Despite its potential for effective morphology in PEMWE, application of fully aromatic graft PEM was reported none for PEMWE and only few for PEMFC due to limited structural design and unwanted crosslinking reaction. The G-sPSS-X was compared with the hydrocarbon-PEM (MB-sPSS-X) designed as multiblock architecture and the commercial perfluorosulfonated (PFSA)-PEM (N212). The graft architecture resembled Nafion, wherein a highly sulfonated side chain was grafted to the hydrophobic main chain, inducing unique and distinct nanophase separation interconnected with hydrophilic domains of restricted size (Figure 3.1). This morphology proved effective for PEMWE, resulting in a very high σ (0.291 S $cm^{-1}$, 90 °C), which is 1.51-times that of N212, and low $P_{H2}$ (27.84 barrer, 80 °C), which is 3.23-times less than that of N212. The spider chart shown in Figure 3.2 and Table 3.1 illustrates the balanced property of G-sPSS-1.95, displaying superior mechanical, dimensional, and thermo-hydrolytic stability, resulting in a PEMWE performance of 5,329 mA $cm^{-2}$ at 1.9 V; this is 1.88-times higher than that of N212 (Figure 3.3).

## 3.2. Experimental

### Materials

Sodium hydrosulfide hydrate, potassium carbonate, calcium carbonate, 2-naphthalenethiol, decafluorobiphenyl, 2-methoxyhydroquinone, lithium sulfide, anhydrous dimethyl sulfoxide (DMSO), anhydrous 1-methyl-2-pyrrolidinone (NMP), anhydrous N,N-dimethylacetamide (DMAc), anhydrous toluene, anhydrous chloroform, fuming sulfuric acid (30% free SO3 basis), boron tribromide solution (1.0 M in methylene chloride), and isopropanol (IPA) were purchased from Sigma-Aldrich. 4,4'-Dihydroxydiphenyl ether (DHDPE) was purchased from TCI Chemicals. Hydrochloric acid (30%) was purchased from OCI Company Ltd. Sodium chloride (99%), sodium hydroxide (>98%), 2-propanol, methyl alcohol, and dimethyl sulfoxide were purchased from Samchun Chemicals. All of the chemical reagents above were used without further purification. 4,4'-Difluorodiphenyl sulfone (DFDPS) and 4,4'-dichlorodiphenyl sulfone (DCDPS) were purchased from Career Henan Chemical Co. and Solvay, respectively, and were recrystallized before use. Nafion 212 (N212) membrane and Nafion ionomer were purchased from Dupont. $IrO_2$ and Pt/C (40%) catalyst was purchased from Alfa Aesar Co. and Johnson Matthey Co., respectively. Titatium paper, single-cell, and PEMWE station were purchased from CNL Co.. Carbon paper (JNTGA3-30) was purchased from JNTG Co.

## Synthesis of side-chain monomer, 4-chloro-4'-mercaptodiphenyl sulfone (CMDPS)

To avoid crosslinking in graft reaction, the side-chain was synthesized from an AB-type monomer, 4-chloro-4'mercaptodiphenyl sulfone (CMDPS), as shown in Figure 3.4. CMDPS was synthesized by adding DCDPS (100 g, 0.32 mol) and anhydrous DMSO (42% solid content) to 300-mL round bottom flask (RBF) with argon gas inlet, and increasing the temperature to 60 °C until the solution fully dissolved for 1 h. Then, sodium hydrosulfide hydrate (25.14 g, 0.32 mol), potassium carbonate (21.88 g, 0.16 mol), and anhydrous DMSO were added to the solution, changing the solution from transparent to green. The solution was heated to 80 °C and maintained for 4 h, in which the solution turned to orange. The reacted solution was precipitated in 5wt% cold KOH solution. After extraction with ethyl acetate, the solution was titrated to pH 7 with hydrochloric acid until white precipitates were formed. The white precipitates were washed with deionized water and filtered. The filtered solid was dried in a vacuum oven at 80 °C overnight.

## Synthesis of side-chain, sulfonated poly(phenylene sulfide sulfone)

The side-chain of the graft polymer was synthesized from AB-type monomer, CMDPS. To prepare a side-chain with a molecular weight of 9000 g $mol^{-1}$, CMDPS (27.34 g, 0.096 mol), 4-*tert*-Butylbenzenethiol (BBT) (0.91 g, 0.0055 mol), potassium carbonate (8.41 g, 0.061 mol), and anhydrous NMP (137.91 mL, 17% solid content) were added in a 250-mL RBF charged with argon. The solution reacted for 3 h at 130 °C, and was cooled to room temperature. The target molecular weight was achieved by controlling the molar feed ratios of CMPDS and BBT. To avoid crosslinking in graft reaction, additional feed of end-capper BBT was added to the solution. BBT (0.091 g, 0.00055 mol), potassium carbonate (0.090 g, 0.00065 mol), and anhydrous DMAc (0.88 mL, 17% solid content) were added to schlenk flask charged with argon, and the solution was heated to 130 °C for 2 h. The reacted solution was poured into the CMDPS-containing solution, and the solution was heated to 130 °C for 2 h. Meanwhile decafluorobiphenyl (DFBP) (19.72 g, 0.059 mol) and anhydrous NMP (613.51 mL, 6% solid content) were dissolved in a 300-mL RBF at room temperature. The CMDPS-containing solution was dropped into the DFBP-containing solution at 0 °C using an ice bath to avoid undesirable crosslinking, and was stirred for 2 h charged with argon. The final solution was precipitated in methyl alcohol, and was washed several times with methyl alcohol.

The product was dried *in vacuo* at 80 °C overnight.

Functionalization of sulfonic acid group was achieved with post-sulfonation process. The product obtained from the previous step (24.20 g, 0.0027 mol, 1 equiv.) and fuming sulfuric acid (73.87 g, 5 equiv.) were added to 250-mL jacketed RFB at −10 °C for 5 days. The product was poured in ice water bath, and was precipitated by saturating the aqueous solution with sodium chloride. The filtered product was dissolved in deionized water and was titrated to pH 7 with 10 N sodium hydroxide solution. The dissolved solution was precipitated by saturating with sodium chloride. The filtered solid was dried under vacuum at 60 °C overnight. The vacuum-dried product was then dissolved in DMSO. The solution was then filtered to remove excess sodium chloride, and the filtrate was precipitated and washed in 2-propanol several times. The final product was dried *in vacuo* at 60 °C overnight.

## Synthesis of main-chain, poly(arylene ether sulfone)

The main-chain of graft polymer with pendant methoxy groups (120000 g mol$^{-1}$) were synthesized by adding 2-methoxyhydroquinone (0.60 g, 0.0043 mol), DHDPE (12.51 g, 0.062 mol), DFDPS (16.88 g, 0.066 mol), potassium carbonate (10.86 g, 0.079 mol), anhydrous DMAc (120 mL, 20% solid content), and anhydrous toluene (120 mL) in 250-mL RBF charged with argon by slowly increasing the temperature to 175 °C while azeotropically removing water by refluxing toluene. After fully removing the toluene through dean-stark trap, the solution was reacted for 5 h at 175 °C, and was cooled to room temperature. BBT (0.83 g, 0.0050 mol), potassium carbonate (0.83 g, 0.0060 mol), and anhydrous DMAc (6.64 mL, 20% solid content) were added to schlenk flask charged with argon, and the solution was heated to 130 °C for 2 h. The BBT-containing solution was poured into the DHDPE-containing solution, and the mixture was stirred at 130 °C for 2 h. The product was precipitated in deionized water, and washed with deionized water and 2-propanol several times. The filtered product was vacuum-dried at 80 °C overnight.

The pendant methoxy group of the polymerized main-chain was demethylated to pendant hydroxy group. The methoxy-containing polymer (26.88 g, 0.064 mol) was dissolved in anhydrous chloroform (284.57 mL, 6% solid content) at room temperature charged with argon. After the polymer was completely dissolved, boron tribromide solution (25.09 mL, 0.025 mol, 6 equiv.) was dropped into the solution, and was reacted for 3 hours. The product was precipitated into methyl alcohol, and was thoroughly washed with methyl alcohol. The filtered solid was dried *in vacuo* at 80 °C overnight.

## Synthesis of graft polymer by grafting side-chain to main-chain

Graft polymer was synthesized by nucleophilic substitution reaction between highly reactive DFBP group of side-chain and hydroxy group of main-chain. The main-chain polymer (1.39 g, 0.0034 mol) and anhydrous DMAc (50.75 mL, 2.59 wt%) were dissolved in a 100-mL RBF charged with argon at 80 °C for 2 h. After the solution was fully dissolved, potassium carbonate (0.30 g, 0.0022 mol) was added, and the solution was heated to 110 °C for 1 hour. Meanwhile, the side-chain polymer (6 g, 0.00055 mol, 2.5 equiv. of hydroxy group mol %) was dissolved in anhydrous DMAc (23.30 mL, 20% solid content) at 80 °C until fully dissolved. Both solutions were cooled to room temperature after reaction. The side-chain solution was injected into the main-chain solution at room temperature, and the mixed solution was heated to 80 °C for 48 h. The product was precipitated to 2-propanol, and was washed several times with deionized water and 2-propanol. The filtered product was dried *in vacuo* at 60 °C overnight.

### Synthesis hydrophilic oligomer, sulfonated poly(arylene ether sulfone)

The hydrophilic oligomer of multiblock copolymer with molecular weight of 10000 g $mol^{-1}$ was synthesized by adding DFDPS (25.51 g, 0.10 mol), lithium sulfide (4.49 g, 0.098 mol), and anhydrous NMP (120 mL, 20% solid content) in a

300-mL dehydrated RBF, charged with argon, and the solution was slowly heated to 160 °C, reacting for 18 h (Figure 3.5). The solution was precipitated and washed several times with deionized water. The filtered solid was vacuum-dried at 80 °C overnight.

The hydrophilic oligomer was functionalized with sulfonic acid group through postsulfonation process by adding unsulfonated hydrophilic oligomer (23.18 g, 0.0023 mol, 1 equiv.) with fuming sulfuric acid (74.69 g, 5 equiv.) in a 250-mL jacketed RBF at −10 °C for 5 days. The product was poured in ice water bath, and precipitated by saturating the aqueous solution with sodium chloride. The filtered product was dissolved in deionized water and was titrated to pH 7 with 10 N sodium hydroxide solution. The dissolved solution was precipitated by saturating with sodium chloride. The filtered solid was dried under vacuum at 60 °C overnight. The vacuum-dried product was then dissolved in DMSO. The solution was then filtered to remove excess sodium chloride, and the filtrate was precipitated and washed in 2-propanol several times. The final product was dried *in vacuo* at 80 °C overnight.

## Synthesis hydrophobic oligomer, poly(arylene ether sulfone)

The hydrophobic oligomer of multiblock copolymer with molecular weight of 8000 g $mol^{-1}$ was synthesized by adding DHDPE (12.78 g, 0.063 mol), DCDPS

(17.22 g, 0.060 mol), potassium carbonate (10.48 g, 0.076 mol), anhydrous DMAc (120 mL, 20% solid content), and anhydrous toluene (75 mL) in a 300-mL RBF, charged with argon. The solution was heated to 175 °C, while azeotropically removing water by refluxing toluene. After fully removing the toluene through dean-stark trap, the solution was reacted for 18 h at 175 °C, and was cooled to room temperature. The product was precipitated in deionized water, was washed thoroughly with deionized water and 2-propanol several times, and was vacuum-dried at 80 °C overnight.

## Synthesis of multiblock polymer with hydrophilic oligomer and hydrophobic oligomer

Multiblock polymer was synthesized by nucleophilic substitution reaction between the fluorine group of hydrophilic oligomer and hydroxy group of hydrophobic oligomer. Hydrohpobic oligomer (4.24 g, 0.00048 mol, 1 equiv.), potassium carbonate (0.093 g, 0.00067 mol, 1.4 equiv.), calcium carbonate (0.058 g, 0.00058 mol, 1.2 equiv.), and anhydrous DMAc (52.34 mL, 15% solid content) were dissolved in a 250-mL RBF charged with argon at 160 °C. After the solution was fully dissolved, hydrophilic oligomer (5 g, 0.00048 mol, 1 equiv.) was added, and the solution was heated to 175 °C for 3 d. The solution was precipitated in 1 M hydrochloric acid to remove calcium carbonate. The filtered solid was titrated to pH 8 with potassium carbonate aqueous solution. The filtered product was washed several times with deionized water and 2-propanol, and was dried *in vacuo* at 80 °C overnight.

## Membrane casting

The membranes were prepared by dissolving polymer into anhydrous NMP (18 wt%), and filtering with 5-μm Teflon syringe filters. The solutions were casted with doctor-blade applicator, and dried at 60 °C overnight. The dried membranes were immersed into 1.5 M $H_2SO_4$ aqueous solution at room temperature for 24 h, and subsequently in deionized water at room temperature for 24 h. The thickness of the swollen membranes were adjusted to 50-60 μm.

## Preparation of membrane electrode assembly (MEA) in PEMWE

The MEAs with different membranes (the synthesized membrane and N212) were prepared using the catalyst-coated membrane (CCM) method. The membranes were pre-treated with deionized water at 80 ºC for 1 h. After placing the membranes in a acryl template, they were dried for 12 h. Then, two kinds of catalyst slurry were sprayed to prepare the catalyst layer in the anode and the cathode. The catalyst slurry included anode ($IrO_2$) or cathode (40 wt.% Pt/C) catalyst, deionized water, Nafion ionomer, and IPA. The anode and cathode catalyst loadings were 2.0 and 0.4 mg cm$^{-2}$, respectively. The anode and cathode ionomer contents were 10 and 30 wt.%, respectively.

## Ion exchange capacity (IEC)

Ion exchange capacity (IEC) was measured by adding acid-treated membrane to 100-mL of 0.01 M NaCl aqueous solution. The solution was stirred for 24 h, substituting $H^+$ to $Na^+$. IEC was measured by acid titration method using an autotitrator (Metrohm 794 Basic Titrino), titrating with 0.01 M sodium hydroxide (NaOH) aqueous solution. IEC was calculated by the following equation:

$$IEC\ \ (meq\ \ g^{-1}) = \frac{V \times C}{w},$$

where $V$ is the volume of the aqueous solution of 0.01 M NaOH, titrated to pH 7; $w$ is the weight of the dried sample (g); and $C$ is the molar concentration of the NaOH aqueous solution.

## Inherent viscosity (IV)

To measure the inherent viscosity (IV), polymer was dissolved in NMP (0.5 g $dL^{-1}$) and filtered with a 5-μm syringe filter. IV was measured in a water bath at 25 °C using a Cannon-Ubbelohde viscometer.

## Nuclear magnetic spectroscopy (NMR)

The nuclear magnetic spectroscopy (NMR) samples were prepared by dissolving the synthesized product in deuterated dimethyl sulfoxide (DMSO-d6). The $^1$H and $^{19}$F NMR spectra were obtained on a Bruker Avance NEO (500 MHz) spectrometer.

## Transmission electron microscopy (TEM)

The acid-treated membrane was immersed in an aqueous solution of 0.5 M lead acetate for 24 h to replace the $H^+$ form with the $Pb^{2+}$ form. Lead, which was on the surface of the membrane, was washed with deionized water for 24 h, and the membrane was sufficiently vacuum-dried at 80 °C. The dried membrane was prepared by a Leica EM UC6 ultramicrotome, and the TEM images were obtained on a TECNAI G2 T-20S microscope.

## Small-angle X-ray scattering (SAXS)

SAXS measurements were taken from the Pohang Accelerator Laboratory (PAL) located in Pohang, Republic of Korea using PLS-II 3C beamline. The thickness of the analyzed membranes were fixed at 200 μm for accurate comparison. The data was corrected with background-subtraction. The scattering vector was calculated by the following equation,

$$q = \frac{4\pi}{l(sin2\theta)}$$

where $l$ represents the wavelength of the Cu Kα radiation ($\lambda$=1.541Å) and $2\theta$ represents the scattering angle. The inter-domain space (d) was measured by the following equation,

$$d = \frac{2\pi}{q_{max}}$$

where $q_{max}$ represents the maximum q value ($10^{-10}$ $m^{-1}$).

## Dimensional change and water uptake

Acid-treated membrane was prepared and cut into a size of 2 cm × 2 cm. After immersing the cropped membrane in deionized water for 24 h at 25 °C, its weight, length, and thickness were measured. The weight, length, and thickness of the dried membrane were measured by dehydrating the membrane in a vacuum for 24 h at 50 °C. The dimensional change and water uptake were obtained by the following equations.

$$\Delta Area = \frac{l_{wet} \times l_{wet} - l_{dry} \times l_{dry}}{l_{dry} \times l_{dry}} \times 100(\%)$$

$$\Delta Thickness = \frac{t_{wet} \times t_{wet} - t_{dry} \times t_{dry}}{t_{dry} \times t_{dry}} \times 100(\%)$$

$$Water\ \ Uptake\ \ (\%) = \frac{w_{wet} - w_{dry}}{w_{dry}} \times 100(\%),$$

where $l_{wet}$ and $t_{wet}$ are the length and thickness of the wet membrane, respectively; $l_{dry}$, and $t_{dry}$ represent the length, thickness, and volume of the dry membrane, respectively; $w_{wet}$ and $w_{dry}$ represent the weights of the wet and dry membranes, respectively.

The hydration number (λ) was calculated as the average number of water molecules per sulfonic acid group in the hydrated state.

$$\lambda = \frac{[H_2O]}{[SO_3 -]} = \frac{water\ \ uptake\ \ (\%) \times 10}{18 \times IEC\ \ (meq\ \ g^{-1})}$$

The acid concentration [−SO3H] was calculated by multiplying weight of the dry membrane divided by the volume of the wet membrane with IEC.

$$[-SO_3H] = \frac{w_{dry}(g)}{Volume_{wet}(cm^3)} \times IEC\ \ (meq\ \ g^{-1}).$$

## Proton conductivity

To measure the proton conductivity (σ) in the wet state, AC impedance spectroscopy (ACIS) was performed by the 4-probe method at 25-90 °C and relative humidity (RH) of 100% utilizing a Solatron-1280 impedance/gain-phase analyzer (Solatron), and the frequency was measured with conversion in the range of 0.1–10,000 Hz. The value of the calculated impedance was converted to the proton-conductivity value through the following equation:

$$Proton\ \ Conductivity\ \ (S\ \ cm^{-1}) = \sigma = \frac{1}{R} \times \frac{L}{A},$$

where $R$ is the measured impedance value (Ω), $L$ is the distance between the measured electrodes, and $A$ is the cross-sectional area ($cm^2$) of the ion-exchange membrane that was utilized for the measurement.

The *“effective”* proton mobility ($\mu_{eff}$) is the normalized proton conductivity value after the removal of the effect of the acid concentration. It can be calculated by the following equation:

$$\mu_{eff} = \frac{\sigma}{F \times [-SO_3H]}$$

where $F$ is Faraday’s constant and $\sigma$ ($S\ cm^{-1}$) is the proton conductivity at 25-90 °C and 100% RH.

## Hydrogen permeability

To measure hydrogen gas permeability ($P_{H2}$), a system was developed connecting fuel cell station (SFC-TS, Fuel cell technologies Inc.) to gas chromatography (GC, YL6500 GC, Young In) equipped with a thermal conductivity detector. Between EPDM gaskets (210 μm) and flow field plates, a membrane (t = thickness) was placed without catalyst layers and gas diffusion layers. The humidified (100% RH) $H_2$ and Ar were each fed into anode and cathode side of a cell. The Ar, which was permeated through membrane, was passed to the GC quantifying the concentration of the permeated $H_2$ ($C_H$) in Ar. $P_{H2}$ was evaluated using the following equation,

$$P_{H2} = \frac{C_H \times v \times t}{A \times \Delta p}$$

where v is the Ar flow rate at STP (2750 mL $\text{min}^{-1}$), A is the active area (7.5 $\text{cm}^2$), and $\Delta p$ is the difference of $H_2$ partial pressure across the membrane. The unit for P is (molm $\text{m}^{-2}\text{s}^{-1}\text{Pa}^{-1}$) (1 molm $\text{m}^{-2}\text{s}^{-1}\text{Pa}^{-1} = 2.987 \times 10^{15}$ barrer).

## Gel permeation chromatography (GPC)

Gel permeation chromatography (YL9120 UV/Vis Detector) with YL9112 Isocratic pump and Shodex KF-805L column was used to determine number-average molecular weight (Mn). The flow rate of the eluent (HPLC grade DMAc with 0.05 M LiBr) was 1.0 mLmin$^{-1}$. Calibration was conducted using polystyrene standards.

## Open circuit voltage (OCV) test

The MEA for OCV test was fabricated via catalyst coated gas diffusion layer (GDL) method, loading 0.4 mg$_{Pt}$ cm$^{-2}$ at anode and cathode. To test the chemical stability and degradation of the membrane, the cell was continuously fed with fuels of 300 mL min$^{-1}$ hydrogen and 600 mL min$^{-1}$ air at 90 °C, 25% RH, and 50 kPa back pressure. The back pressure was applied to fill the inside of the cell with gas pressure to allow easy exhaust of water and to increase the gas density. Cell performance test was conducted every 100 hours (approximated) at 80 °C, 100% RH, and 0 kPa back pressure. The polarization curves were measured with fuel cell test station (Z010-100, SCITHEC KOREA).

Electrochemical Impedance spectroscopy (EIS) after OCV test was measured at current density of 1 A cm$^{-2}$ and frequency range from 1 MHz to 10 mHz, adjusting the amplitude of 1 A. The impedance measurements were performed using a potentiostat (HCP-803, Biologic). Hydrogen crossover of MEA was measured every 100 h using linear sweep voltammetry (LSV) from 0.1 to 0.6 V at a scan rate of 2 mV $s^{-1}$. Before measurement, cells were equilibrated at 80 °C in 500SCCM $H_2$/ 500SCCM $N_2$ at 100% RH.

## PEMWE performance

The PEMWE performance and durability were examined based on the single-cell. The single-cell consists of the MEA, porous-transport layer (PTL), and bipolar plates (BPP). The titanium and graphite-based plates were used in the anode and cathode BPP, respectively. The titanium and carbon paper were employed in the anode and cathode PTL. The cell temperature was maintained at 90 ºC. The preheated deionized water at 60 ºC was supplied into the anode as the reactants. The performance was measured using the voltage sweep method from 1.25 to 2.05 V. The voltage scan rate was 10 mV $s^{-1}$. The resistances were evaluated using electrochemical impedance spectroscopy (EIS) operated under a constant voltage of 1.6 V with an amplitude of 50 mV. The durability was conducted using chronopotentiometry at a constant current density of 1000 mA $cm^{-2}$ for 50 h.

# 3.3. Results and discussion

## Syntheses of PEMs

G-sPSS-X was synthesized *via* a polymer analogous reaction, where one end of the side chain was exclusively reactive, suppressing the crosslinking side reaction. G-sPSS-X was designed with a highly sulfonated ether-free hydrophilic side chain to increase rigidity, acidity, and chemical stability. Mechanical balance and thermo-hydrolytic stability were achieved by grafting a hydrophobic main chain containing flexible ether groups. The synthesis of polymers were confirmed in $^{1}$H NMR and $^{19}$F NMR in Figures 3.6, 3.7, and 3.8.The high molecular weight of G-sPSS-X with a side-chain molecular weight of 11,000 g mol$^{-1}$ provided excellent viscosity (1.50–1.66 dL g$^{-1}$). For comparison, MB-sPSS-X with an identical hydrophilic/hydrophobic chemical structure and a hydrophilic block of similar molecular weight (10,000 g mol$^{-1}$) was synthesized (Figure 3.9 and Table 3.2).

## Morphological properties

Hydrophilic/hydrophobic nanophase separation was observed using a transmission electron microscope (TEM) (Figure 3.10). N212 showed phase separation of small-sized domains, whereas G-sPSS-X showed narrow and zebra-shaped nanophase separation with excellent connectivity. Even with the increase in IEC, the domain size did not increase excessively, and the distance between the hydrophilic domains remained narrow. In contrast, MB-sPSS-1.91, which has a similar IEC, exhibited a larger domain size. In small-angle X-ray scattering (SAXS) (Figure 3.11), the d-spacings of hydrophilic domains were investigated using Bragg's law and $q_{max}$ values [18]. G-sPSS-1.95 (11.27 nm) showed narrower d-spacings and sharper peaks than MB-sPSS-1.91 (15.76 nm), suggesting that the sulfonic acid group introduced in the G-sPSS-X side chain formed narrower and denser hydrophilic domains. In other studies, graft PEMs showed a similar trend owing to the unique graft morphology (Table 3.3) [19-21].

## Intrinsic properties of PEMs

Figure 3.12 shows water uptake (WU) and dimensional stability of PEMs at 90 °C. To transport protons, the PEM should maintain sufficient WU level [22]. However, at high temperatures, the WU level should be controlled to prevent excessive swelling. The area of swelling must be minimized to avoid adverse effects on interface stability with the electrode layer in the membrane-electrode assembly (MEA) [23]. N212 showed 34% WU and 28% area change (ΔA), while G-sPSS-

1.47 showed 58% WU and 23% ΔA despite a higher IEC. The WU of G-sPSS-1.95 increased to 125%, but the ΔA was maintained at 40%. G-sPSS-X showed strong anisotropic properties, where swelling was accentuated in the thickness rather than the area. TEM and SAXS analyses confirmed that G-SPSS-1.95 displayed significantly lower WU and ΔA than MB-sPSS-1.91 (150% and 47%, respectively) owing to narrow and dense hydrophilic domains.

The σ was measured over the temperature range of 25–90 °C, i.e. from room temperature to the practical operating temperature of PEMWE Figure 3.13a. PEMs demonstrated a similar tendency, where σ was inversely linearly proportional to 1/T in the Arrhenius plot. N212 showed a σ of 0.083–0.193 S $cm^{-1}$ at 25–90 °C, while in the same temperature range, G-sPSS-1.47 showed a σ of 0.099–0.208 S $cm^{-1}$, i.e. an improvement of 7.77–19.28%. Compared to the hydrocarbon-PEM reference with a similar IEC, G-sPSS-1.47 showed superior σ [16]. G-sPSS-1.95 and MB-sPSS-1.91 exhibited σ values in the ranges of 0.166–0.291 and 0.133–0.229 S $cm^{-1}$, respectively. Since the chemical structures of G-sPSS-1.95 and MB-sPSS-1.91 are identical and the IECs are similar, the higher σ of G-sPSS-1.95 suggests that the graft architecture is more advantageous for proton conduction than the multiblock architecture. Activation energy ($E_a$), which indicates the activation barrier for proton conduction, was calculated from the Arrhenius plot. $E_a$ of G-sPSS-1.47 (10.68 kJ $mol^{-1}$) was lower than that of N212 (11.91 kJ $mol^{-1}$), suggesting that the interconnected morphology of G-sPSS-X is more favorable for proton conduction. $E_a$ of G-sPSS-1.95 (7.93 kJ $mol^{-1}$) was lower than that of MB-sPSS-1.91(9.97 kJ $mol^{-1}$) indicating that a lower activation barrier is required for G-sPSS-X.

"Effective" proton mobility ($\mu_{eff}$) was analyzed to further investigate the relationship between PEM morphology and σ (Figure 3.13b). $\mu_{eff}$, the normalized σ where the acid concentration effect has been removed, revealed effects of σ on acid dissociation degree, tortuosity of proton conducting pathway, and spatial proximity of neighboring acid groups [24]. Since G-sPSS-X has a lower hydration number (λ) (14.89–18.15 $mol_{H2O}$ $mol^{-1}{}_{-SO3H}$) than MB-sPSS-1.95 (23.87 $mol_{H2O}$ $mol^{-1}{}_{-SO3H}$), the amount of $H_2O$ in G-sPSS-X is not the reason for higher σ [25]. The $\mu_{eff}$ values of N212, G-sPSS-1.47, and G-sPSS-1.95 were 0.00063, 0.00075, and 0.0011 $cm^2$ $s^{-1}$ $V^{-1}$, respectively. G-sPSS-1.95 showed a higher $\mu_{eff}$ with lower λ than MB-sPSS-1.91 (0.00098 $cm^2$ $s^{-1}$ $V^{-1}$) with a similar IEC. Since the dissociations of acid groups in hydrocarbon-PEMs are similar because of identical chemical structures, the higher $\mu_{eff}$ of G-sPSS-1.95 implies that the morphology of the graft architecture induced better connectivity and closer proximity of sulfonic acid groups [26].

The mechanical properties of the fully wetted PEMs were analyzed by simulating the PEMWE environment (Figure 3.14). N212, G-sPSS-1.47, G-sPSS-1.95, and MB-sPSS-1.91 exhibited tensile strengths of 21.68, 21.16, 19.82, and 15.31 MPa, respectively, and elongations of 246.55, 68.59, 125.65, and 71.48%, respectively, obtaining mechanical balance from the flexible ether groups in the hydrophobic main chain. The large elongation alleviated physical fatigue caused by the swelling in PEMWE [27].

Humidified hydrogen gas was supplied to one side and the hydrogen that permeated to the other side was measured using gas chromatography to measure $P_{H2}$ of PEMs (Figure 3.15). N212 showed a high $P_{H2}$ of 89.81 barrer at 80 °C, which was approximately three times higher than that of G-sPSS-X (Figure 3.16a). G-sPSS-1.47 displayed 24.46 barrer at 80 °C, and even with increased IEC, G-sPSS-1.95 maintained a low $P_{H2}$ of 27.84 barrer. MB-sPSS-1.91, with a similar IEC, showed a 1.19-fold higher $P_{H2}$, which was attributed to the formation of a wider hydrophilic domain.

To compare the key PEMWE parameters, the figure of merit (FOM) was calculated by dividing σ by $P_{H2}$ (Figure 3.16b). N212 displayed the lowest FOM, 1.94 mS $cm^{-1}$ $barrer^{-1}$ at 80 °C, due to high $P_{H2}$ and low σ. G-sPSS-1.47 showed a higher σ and lower $P_{H2}$ than N212, thus enhancing the FOM (7.97 mS $cm^{-1}$ $barrer^{-1}$). The highest FOM at 80 °C was obtained for G-sPSS-1.95 at 10.20 mS $cm^{-1}$ $barrer^{-1}$. Despite identical hydrophilic/hydrophobic block structures, MB-sPSS-1.91 displayed an FOM of 6.81 mS $cm^{-1}$ $barrer^{-1}$, which was lower than that of G-sPSS-1.47. The interconnected narrow hydrophilic channels of the G-sPSS-X may have induced superior gas barrier properties with favorable proton conduction.

## Thermo-hydrolytic stability test (THST)

Major issues arise in PEMWE due to the use of high-temperature water, such as decrease in dimensional stability caused by membrane swelling and chemical degradation caused by hydrolysis and radical attack [28]. Thermo-hydrolytic stability test (THST) was conducted to measure the different properties of PEMs after immersion in water at 90 °C for several days, simulating PEMWE operation. The fully saturated PEMs maintained a constant ΔA for five to 25 days when immersed at 90 °C (Figure 3.17). N212 showed a 1.27-fold increase of ΔA (28–36%) over the five days. G-sPSS-1.47 displayed a 1.07-fold increase (23–24%) under the same conditions, the smallest among the measured PEMs. G-sPSS-1.95 exhibited a 1.19-fold increase (40–48%), lower than that of N212. In contrast, MB-sPSS-1.91 showed the largest increase of 1.38-fold (47–65%). G-sPSS-X exhibited dimensional stability in PEMWE, where the PEM was exposed to long-term high-temperature water.

Dimensional properties were related to the morphological changes observed by SAXS (Figure 3.18) and TEM (Figure 3.19). After exposure for five days to water at 90 °C, the peaks shifted to lower q values in the SAXS spectra. The d-spacings of N212 (4.43–6.35 nm) and G-sPSS-1.47 (11.56–12.84 nm) increased after the

THST. The increase in d-spacing of MB-sPSS-1.91 (from 16.11 to 19.69 nm) was greater than that of G-sPSS-1.95 (from 10.94 to 12.77 nm). TEM revealed that the size and distance of hydrophilic domains in MB-sPSS-1.91 increased after immersion in water for five days at 90 °C. In contrast, G-sPSS-X maintained a narrow and small hydrophilic domain.

$P_{H2}$ of N212 increased from 38.58 to 89.81 barrer as temperature was increased from 25 to 80 °C (Figure 3.20), followed by an additional 1.09-fold increase (to 97.7 barrer) post the THST (90 °C, 5 d). The poor hydrogen barrier property of N212 further deteriorates at high temperatures in addition to long-term exposure. Hydrocarbon-PEMs showed low $P_{H2}$ even at high temperatures, and the increase was insignificant after the THST. G-sPSS-1.95 exhibited better hydrogen barrier properties than MB-sPSS-1.91, even after long-term immersion in water at 90 °C. Consequently, G-sPSS-1.47 and G-sPSS-1.95 displayed low $P_{H2}$ values of 26.19 and 30.51 barrer, respectively, indicating that G-sPSS-X was less affected by the THST, which is also reflected by an insignificant change in the TEM images.

G-sPSS-X showed a negligible change in the number-average molecular weight ($M_n$) (1.17–6.73%) (Figure 3.21), while MB-sPSS-1.91 showed a $M_n$ reduction ratio of 45.88% after the THST. The $M_n$ reduction ratio was expected to be small for G-sPSS-X owing to its stable hydrophilic structure and unique architecture. Degradation occurs during THSTs in hydrophilic structures [29, 30]. G-sPSS-X and

MB-sPSS-1.91 incorporate an ether-free sulfonated polyarylene sulfide sulfone structure, and the sulfide linkage has a radical stabilizing effect by oxidizing to sulfoxide and sulfone [31]. In MB-sPSS-X, both hydrophilic and hydrophobic blocks constitute the main chain. When hydrophilic chain cleavage in MB-sPSS-X occurs on rare occasions, a large reduction in molecular weight occurs due to the cleavage of the entire main chain. Because G-sPSS-X is composed of a hydrophobic main chain and hydrophilic side chain, molecular weight reduction of the entire chain can be avoided when hydrophilic chain cleavage occurs.

Chemical degradation of PEM by radical attack in PEMWE is controversial in terms of results and mechanisms. PEM degradation is accelerated by radical formation at insufficient humidification during the operation of the PEM fuel cell. In a fully wetted PEMWE environment, fewer radicals are formed, and reactive radical intermediates are diluted by water [32]. To investigate the long-term chemical stability of PEMs, Pt/C catalyst layers were applied on both surfaces of the PEM, and hydrogen and air were fed to each side of the cell to measure the open-circuit voltage (OCV) (Figure 3.22). OCV of N211 decreased continuously from 1 to 0.82 V over 30 h. The voltage drop rate increased subsequently; however, a complete voltage drop occurred after 48 h. G-sPSS-1.95 showed an initial OCV of 1.001 V, and voltage drop ceased beyond 400 h. Linear sweep voltammetry was conducted to determine the extent of hydrogen crossover (Figure 3.23). G-sPSS-

1.95 showed a low current density (< 0.5 mA $cm^{-2}$) after 400 h of the OCV test, indicating low hydrogen crossover. N211 showed an increased current density after 100 h, suggesting that membrane degradation occurred due to radical attack. The Nyquist plots (Figure 3.24) of G-sPSS-1.95 displayed small changes in resistance after the OCV test. The aromatic hydrocarbon-PEM showing superior radical stability has also been confirmed in other studies [33].

## Electrochemical performances

The electrochemical performances of the PEM-incorporated MEAs were evaluated at 90 °C to demonstrate the feasibility of applying PEMs in practical PEMWE. Figure 3.25a and b presents the polarization curves and Nyquist plots obtained at 1.6 V, respectively. PEMWE performances of G-sPSS-1.47, G-sPSS-1.95, MB-sPSS-1.91, and N212 at 1.6 V were 1,144, 1,603, 1,541, and 977 mA $cm^{-2}$, respectively. The performance increased in the order of N212 < G-sPSS1.47 < MB-sPSS-1.91 < G-sPSS-1.95, which is attributed to the effects of ohmic resistance ($R_{ohm}$) and charge-transfer resistance ($R_{ct}$). The $R_{ohm}$ x-intercept in the Nyquist plot is associated with σ at 90 °C. $R_{ohm}$ gradually decreased from 115 to 61 mΩ $cm^{-2}$ as σ increased from 0.193 to 0.291 S $cm^{-2}$. The performance was affected by $R_{ct}$ and the semicircle diameter in the Nyquist plot. $R_{ct}$ is related to catalyst kinetics [34] and membrane/electrode interface [35]. $R_{ct}$ in G-sPSS-1.47, G-sPSS-1.95, and N212 decreased as σ increased because the catalyst kinetics were affected by σ. MB-sPSS-1.91 $R_{ct}$ was larger than that of G-sPSS-1.47, which exhibited a lower σ owing to the large in-plane swelling and ΔA of MB-sPSS-1.91. A large dimensional change deteriorates the membrane/electrode interface, leading to an increased $R_{ct}$.

PEMWE durability tests of G-sPSS-1.95 and N212 were performed at a high current density (1,000 mA $cm^{-2}$) for 50 h (Figure 3.26a). During the first 30 min, both PEMWEs were degraded because of Ti-PTL passivation [36, 37]. After 30 min of operation, G-sPSS-1.95 showed a durable performance without loss for 50 h. Peak change was absent in $^1$H-NMR spectra (Figure 3.26b) for G-sPSS-1.95 before and after the durability test.

## 3.4. Conclusion

In conclusion, we developed a highly sulfonated aromatic G-sPSS-X, which induced formation of interconnected, narrow hydrophilic channels optimized for PEMWE operation, leading to high $\sigma$ and low $P_{H2}$. Along with durable chemical, mechanical, thermo-hydrolytic characteristics, excellent performance and low resistances were demonstrated. Our finding provides a possible outlook on designing PEM and a practical approach of analyzing PEM for PEMWE.

## 3.5. References

[1] A.M. Oliveira, R.R. Beswick, Y. Yan, A green hydrogen economy for a renewable energy society, Current Opinion in Chemical Engineering, 33 (2021) 100701.

[2] C.V. Pham, D. Escalera-López, K. Mayrhofer, S. Cherevko, S. Thiele, Essentials of High Performance Water Electrolyzers – From Catalyst Layer Materials to Electrode Engineering, Advanced Energy Materials, 11 (2021) 2101998.

[3] U. Babic, M. Suermann, F.N. Büchi, L. Gubler, T.J. Schmidt, Critical Review—Identifying Critical Gaps for Polymer Electrolyte Water Electrolysis Development, Journal of The Electrochemical Society, 164 (2017) F387-F399.

[4] H. Nguyen, C. Klose, L. Metzler, S. Vierrath, M. Breitwieser, Fully Hydrocarbon Membrane Electrode Assemblies for Proton Exchange Membrane Fuel Cells and Electrolyzers: An Engineering Perspective, Advanced Energy Materials, 12 (2022) 2103559.

[5] S. Choi, S.-H. Shin, D.-H. Lee, G. Doo, D.W. Lee, J. Hyun, S.H. Yang, D. Man Yu, J.Y. Lee, H.-T. Kim, Oligomeric chain extender-derived poly(p-phenylene)-based multi-block polymer membranes for a wide operating current density range in polymer electrolyte membrane water electrolysis, Journal of Power Sources, 526 (2022) 231146.

[6] K. Ghosal, B.D. Freeman, Gas separation using polymer membranes: an overview, Polymers for Advanced Technologies, 5 (1994) 673-697.

[7] A. Daryaei, G.C. Miller, J. Willey, S. Roy Choudhury, B. Vondrasek, D. Kazerooni, M.R. Burtner, C. Mittelsteadt, J.J. Lesko, J.S. Riffle, J.E. McGrath, Synthesis and Membrane Properties of Sulfonated Poly(arylene ether sulfone) Statistical Copolymers for Electrolysis of Water: Influence of Meta- and Para-Substituted Comonomers, ACS Applied Materials & Interfaces, 9 (2017) 20067-20075.

[8] D.W. Shin, M.D. Guiver, Y.M. Lee, Hydrocarbon-Based Polymer Electrolyte Membranes: Importance of Morphology on Ion Transport and Membrane Stability, Chemical Reviews, 117 (2017) 4759-4805.

[9] M. Schalenbach, T. Hoefner, P. Paciok, M. Carmo, W. Lueke, D. Stolten, Gas Permeation through Nafion. Part 1: Measurements, The Journal of Physical Chemistry C, 119 (2015) 25145-25155.

[10] M. Schalenbach, M.A. Hoeh, J.T. Gostick, W. Lueke, D. Stolten, Gas Permeation through Nafion. Part 2: Resistor Network Model, The Journal of Physical Chemistry C, 119 (2015) 25156-25169.

[11] M. Mukaddam, E. Litwiller, I. Pinnau, Gas Sorption, Diffusion, and Permeation in Nafion, Macromolecules, 49 (2016) 280-286.

[12] H. Ito, T. Maeda, A. Nakano, H. Takenaka, Properties of Nafion membranes

under PEM water electrolysis conditions, International Journal of Hydrogen Energy, 36 (2011) 10527-10540.

[13] B.-H. Goo, A.Z. Al Munsur, O. Choi, Y. Kim, O.J. Kwon, T.-H. Kim, Sulfonated Poly(ether sulfone)-Coated and -Blended Nafion Membranes with Enhanced Conductivity and Reduced Hydrogen Permeability, ACS Applied Energy Materials, 3 (2020) 11418-11433.

[14] C. Klose, T. Saatkamp, A. Münchinger, L. Bohn, G. Titvinidze, M. Breitwieser, K.-D. Kreuer, S. Vierrath, All-Hydrocarbon MEA for PEM Water Electrolysis Combining Low Hydrogen Crossover and High Efficiency, Advanced Energy Materials, 10 (2020) 1903995.

[15] J.E. Park, J. Kim, J. Han, K. Kim, S. Park, S. Kim, H.S. Park, Y.-H. Cho, J.-C. Lee, Y.-E. Sung, High-performance proton-exchange membrane water electrolysis using a sulfonated poly(arylene ether sulfone) membrane and ionomer, Journal of Membrane Science, 620 (2021) 118871.

[16] S.-Y. Han, D.M. Yu, Y.-H. Mo, S.M. Ahn, J.Y. Lee, T.-H. Kim, S.J. Yoon, S. Hong, Y.T. Hong, S. So, Ion exchange capacity controlled biphenol-based sulfonated poly(arylene ether sulfone) for polymer electrolyte membrane water electrolyzers: Comparison of random and multi-block copolymers, Journal of Membrane Science, 634 (2021) 119370.

[17] J.E. Chae, S.Y. Lee, S.Y. Baek, K.H. Song, C.H. Park, H.-J. Kim, K.-S. Lee,

High-performance multiblock PEMs containing a highly acidic fluorinated-hydrophilic domain for water electrolysis, Journal of Membrane Science, 638 (2021) 119694.

[18] H. Mendil-Jakani, I. Zamanillo Lopez, P.M. Legrand, V.H. Mareau, L. Gonon, A new interpretation of SAXS peaks in sulfonated poly(ether ether ketone) (sPEEK) membranes for fuel cells, Physical Chemistry Chemical Physics, 16 (2014) 11243-11250.

[19] K. Kim, B.-K. Jung, T. Ko, T.-H. Kim, J.-C. Lee, Comb-shaped polysulfones containing sulfonated polytriazole side chains for proton exchange membranes, Journal of Membrane Science, 554 (2018) 232-243.

[20] Y. Li, X. Zhang, G. He, F. Zhang, Sulfonated poly(phenylene sulfide) grafted polysulfone proton exchange membrane with improved stability, International Journal of Hydrogen Energy, 42 (2017) 2360-2369.

[21] N. Li, C. Wang, S.Y. Lee, C.H. Park, Y.M. Lee, M.D. Guiver, Enhancement of Proton Transport by Nanochannels in Comb-Shaped Copoly(arylene ether sulfone)s, Angewandte Chemie International Edition, 50 (2011) 9158-9161.

[22] G. Titvinidze, K.-D. Kreuer, M. Schuster, C.C. de Araujo, J.P. Melchior, W.H. Meyer, Proton Conducting Phase-Separated Multiblock Copolymers with Sulfonated Poly(phenylene sulfone) Blocks for Electrochemical Applications: Preparation, Morphology, Hydration Behavior, and Transport, Advanced

Functional Materials, 22 (2012) 4456-4470.

[23] T. Uchiyama, M. Kato, T. Yoshida, Buckling deformation of polymer electrolyte membrane and membrane electrode assembly under humidity cycles, Journal of Power Sources, 206 (2012) 37-46.

[24] M. Maalouf, C.-N. Sun, B. Pyle, M. Emery, G.M. Haugen, S.J. Hamrock, T.A. Zawodzinski, Factors enabling high mobility of protons and water in perfluorosulfonate membranes under low hydration conditions1, International Journal of Hydrogen Energy, 39 (2014) 2795-2800.

[25] E. Spohr, P. Commer, A.A. Kornyshev, Enhancing Proton Mobility in Polymer Electrolyte Membranes: Lessons from Molecular Dynamics Simulations, The Journal of Physical Chemistry B, 106 (2002) 10560-10569.

[26] T.J. Peckham, J. Schmeisser, M. Rodgers, S. Holdcroft, Main-chain, statistically sulfonated proton exchange membranes: the relationships of acid concentration and proton mobility to water content and their effect upon proton conductivity, Journal of Materials Chemistry, 17 (2007) 3255-3268.

[27] M. Yousefi Tehrani, S.H. Mirfarsi, S. Rowshanzamir, Mechanical stress and strain investigation of sulfonated Poly(ether ether ketone) proton exchange membrane in fuel cells: A numerical study, Renewable Energy, 184 (2022) 182-200.

[28] S. Choi, S.-H. Shin, D.-H. Lee, G. Doo, D.W. Lee, J. Hyun, J.Y. Lee, H.-T. Kim, Enhancing the durability of hydrocarbon-membrane-based polymer

electrolyte water electrolysis using a radical scavenger-embedded interlocking interfacial layer, Journal of Materials Chemistry A, 10 (2022) 789-798.

[29] K. Enomoto, S. Takahashi, T. Iwase, T. Yamashita, Y. Maekawa, Degradation manner of polymer grafts chemically attached on thermally stable polymer films: swelling-induced detachment of hydrophilic grafts from hydrophobic polymer substrates in aqueous media, Journal of Materials Chemistry, 21 (2011) 9343-9349.

[30] A. Albert, T. Lochner, T.J. Schmidt, L. Gubler, Stability and Degradation Mechanisms of Radiation-Grafted Polymer Electrolyte Membranes for Water Electrolysis, ACS Applied Materials & Interfaces, 8 (2016) 15297-15306.

[31] D. Zhao, J. Li, M.-K. Song, B. Yi, H. Zhang, M. Liu, A Durable Alternative for Proton-Exchange Membranes: Sulfonated Poly(Benzoxazole Thioether Sulfone)s, Advanced Energy Materials, 1 (2011) 203-211.

[32] Q. Feng, X.Z. Yuan, G. Liu, B. Wei, Z. Zhang, H. Li, H. Wang, A review of proton exchange membrane water electrolysis on degradation mechanisms and mitigation strategies, Journal of Power Sources, 366 (2017) 33-55.

[33] S. Adhikari, M.K. Pagels, J.Y. Jeon, C. Bae, Ionomers for electrochemical energy conversion & storage technologies, Polymer, 211 (2020) 123080.

[34] A.Y. Faid, A.O. Barnett, F. Seland, S. Sunde, NiCu mixed metal oxide catalyst for alkaline hydrogen evolution in anion exchange membrane water electrolysis, Electrochimica Acta, 371 (2021) 137837.

[35] A. Alobaid, C. Wang, R.A. Adomaitis, Mechanism and Kinetics of HER and OER on NiFe LDH Films in an Alkaline Electrolyte, Journal of The Electrochemical Society, 165 (2018) J3395-J3404.

[36] M. Suermann, B. Bensmann, R. Hanke-Rauschenbach, Degradation of Proton Exchange Membrane (PEM) Water Electrolysis Cells: Looking Beyond the Cell Voltage Increase, Journal of The Electrochemical Society, 166 (2019) F645-F652.

[37] S. Stiber, N. Sata, T. Morawietz, S.A. Ansar, T. Jahnke, J.K. Lee, A. Bazylak, A. Fallisch, A.S. Gago, K.A. Friedrich, A high-performance, durable and low-cost proton exchange membrane electrolyser with stainless steel components, Energy & Environmental Science, 15 (2022) 109-122.

**Table 3.1.** Quantitative values of key performance indicators.

| **Samples** | **Proton conductivity (mS cm$^{-1}$)**[a] | **Dimensional stability (%)**[b] | **Hydrogen barrier property (barrer$^{-1}$)**[c] | **Mechanical property (MPa)**[d] | **Thermal stability**[e] | |
|---|---|---|---|---|---|---|
| | | | | | **Area change (%)** | **Hydrogen permeability (barrer)** |
| **G-sPSS-1.95** | 0.291 | 40.35 | 27.84 | 19.86 | 47.89 | 30.51 |
| **MB-sPSS-1.91** | 0.226 | 47.06 | 33.06 | 15.18 | 64.76 | 38.04 |
| **N212** | 0.193 | 27.89 | 89.81 | 89.81 | 35.54 | 97.71 |

[a] Proton conductivity in water at 90 °C

[b] Area change (%) at 90 °C

[c] Hydrogen permeability at 80 °C

[d] Tensile strength of hydrated membranes

[e] Thermo-hydrolytic stability: product of area change and hydrogen permeability at 90 °C, 5 d

**Table 3.2.** General properties G-sPSS-1.47, G-sPSS-1.95, MB-sPSS-1.91, and N212.

| **Samples** | **IEC (meq g$^{-1}$)** | **Branching point (%)** | **Side chain MW (g mol$^{-1}$)** | **Inherent viscosity (dL g$^{-1}$)** |
|---|---|---|---|---|
| **G-sPSS-1.47** | 1.47 | 1.93 | 11000 | 1.66 |
| **G-sPSS-1.95** | 1.95 | 3.40 | 11000 | 1.50 |
| **MB-sPSS-1.91** | 1.91 | - | - | 0.61 |
| **N212** | 0.91 | - | - | - |

**Table 3.3.** Comparison of aromatic graft polymers reported for fuel cell technologies.

| Samples | Full aromaticity | Usage in PEMWE | Side chain | | IEC (meq g$^{-1}$) | Reference |
|---|---|---|---|---|---|---|
| | | | AB-type monomer | $SO_3H$ per benzene ring | | |
| **Comb-X** | X | X | X | 2/3 | 1.81, 2.06 | [19] |
| **PSf-g-sPS** | X | X | O | 1/1 | 0.8-1.8 | [20] |
| **PAES-g-SPPO** | O | X | O | 2/3 | 0.92-1.72 | [21] |

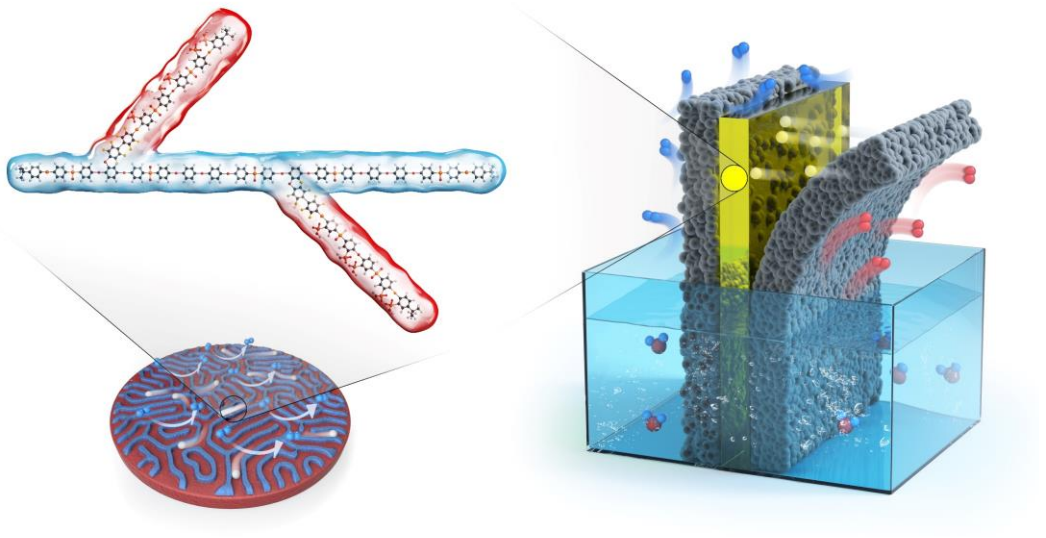

**Figure 3.1.** Schematic of highly sulfonated aromatic graft PEM-based PEMWE

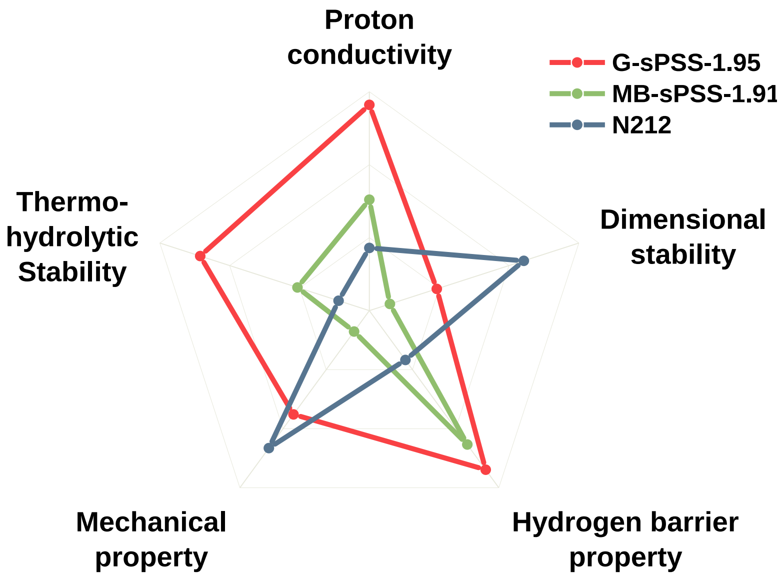

**Figure 3.2.** Spider chart of key performance indicators for PEMWE. Quantitatively defined criterion of each property is listed in Table 3.1

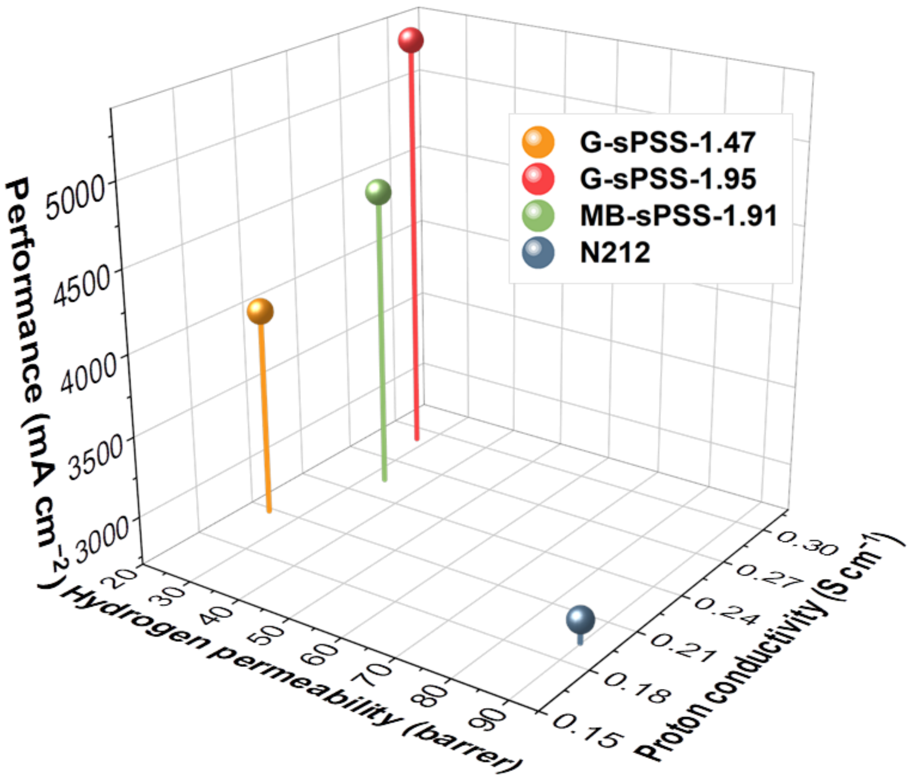

**Figure 3.3.** comparing the PEMWE performance (current density at 1.9 V, 90 °C) as a function of hydrogen permeability (PH2) (80 °C, 100% RH) and proton conductivity (σ) (90 °C, in water)

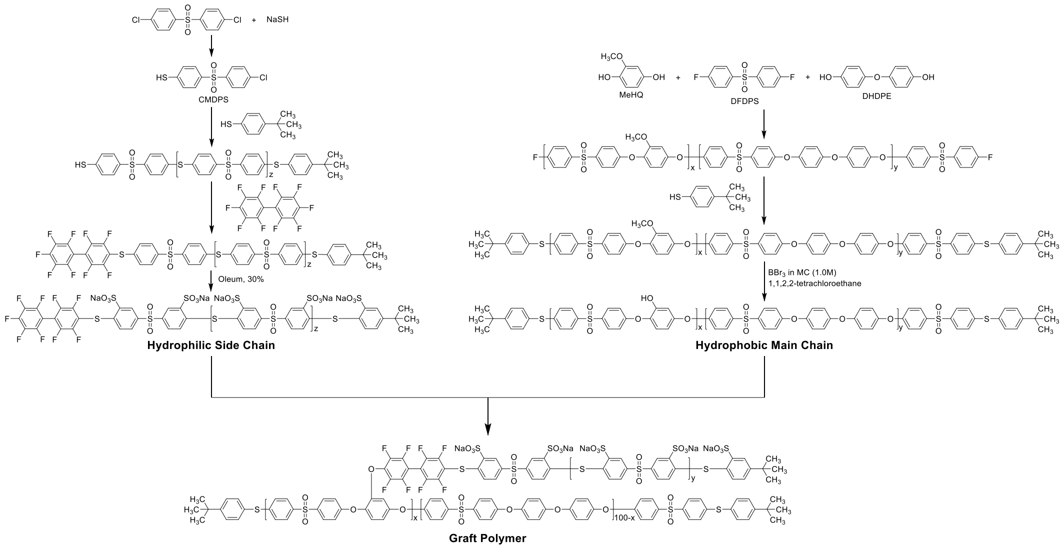

**Figure 3.4.** Synthesis of hydrophilic side-chain, hydrophobic main-chain, and graft polymer (G-sPSS-X)

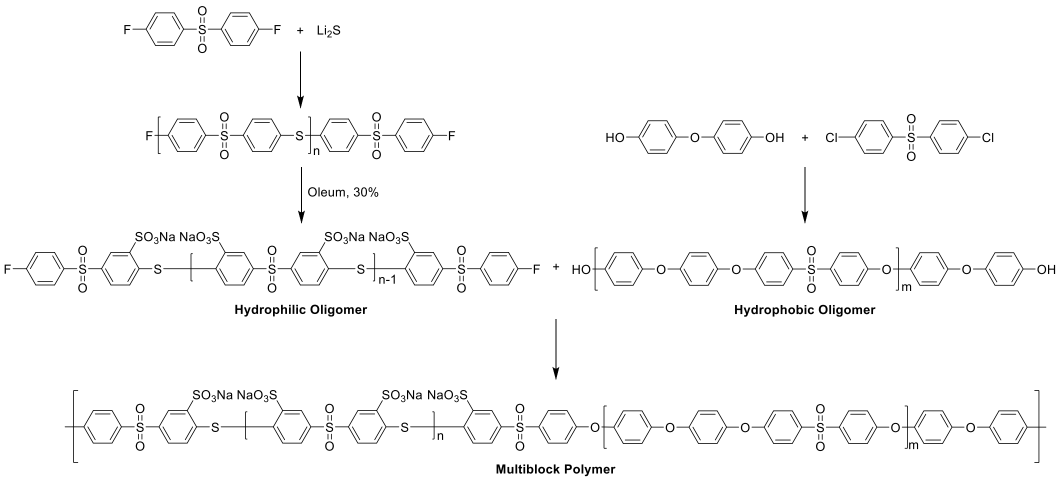

**Figure 3.5.** Synthesis of hydrophilic oligomer, hydrophobic oligomer, and multiblock polymer (MB-sPSS-X)

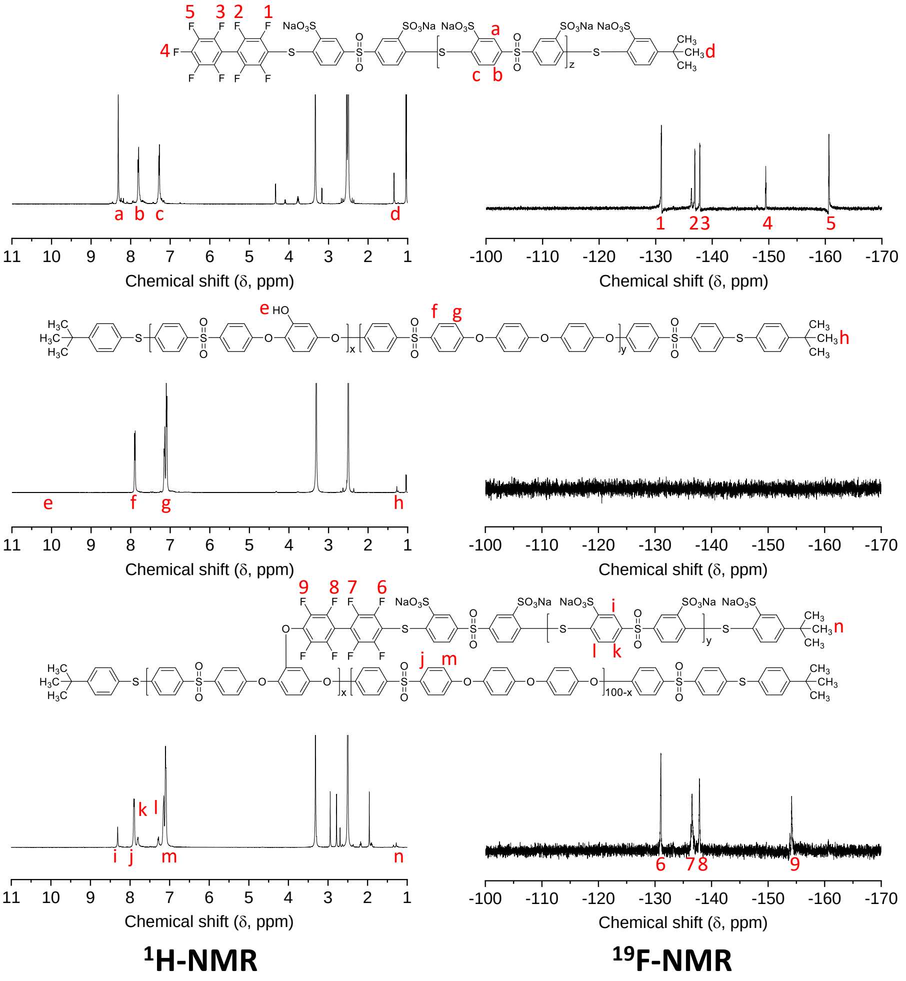

**Figure 3.6.** $^{1}$H and $^{19}$F-NMR of G-sPSS-1.47

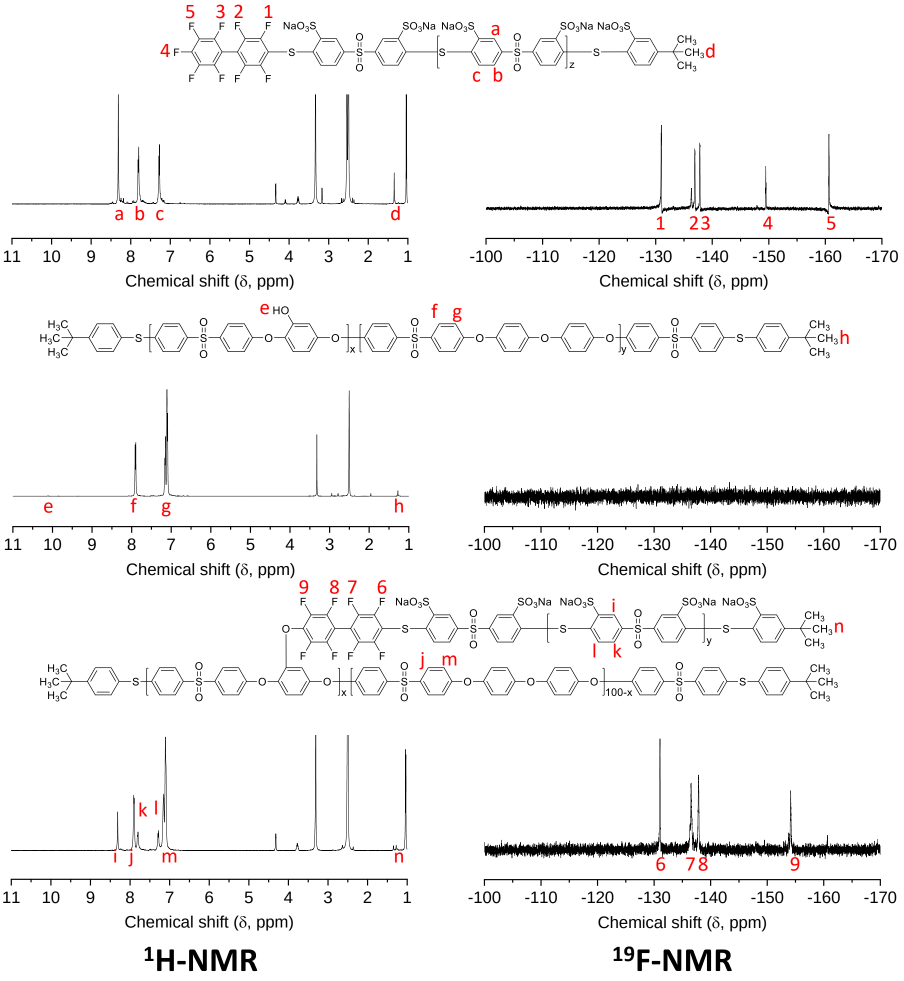

**Figure 3.7.** $^1$H and $^{19}$F-NMR of G-sPSS-1.95

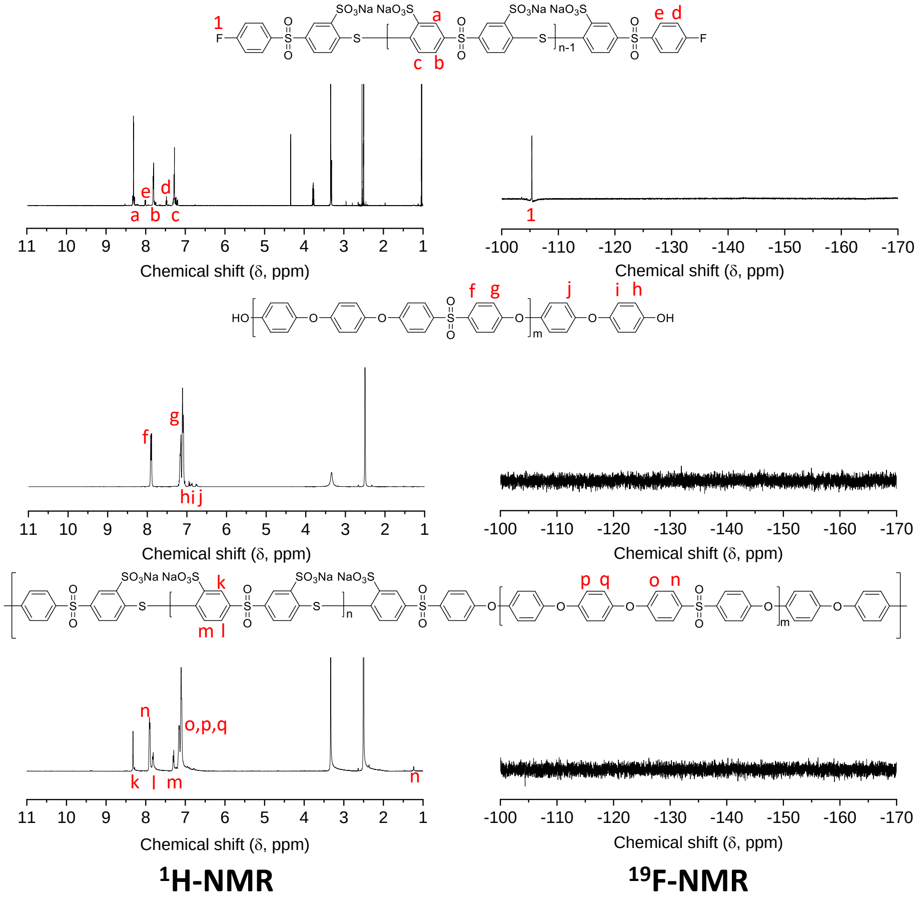

**Figure 3.8.** $^1$H and $^{19}$F-NMR of MB-sPSS-1.91

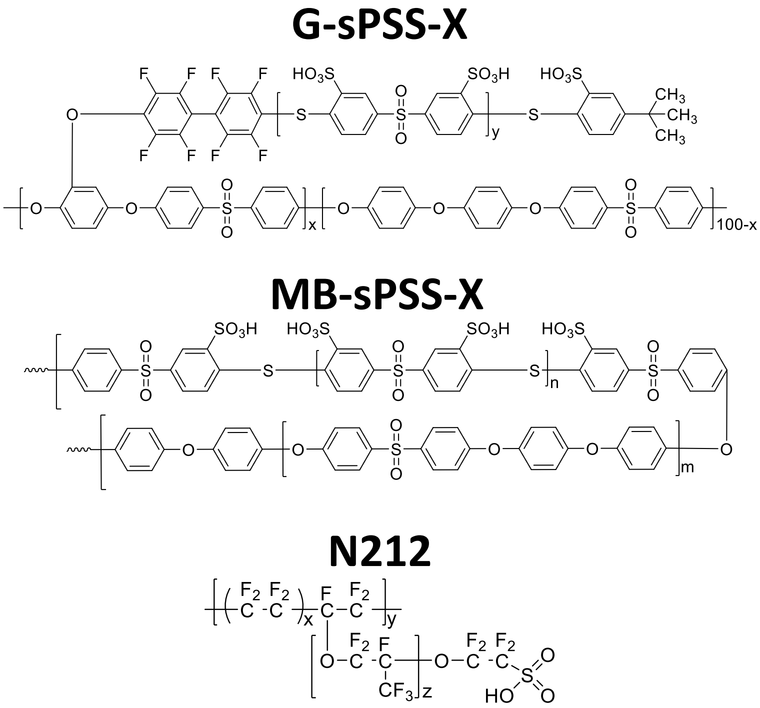

**Figure 3.9.** Chemical structures of graft (G-sPSS-X), multiblock (MB-sPSS-X), and PFSA (N212) PEMs

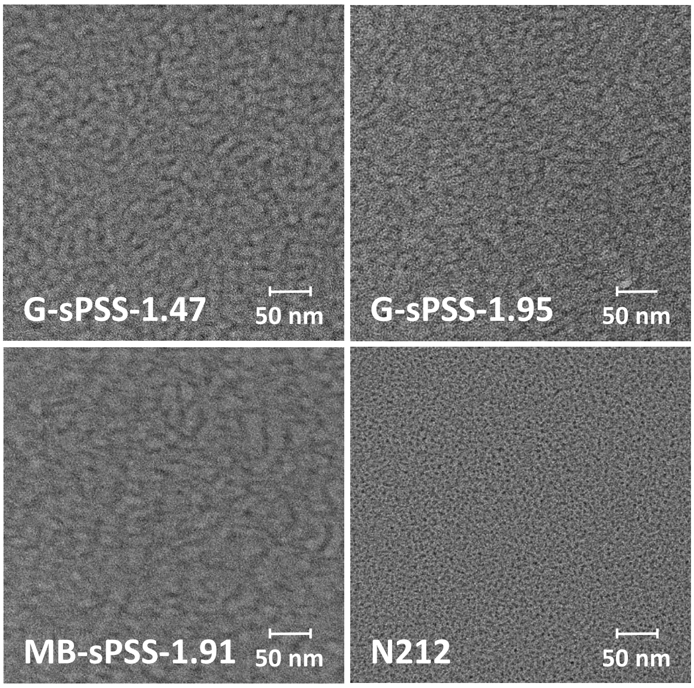

**Figure 3.10.** Lead-stained TEM images of PEMs under 50-nm scale. The dark and light domains represent hydrophilic and hydrophobic moieties, respectively

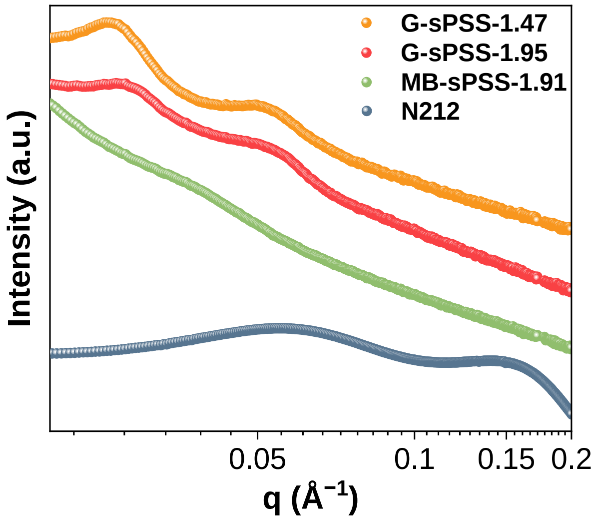

**Figure 3.11.** SAXS spectra of swollen PEMs at 25 °C

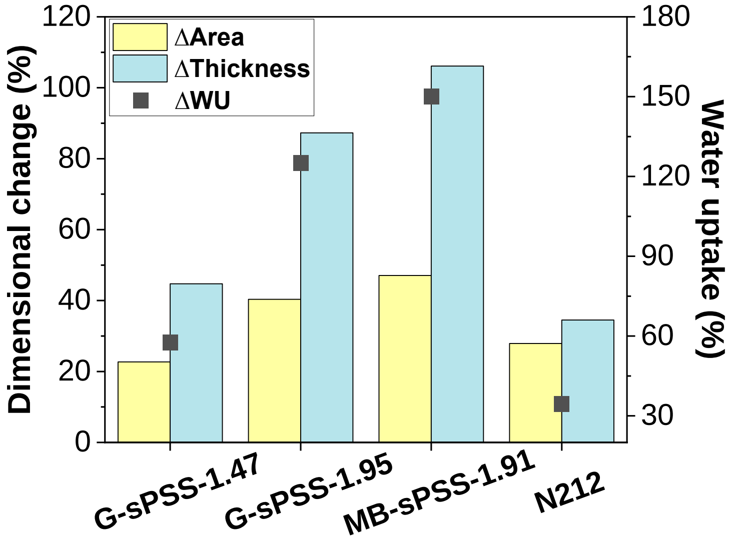

**Figure 3.12.** Dimensional change (area and thickness) and water uptake at 90 °C

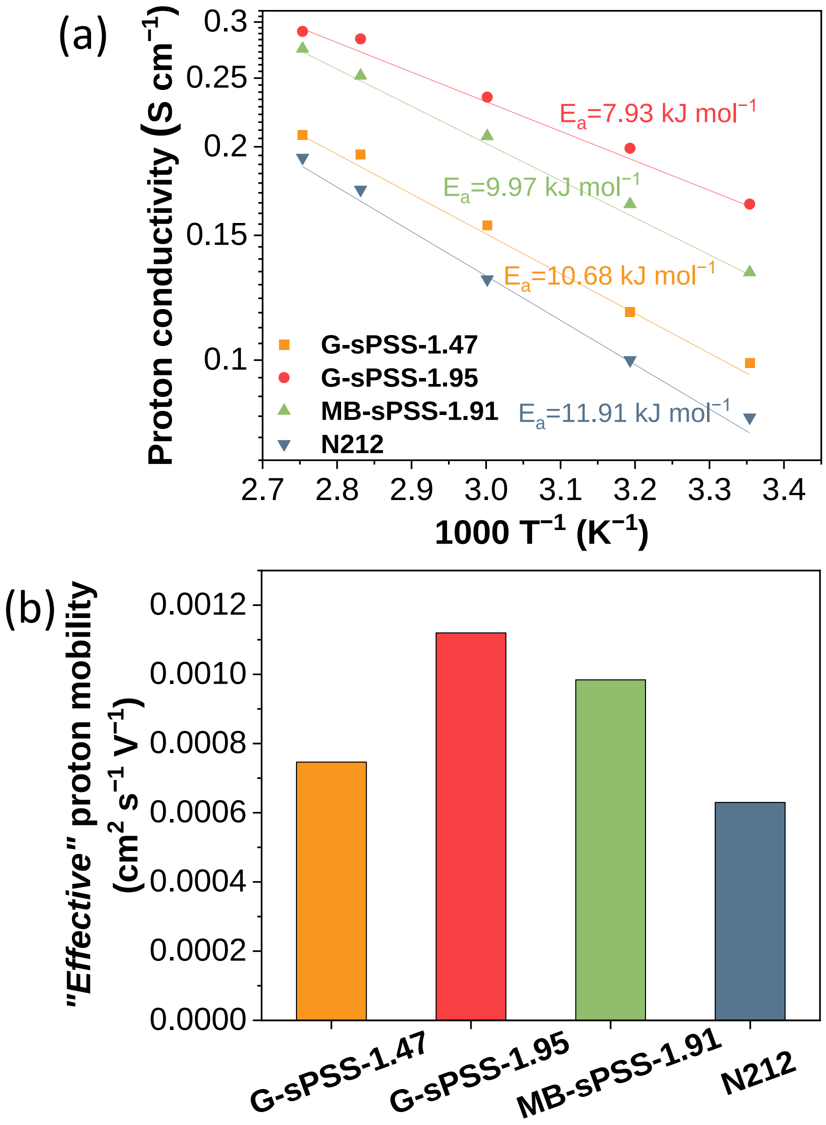

**Figure 3.13.** (a) Arrhenius plot for proton conductivity (σ) of the PEMs measured in water as a function of temperature (b) "Effective" proton mobility (μeff) of the PEMs at 25 °C

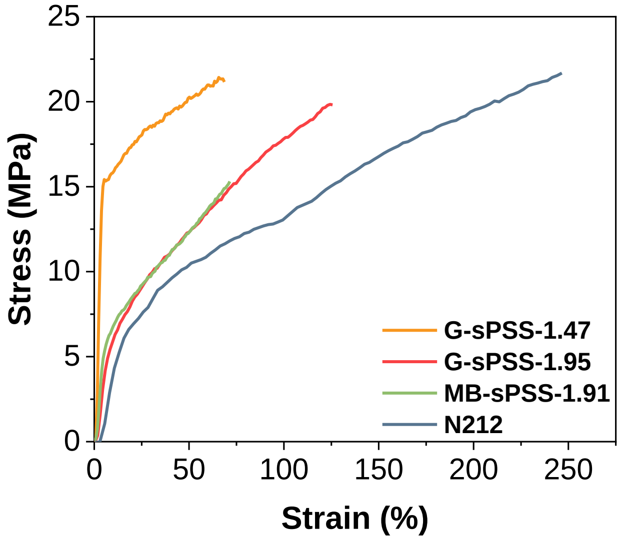

**Figure 3.14.** Stress–strain curves of swollen PEMs at 25 °C and 50% humidity

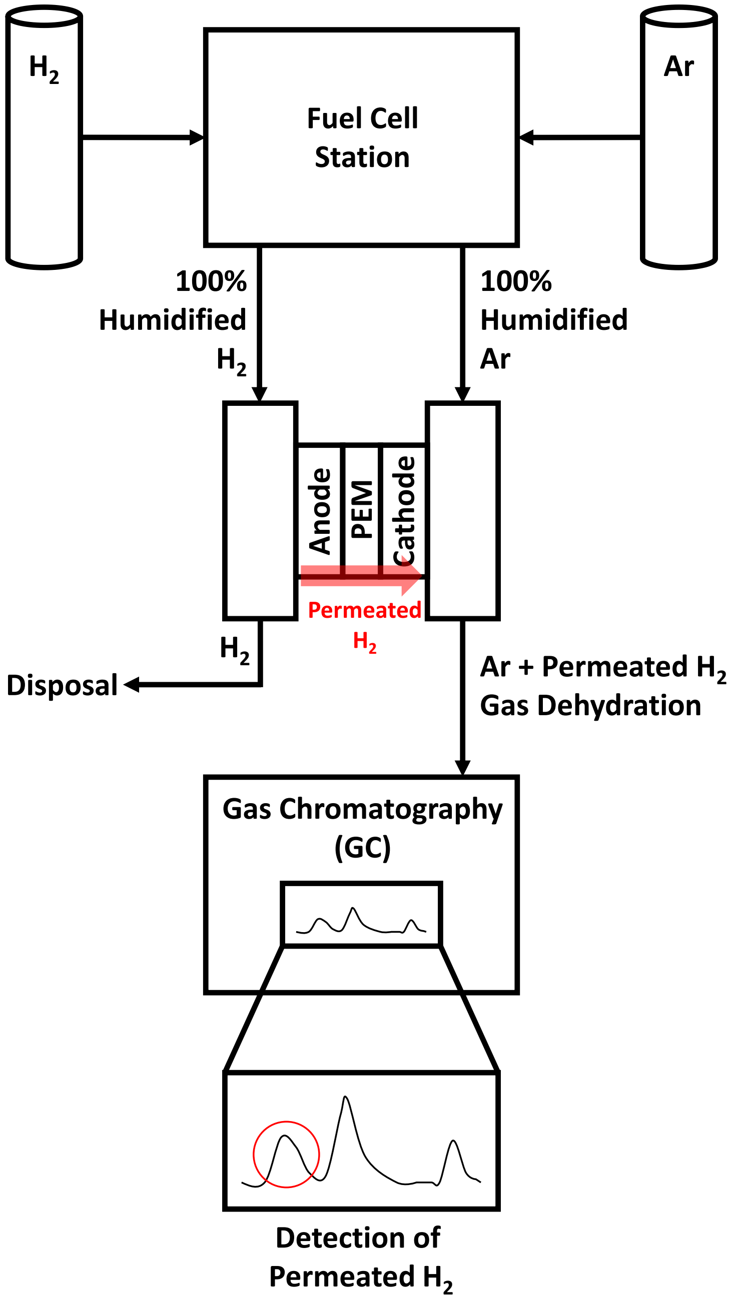

**Figure 3.15.** Schematic drawing of measuring system of hydrogen permeability with fuel cell station and gas chromatography.

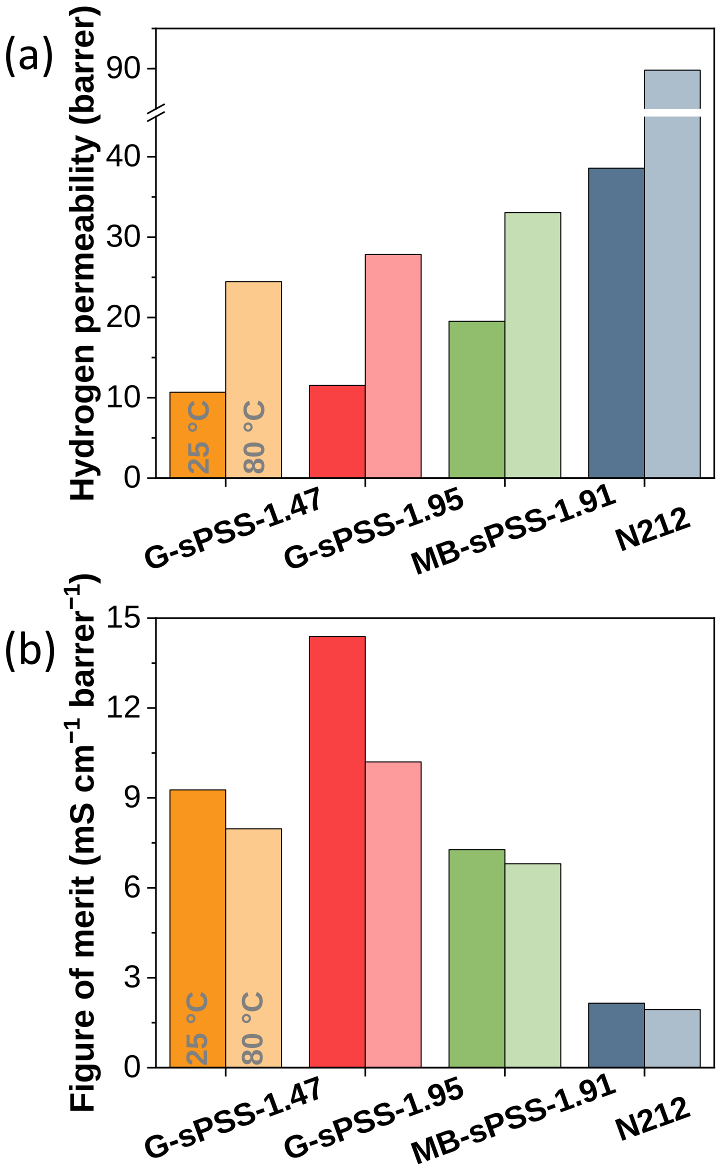

**Figure 3.16.** (a) Hydrogen permeability (PH2) at 100% RH, 25 °C (dark bar), and 80 °C (light bar) (b) FOM at 25 °C (dark bar) and 80 °C (light bar)

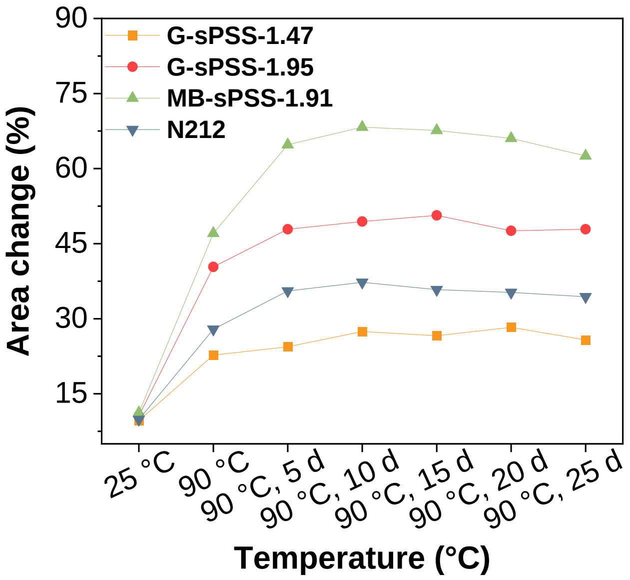

**Figure 3.17.** Area change (ΔA) of PEMs at 25 and 90 °C and post THST (PEMs were immersed in water at 90 °C for 5–25 days)

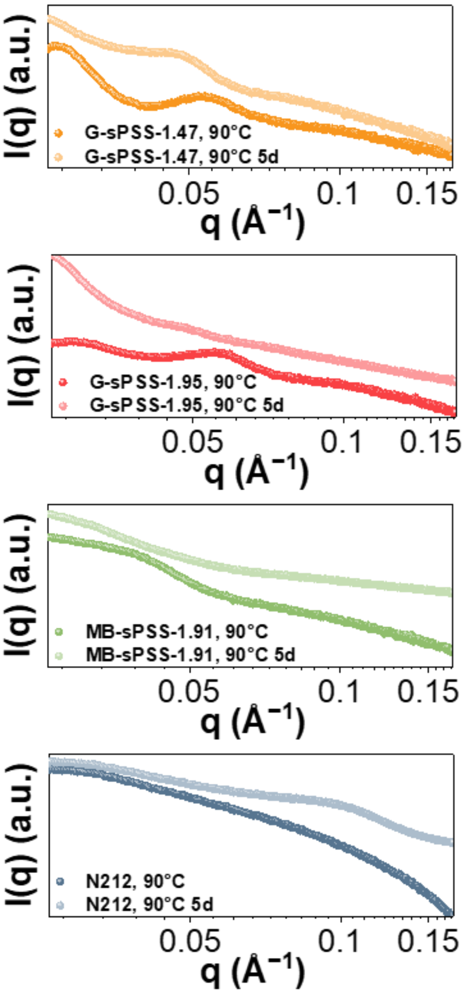

**Figure 3.18.** SAXS spectra of PEMs at 90 °C (dark line) and post THST (light line)

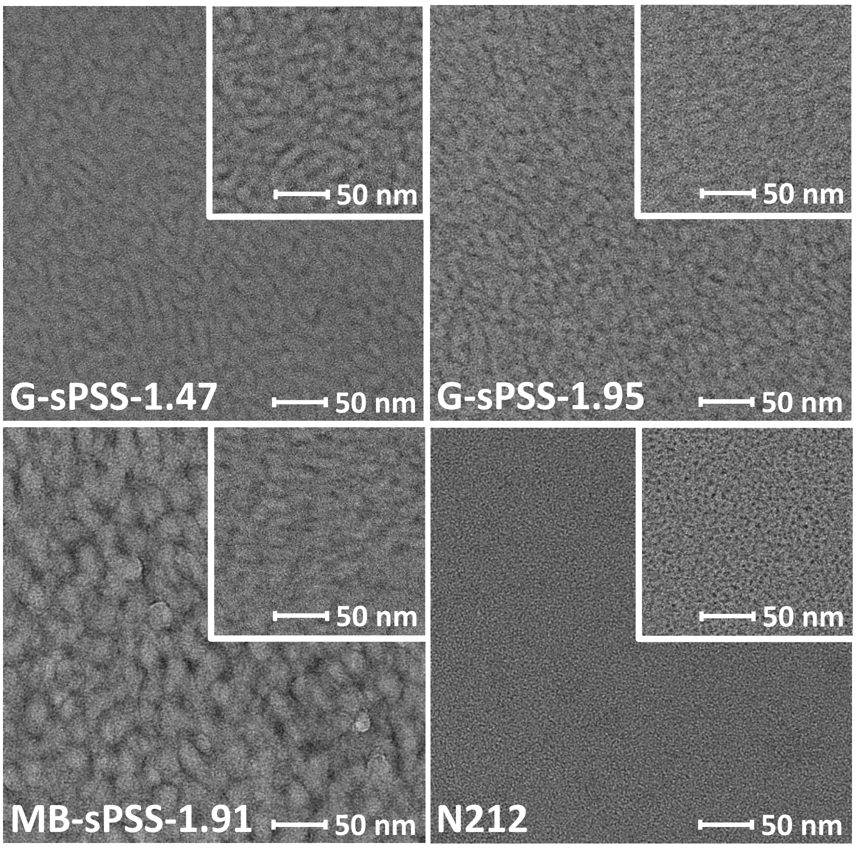

**Figure 3.19.** Lead-stained TEM images of PEMs at 25 °C (quarter image) and post THST (full image) under 50 nm

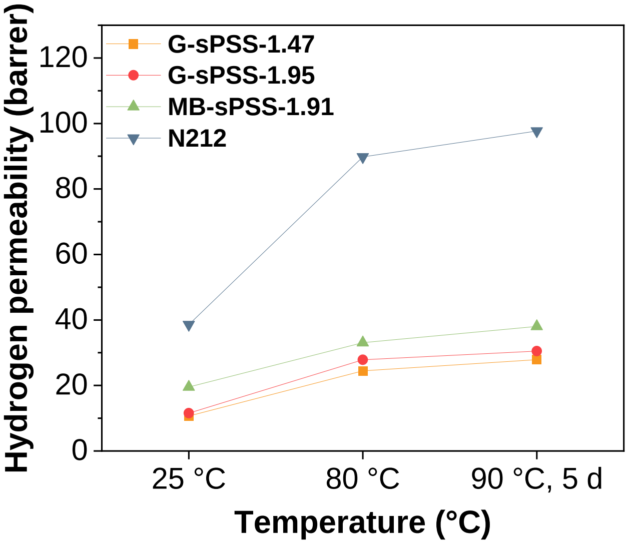

**Figure 3.20.** Hydrogen permeability (PH2) under 100% RH at 25 and 80 °C and post THST

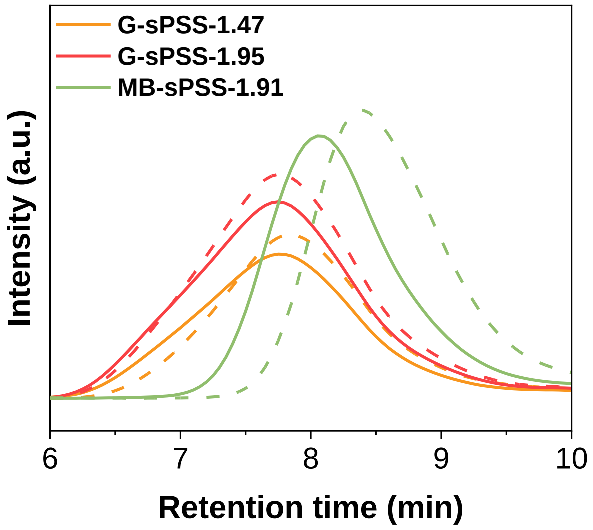

**Figure 3.21.** Gel permeation chromatography results of PEMs at the pristine state (solid line) and post THST (dash)

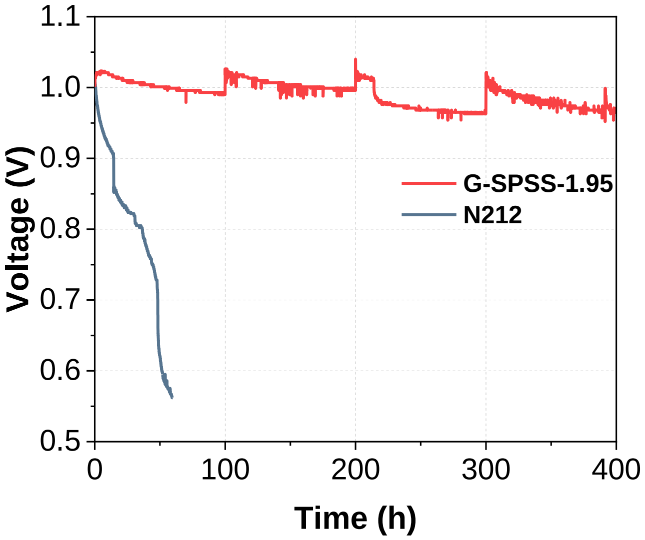

**Figure 3.22.** OCV hold test to measure in situ chemical stability of G-sPSS-1.95 and N212 MEAs

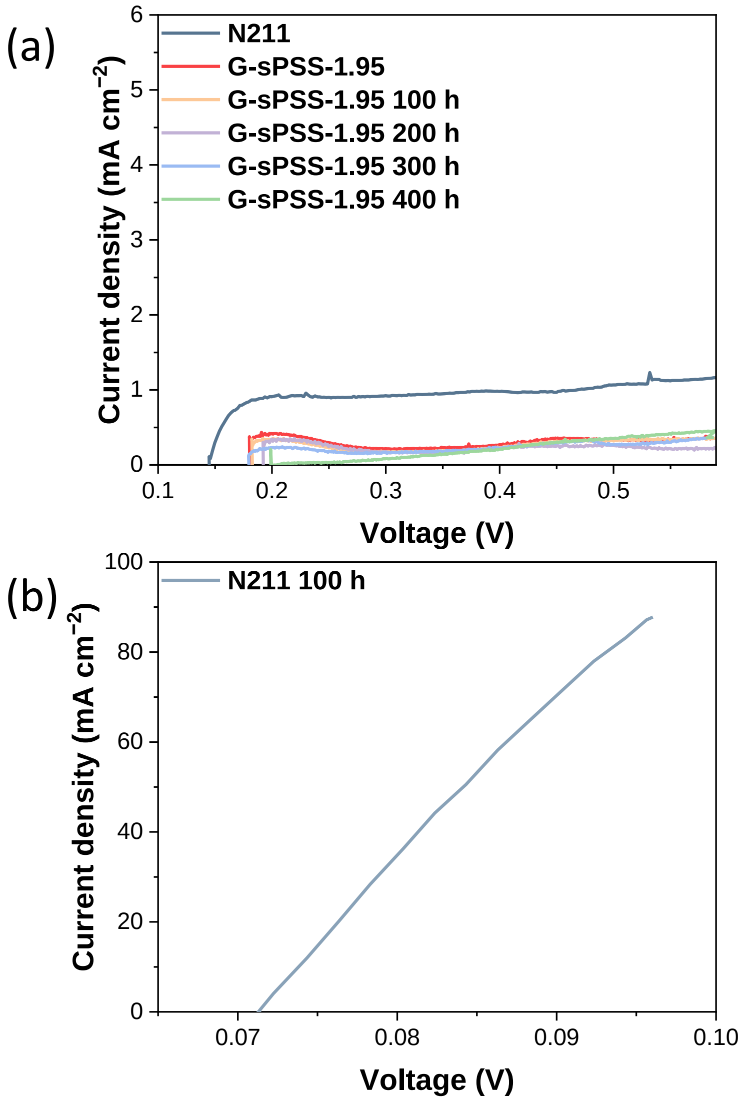

**Figure 3.23.** Linear sweep voltammetry (LSV) of (a) G-sPSS-1.95 (0-400 h) and N211 (0 h) and (b) N211 (100 h)

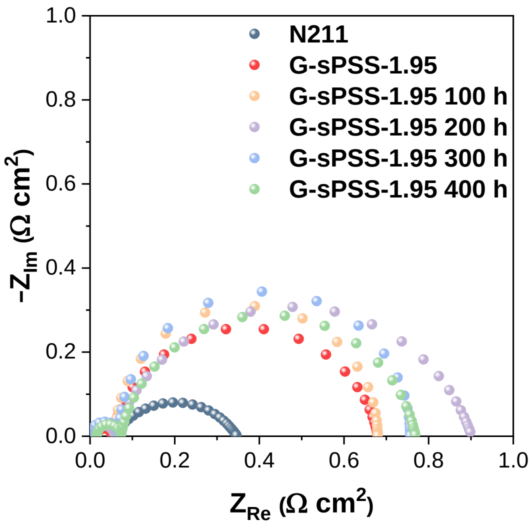

**Figure 3.24.** Nyquist plots of G-sPSS-1.95 (0-400 h) and N211 (0 h) after OCV test

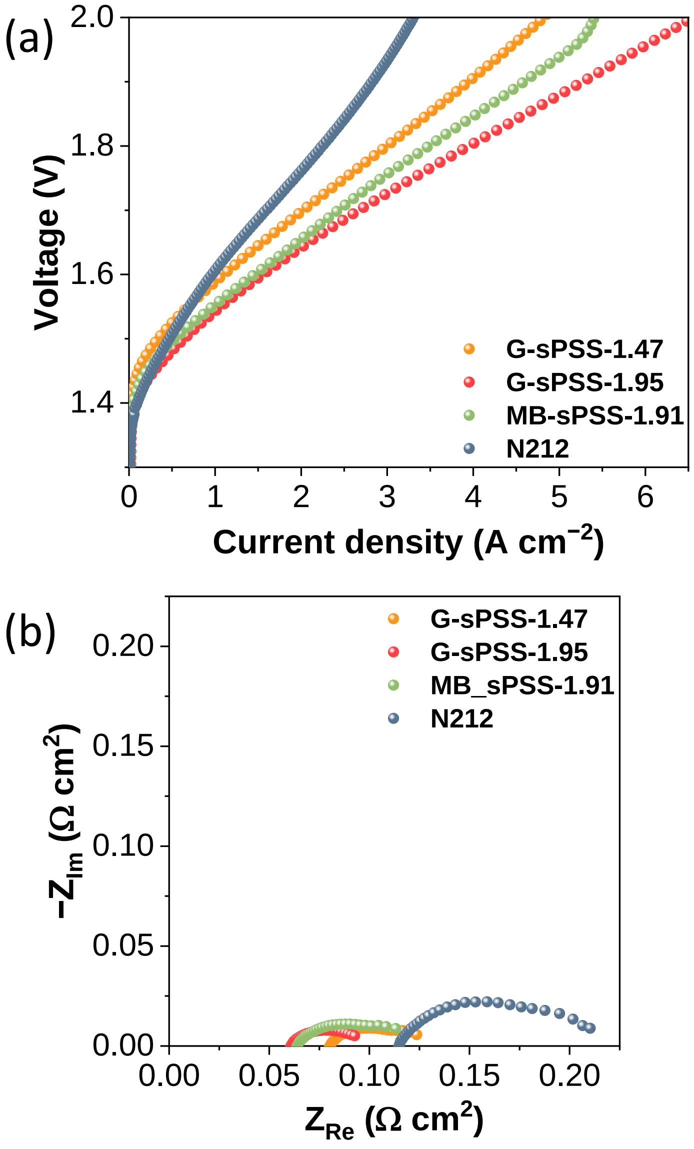

**Figure 3.25.** (a) Single-cell performance of PEMWE and corresponding (b) Nyquist plots obtained at 1.6 V

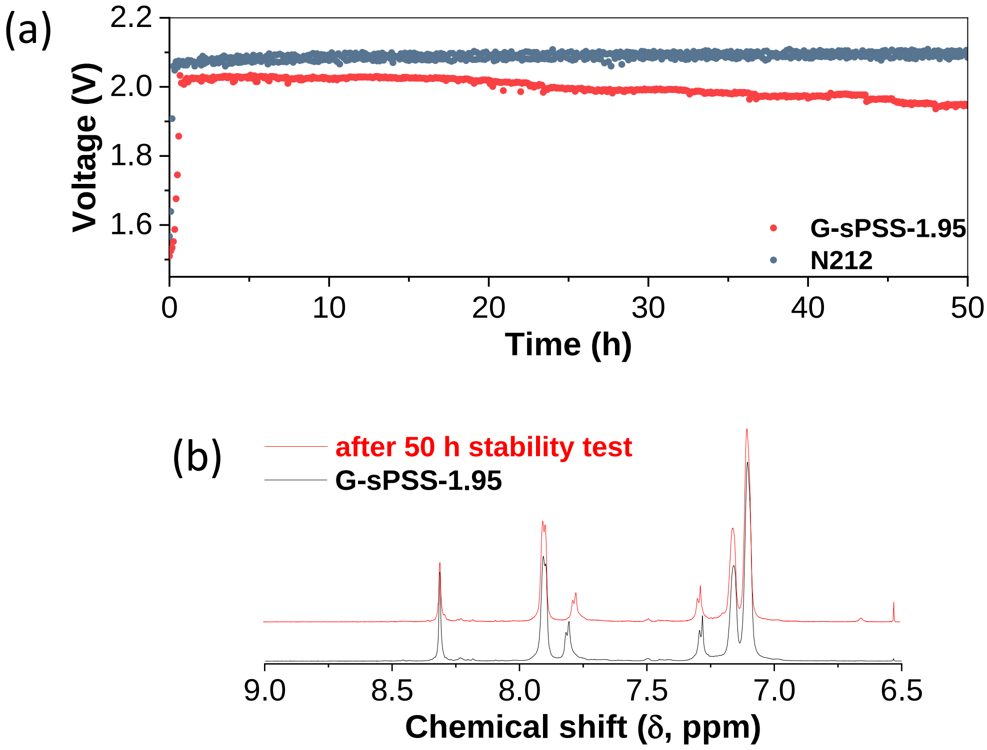

**Figure 3.26.** (a) Durability test operated at a constant current density of 1000 mA cm$^{-2}$ for 50 h and corresponding (b) $^1$H-NMR results before and after 50 h

# Chapter 4

# Structure-property relationship of versatile aromatic graft proton exchange membrane for fuel cell and water electrolysis

## 4.1. Introduction

Future hydrogen society employs proton exchange membrane fuel cell (PEMFC) and water electrolysis (PEMWE) for generating electricity and producing hydrogen gas [1]. Proton exchange membrane (PEM) is the key material for both of the applications, conducting proton and separating gas [2]. PEM requires excellent proton conductivity, low gas crossover, mechanical strength, dimensional, thermal, and chemical stability [3]. Despite the utilization of commercial perfluorosulfonated Nation for its dimensional and chemical stability, high cost and detrimental environmental effects hinders the usage for the future hydrogen society [4].

Sulfonated aromatic hydrocarbon-PEMs with ion-exchanging sulfonic acid groups have been developed as an alternative to Nafion to reduce the production cost and to increase the thermal stability [5]. The phase separation between the sulfonated hydrophilic moieties and the hydrophobic moieties induce well-connected proton-conducting channels, affecting not only the proton conductivity but also the hydrogen permeability and the dimensional stability [6]. Research on various structural architecture on sulfonated aromatic polymers was conducted to enhance the hydrophilic-hydrophobic phase-separated morphology [7]. Numerous random-architectured hydrocarbon-PEMs with controlled degree of sulfonation were reported in the early stage of development [8]. To enhance the hydrophilic-hydrophobic phase separation, multiblock-architectured hydrocarbon-PEMs, where the sulfonic acid groups were located densely together, were developed varying the block length and the ratio of hydrophilic and hydrophobic moieties [9]. Despite the improvement in proton conduction, further research on balancing the dimensional property and mechanical stability without compromising the proton conductivity and the hydrogen permeability is needed.

We previously reported an aromatic graft PEM, where the fully aromatic sulfonated side chain was grafted to fully aromatic main chain, mimicking the graft architecture of commercial Nafion. Unique morphology of interconnected hydrophilic channels with restricted domain size was observed inducing high proton conductivity and low hydrogen permeability. Despite its potential for an optimal PEM material, research on aromatic graft PEMs have seldom been reported due to the restricted structural design and unwanted crosslinking reaction [10]. From the limited number of studies, Kim et. al reported increased size and connectivity of the ionic domains of graft PEMs with increasing side chain length and ion exchange capacity (IEC) [11]. Li et. al investigated graft PEMs with similar IEC but with different side chain length and branching point induced different morphologies, where the graft PEM with the longer side chain showed more interconnected and larger ionic domains compared to the shorter side chain graft

PEM [12]. The distinct morphological behaviors from different side chain length and branching point can promote versatility on graft PEMs, where they can be optimized for various applications.

We prepared series of aromatic graft PEMs varying the side chain length and the branching point, and comprehensively investigated the structure-property relationship. Three types of side chain with different lengths were used to produce graft PEMs of various IECs by adjusting the percentage of branching point of the main chain, depicted in the schematic drawing in Figure 4.1. The variation of side chain length and branching point affected the morphology, producing different behaviors on water uptake, dimensional change, proton conductivity, and hydrogen permeability. In this paper, we propose that graft PEM with short side chain is more suitable for PEMFC from the favorable properties at reduced humidity, and graft PEM with long side chain is more suitable for PEMWE from the excellent properties at hot-water immersed condition.

# 4.2. Experimental

## Materials

Sodium hydrosulfide hydrate, potassium carbonate, calcium carbonate, 2-naphthalenethiol, decafluorobiphenyl, 2-methoxyhydroquinone, lithium sulfide, anhydrous dimethyl sulfoxide (DMSO), anhydrous 1-methyl-2-pyrrolidinone (NMP), anhydrous N,N-dimethylacetamide (DMAc), anhydrous toluene, anhydrous chloroform, fuming sulfuric acid (30% free SO3 basis), boron tribromide solution (1.0 M in methylene chloride), and isopropanol (IPA) were purchased from Sigma-Aldrich. 4,4'-Dihydroxydiphenyl ether (DHDPE) was purchased from TCI Chemicals. Hydrochloric acid (30%) was purchased from OCI Company Ltd. Sodium chloride (99%), sodium hydroxide (>98%), 2-propanol, methyl alcohol, and dimethyl sulfoxide were purchased from Samchun Chemicals. All of the chemical reagents above were used without further purification. 4,4'-Difluorodiphenyl sulfone (DFDPS) and 4,4'-dichlorodiphenyl sulfone (DCDPS) were purchased from Career Henan Chemical Co. and Solvay, respectively, and were recrystallized before use.

## Synthesis

To avoid crosslinking in graft reaction, the side-chain was synthesized from an AB-type monomer, 4-chloro-4'mercaptodiphenyl sulfone (CMDPS). CMDPS was synthesized by adding DCDPS (100 g, 0.32 mol) and anhydrous DMSO (42% solid content) to 300-mL round bottom flask (RBF) with argon gas inlet, and increasing the temperature to 60 °C until the solution fully dissolved for 1 h. Then, sodium hydrosulfide hydrate (25.14 g, 0.32 mol), potassium carbonate (21.88 g, 0.16 mol), and anhydrous DMSO were added to the solution, changing the solution from transparent to green. The solution was heated to 80 °C and maintained for 4 h, in which the solution turned to orange. The reacted solution was precipitated in 5wt% cold KOH solution. After extraction with ethyl acetate, the solution was titrated to pH 7 with hydrochloric acid until white precipitates were formed. The white precipitates were washed with deionized water and filtered. The filtered solid was dried in a vacuum oven at 80 °C overnight.

The side-chain of the graft polymer was synthesized from AB-type monomer, CMDPS. To prepare a side-chain with a molecular weight of 9000 g $\mathrm{mol}^{-1}$, CMDPS (27.34 g, 0.096 mol), 4-*tert*-Butylbenzenethiol (BBT) (0.91 g, 0.0055 mol), potassium carbonate (8.41 g, 0.061 mol), and anhydrous NMP (137.91 mL, 17% solid content) were added in a 250-mL RBF charged with argon. The solution reacted for 3 h at 130 °C, and was cooled to room temperature. The target molecular weight was achieved by controlling the molar feed ratios of CMPDS and BBT. To avoid crosslinking in graft reaction, additional feed of end-capper BBT was added to the solution. BBT (0.091 g, 0.00055 mol), potassium carbonate (0.090 g, 0.00065 mol), and anhydrous DMAc (0.88 mL, 17% solid content) were added to schlenk flask charged with argon, and the solution was heated to 130 °C for 2 h. The reacted solution was poured into the CMDPS-containing solution, and the solution was heated to 130 °C for 2 h. Meanwhile decafluorobiphenyl (DFBP) (19.72 g, 0.059 mol) and anhydrous NMP (613.51 mL, 6% solid content) were dissolved in a 300-mL RBF at room temperature. The CMDPS-containing solution was dropped into the DFBP-containing solution at 0 °C using an ice bath to avoid undesirable crosslinking, and was stirred for 2 h charged with argon. The final solution was precipitated in methyl alcohol, and was washed several times with methyl alcohol. The product was dried *in vacuo* at 80 °C overnight.

Functionalization of sulfonic acid group was achieved with post-sulfonation process. The product obtained from the previous step (24.20 g, 0.0027 mol, 1 equiv.) and fuming sulfuric acid (73.87 g, 5 equiv.) were added to 250-mL jacketed RFB at −10 °C for 5 days. The product was poured in ice water bath, and was precipitated by saturating the aqueous solution with sodium chloride. The filtered product was dissolved in deionized water and was titrated to pH 7 with 10 N sodium hydroxide solution. The dissolved solution was precipitated by saturating with sodium chloride. The filtered solid was dried under vacuum at 60 °C overnight. The vacuum-dried product was then dissolved in DMSO. The solution was then filtered to remove excess sodium chloride, and the filtrate was precipitated and washed in 2-propanol several times. The final product was dried *in vacuo* at 60 °C overnight.

The main-chain of graft polymer with pendant methoxy groups (120000 g $mol^{-1}$) were synthesized by adding 2-methoxyhydroquinone (0.60 g, 0.0043 mol), DHDPE (12.51 g, 0.062 mol), DFDPS (16.88 g, 0.066 mol), potassium carbonate (10.86 g, 0.079 mol), anhydrous DMAc (120 mL, 20% solid content), and anhydrous toluene (120 mL) in 250-mL RBF charged with argon by slowly increasing the temperature to 175 °C while azeotropically removing water by refluxing toluene. After fully removing the toluene through dean-stark trap, the solution was reacted for 5 h at 175 °C, and was cooled to room temperature. BBT (0.83 g, 0.0050 mol), potassium carbonate (0.83 g, 0.0060 mol), and anhydrous DMAc (6.64 mL, 20% solid content) were added to schlenk flask charged with argon, and the solution was heated to 130 °C for 2 h. The BBT-containing solution was poured into the DHDPE-containing solution, and the mixture was stirred at 130 °C for 2 h. The product was precipitated in deionized water, and washed with deionized water and 2-propanol several times. The filtered product was vacuum-dried at 80 °C overnight.

The pendant methoxy group of the polymerized main-chain was demethylated to pendant hydroxy group. The methoxy-containing polymer (26.88 g, 0.064 mol) was dissolved in anhydrous chloroform (284.57 mL, 6% solid content) at room temperature charged with argon. After the polymer was completely dissolved, boron tribromide solution (25.09 mL, 0.025 mol, 6 equiv.) was dropped into the solution, and was reacted for 3 hours. The product was precipitated into methyl alcohol, and was thoroughly washed with methyl alcohol. The filtered solid was dried *in vacuo* at 80 °C overnight.

Graft polymer was synthesized by nucleophilic substitution reaction between highly reactive DFBP group of side-chain and hydroxy group of main-chain. The main-chain polymer (1.39 g, 0.0034 mol) and anhydrous DMAc (50.75 mL, 2.59 wt%) were dissolved in a 100-mL RBF charged with argon at 80 °C for 2 h. After the solution was fully dissolved, potassium carbonate (0.30 g, 0.0022 mol) was added, and the solution was heated to 110 °C for 1 hour. Meanwhile, the side-chain polymer (6 g, 0.00055 mol, 2.5 equiv. of hydroxy group mol %) was dissolved in anhydrous DMAc (23.30 mL, 20% solid content) at 80 °C until fully dissolved. Both solutions were cooled to room temperature after reaction. The side-chain solution was injected into the main-chain solution at room temperature, and the mixed solution was heated to 80 °C for 48 h. The product was precipitated to 2-propanol, and was washed several times with deionized water and 2-propanol. The filtered product was dried *in vacuo* at 60 °C overnight.

## Membrane preparation

The membranes were prepared by dissolving polymer into anhydrous NMP (18 wt%), and filtering with 5-μm Teflon syringe filters. The solutions were casted with doctor-blade applicator, and dried at 60 °C overnight. The dried membranes were immersed into 1.5 M $H_2SO_4$ aqueous solution at room temperature for 24 h, and subsequently in deionized water at room temperature for 24 h.

## Polymer characterization

Ion exchange capacity (IEC) was measured by adding acid-treated membrane to 100-mL of 0.01 M NaCl aqueous solution. The solution was stirred for 24 h, substituting $H^+$ to $Na^+$. IEC was measured by acid titration method using an autotitrator (Metrohm 794 Basic Titrino), titrating with 0.01 M sodium hydroxide (NaOH) aqueous solution. IEC was calculated by the following equation:

$$IEC \ \ (meq \ \ g^{-1}) = \frac{V \times C}{w},$$

where $V$ is the volume of the aqueous solution of 0.01 M NaOH, titrated to pH 7; $w$ is the weight of the dried sample (g); and $C$ is the molar concentration of the NaOH aqueous solution.

To measure the inherent viscosity (IV), polymer was dissolved in NMP (0.5 g $dL^{-1}$) and filtered with a 5-μm syringe filter. IV was measured in a water bath at 25 °C using a Cannon-Ubbelohde viscometer.

The nuclear magnetic spectroscopy (NMR) samples were prepared by dissolving the synthesized product in deuterated dimethyl sulfoxide (DMSO-$d_6$). The $^1H$ and $^{19}F$ NMR spectra were obtained on a Bruker Avance NEO (500 MHz) spectrometer. Gel permeation chromatography (YL9120 UV/Vis Detector) with YL9112 Isocratic pump and Shodex KF-805L column was used to determine number-average molecular weight ($M_n$). The flow rate of the eluent (HPLC grade DMAc with 0.05 M LiBr) was 1.0 $mLmin^{-1}$. Calibration was conducted using polystyrene standards.

## PEM characterization

The acid-treated membrane was immersed in an aqueous solution of 0.5 M lead acetate for 24 h to replace the $H^+$ form with the $Pb^{2+}$ form. Lead, which was on the surface of the membrane, was washed with deionized water for 24 h, and the membrane was sufficiently vacuum-dried at 80 °C. The dried membrane was prepared by a Leica EM UC6 ultramicrotome, and the TEM images were obtained on a TECNAI G2 T-20S microscope.

SAXS measurements were taken from the Pohang Accelerator Laboratory (PAL) located in Pohang, Republic of Korea using PLS-II 3C beamline. The thickness of the analyzed membranes were fixed at 200 μm for accurate comparison. The data was corrected with background-subtraction. The scattering vector was calculated by the following equation,

$$\mathrm{q} = \frac{4\pi}{l(sin2\theta)}$$

where $l$ represents the wavelength of the Cu Kα radiation ($\lambda$=1.541Å) and $2\theta$ represents the scattering angle. The inter-domain space (d) was measured by the following equation,

$$\mathrm{d} = \frac{2\pi}{q_{max}}$$

where $q_{max}$ represents the maximum q value ($10^{-10}$ $\mathrm{m}^{-1}$).

## Water sorption behavior

Acid-treated membrane was prepared and cut into a size of 2 cm × 2 cm. After immersing the cropped membrane in deionized water for 24 h at 25 °C, its weight, length, and thickness were measured. The weight, length, and thickness of the dried membrane were measured by dehydrating the membrane in a vacuum for 24 h at 50 °C. The dimensional change and water uptake were obtained by the following equations.

$$\Delta Area = \frac{l_{wet} \times l_{wet} - l_{dry} \times l_{dry}}{l_{dry} \times l_{dry}} \times 100(\%)$$

$$\Delta Thickness = \frac{t_{wet} \times t_{wet} - t_{dry} \times t_{dry}}{t_{dry} \times t_{dry}} \times 100(\%)$$

$$Water\ \ Uptake\ \ (\%) = \frac{w_{wet} - w_{dry}}{w_{dry}} \times 100(\%),$$

where $l_{wet}$ and $t_{wet}$ are the length and thickness of the wet membrane, respectively; $l_{dry}$, and $t_{dry}$ represent the length, thickness, and volume of the dry membrane, respectively; $w_{wet}$ and $w_{dry}$ represent the weights of the wet and dry membranes, respectively.

The hydration number (λ) was calculated as the average number of water molecules per sulfonic acid group in the hydrated state.

$$\lambda = \frac{[H_2O]}{[SO_3 -]} = \frac{water\ \ uptake\ \ (\%) \times 10}{18 \times IEC\ \ (meq\ \ g^{-1})}$$

The acid concentration [$-SO_3H$] was calculated by multiplying weight of the dry membrane divided by the volume of the wet membrane with IEC.

$$[-SO_3H] = \frac{w_{dry}(g)}{Volume_{wet}(cm^3)} \times IEC\ \ (meq\ \ g^{-1}).$$

## Proton transport

To measure the proton conductivity (σ) in the wet state, AC impedance spectroscopy (ACIS) was performed by the 4-probe method at 25-90 °C and relative humidity (RH) of 100% utilizing a Solatron-1280 impedance/gain-phase analyzer (Solatron), and the frequency was measured with conversion in the range of 0.1–10,000 Hz. The value of the calculated impedance was converted to the proton-conductivity value through the following equation:

$$Proton\ \ Conductivity\ \ (S\ \ cm^{-1}) = \sigma = \frac{1}{R} \times \frac{L}{A},$$

where $R$ is the measured impedance value (Ω), $L$ is the distance between the measured electrodes, and $A$ is the cross-sectional area (cm$^2$) of the ion-exchange membrane that was utilized for the measurement.

The *"effective"* proton mobility ($\mu_{\mathrm{eff}}$) is the normalized proton conductivity value after the removal of the effect of the acid concentration. It can be calculated by the following equation:

$$\mu_{eff} = \frac{\sigma}{F \times [-SO_3H]}$$

where $F$ is Faraday's constant and $\sigma$ (S cm$^{-1}$) is the proton conductivity at 25-90 °C and 100% RH.

## Hydrogen permeability

To measure hydrogen gas permeability ($P_{H2}$), a system was developed connecting fuel cell station (SFC-TS, Fuel cell technologies Inc.) to gas chromatography (GC, YL6500 GC, Young In) equipped with a thermal conductivity detector. Between EPDM gaskets (210 μm) and flow field plates, a membrane (t = thickness) was placed without catalyst layers and gas diffusion layers. The humidified (100% RH) $H_2$ and Ar were each fed into anode and cathode side of a cell. The Ar, which was permeated through membrane, was passed to the GC quantifying the concentration of the permeated $H_2$ ($C_H$) in Ar. $P_{H2}$ was evaluated using the following equation,

$$P_{H2} = \frac{C_H \times v \times t}{A \times \Delta p}$$

where v is the Ar flow rate at STP (2750 mL $\text{min}^{-1}$), A is the active area (7.5 $\text{cm}^2$), and $\Delta p$ is the difference of $H_2$ partial pressure across the membrane. The unit for P is (molm $\text{m}^{-2}\text{s}^{-1}\text{Pa}^{-1}$) (1 molm $\text{m}^{-2}\text{s}^{-1}\text{Pa}^{-1} = 2.987 \times 10^{15}$ barrer).

## 4.3. Results and discussion

### Synthesis

Graft polymer was synthesized *via* polymer analogous reaction, where one end of the side chain was exclusively reactive, illustrated in Figure 4.2. Side chain was synthesized with desired molecular weight controlling the molar feed ratio of AB-type monomer and end-capper (4-tert-butylbenzenethiol). The AB-type monomer, 4-chloro-4′-mercaptodiphenyl sulfone (CMDPS), was synthesized with high purity, as previously reported in Chapter 3. The side-chain was polymerized with different functional groups at each end to avoid undesirable crosslinking during graft reaction, which could lead to gelation and difficult membrane fabrication. One end of the side chain was functionalized with highly reactive decafluorobiphenyl (DFBP) group, and the other end was functionally end-capped. The fluorine of functionalized DFBP group was detected in $^{19}$F-NMR (Figure 4.3b) at −131, −137, −138, −149, and −161 ppm (peaks 1-5). The protons (peak d) of the end-capper, 4-tert-butylbenzenethiol, was detected at 1.35 ppm in $^{1}$H-NMR (Figure 4.3a). The sulfonic acid groups were introduced to hydrophilic side chain using 30% oleum *via* post-sulfonation method.

Main chain was polymerized with desired branching point and molecular weight by controlling the molar feed ratio. The functional group, 2′-methoxyhydroquinone, was subjected to demethylation, resulting in reactive hydroxy group. The demethylation process was confirmed by the disappearance of the methoxy peak from the $^1$H NMR spectrum at 3.69 ppm in Figure 4.4c. Both ends of the main-chain were end-capped with 4-tert-butylbenzenethiol to avoid undesirable crosslinking reaction. The protons (peak g) of 4-tert-butylbenzenethiol was confirmed at 1.35 ppm in $^1$H-NMR.

Graft polymer was synthesized *via* nucleophilic aromatic substitution reaction between the hydroxy group of the hydrophobic main chain and the DFBP group of the hydrophilic side chain. The reaction was proceeded at low temperature of 80 °C to minimize the crosslinking of highly reactive DFBP groups and to prevent the ether–ether exchange reaction. The protons (peaks h, j, k) of side chain repeat unit were detected at 8.31, 7.80, and 7.28 ppm, and the protons (peaks i, l) of main-chain repeat unit were detected at 7.89 and 7.11 ppm in $^1$H-NMR in Figure 4.4e. The disappearance of fluorine at −149 ppm, para position to the DFBP group, in $^{19}$F-NMR indicated the completion of the reaction.

Graft polymers synthesized from short (7800 g mol$^{-1}$), medium (11000 g mol$^{-1}$), and long (15000 g mol$^{-1}$) side chain length were designated as SG-X, MG-X, and LG-X, respectively, where X indicated the IEC. By varying the percentage of branching point of the main chain, SG-X, MG-X, and LG-X were prepared with

IEC from 1.47 to 2.1 meq $g^{-1}$. The graft PEMs showed inherent viscosity (IV) from 1.46 to 2.33 dL $g^{-1}$, indicating absence of undesirable crosslinking reaction which could lead to gelation. High tensile strength of 19.19-44.14 MPa was observed for the graft PEMs, owing to the high molecular weight. The mechanical balanced achieved from flexible ether groups in hydrophobic main chain and rigid sulfone groups in hydrophilic side chain induced high percentage strain of 99.57-256.35%, summarized in Table 4.1.

## Morphology

Hydrophilic-hydrophobic nanophase separations of SG-X, MG-X, and LG-X were observed with transmission electron microscopy (TEM) in Figure 4.5. Zebra-shaped nanophase separations were observed in all graft PEMs, exhibiting excellent connectivity. As the IEC increased, the connectivity and the density of hydrophilic domains increased, decreasing the distance between the hydrophilic domains. Different morphologies were observed in graft PEMs with different side chain lengths. Larger hydrophilic domain size was observed with increased side chain length, when compared with similar IECs. The relatively flexible side chain arms containing ion exchange groups aggregate to create hydrophilic domains. In other words, LG-X with long side chain length has more space between the hydrophobic main chain to form aggregation of hydrophilic moieties.

Small-angle X-ray spectroscopy (SAXS) was analyzed for SG-X, MG-X, and LG-X ($IEC_{average}$ ~ 1.54 and 1.94) in Figure 4.6. Peaks observed at 0.2-0.6 $nm^{-1}$ are the matrix knee peaks, which are assumed to be originated from the lamellar spacing, where the d-spacing value is the interval between the hydrophobic crystalline layers. As the IEC increased, the d-spacings decreased due to the denser configuration of hydrophilic domains, as observed in TEM images. SG-X showed smaller d-spacings compared to MG-X and LG-X. Short side chain length resulted in small hydrophilic domain size, ultimately inducing small d-spacings between hydrophobic crystalline layers. SG-X, MG-X, and LG-X were observed with distinct morphologies attributed from the side chain length and the branching point.

## Water sorption behavior

Water uptake and volume change in full humidification were investigated for dimensional stability. Excessive dimensional swelling induces membrane delamination from the catalyst layer, causing serious durability issue. Therefore, adequate amount of water uptake sufficient for effective proton conduction while restricting excessive dimensional change is required.

SG-X, MG-X, and LG-X showed increased water uptake with increase of IEC at

25 °C (Figure 4.7a) and 80 °C (Figure 4.7b). While SG-X showed similar levels of water uptake compared to MG-X at 25 °C, SG-X showed higher levels of water uptake at 80 °C. When SG-1.95 and LG-1.92 of similar IEC were compared for water uptake at 80 °C, SG-1.95 showed higher water uptake of 195.02% than 163.47% of LG-1.92 due to higher hydration number of 55.56 mol $H_2O$ $mol^{-1}$ –$SO_3H$ compared to 47.30 mol $H_2O$ $mol^{-1}$ –$SO_3H$ of LG-1.92.

SG-1.95 showed higher volume change of 118.16% than 70.74% of LG-1.92 at 80 °C (Figure 4.8). The SAXS analysis in Figure 4.6 showed slightly higher increase of d-spacing value (1.19-fold) in SG-1.95 compared to LG-1.92 (1.12-fold) when the membranes were wetted, suggesting greater morphology change in SG-1.95. In addition, the acid concentration [–$SO_3H$] of SG-1.95 (1.16 M) was lower than LG-1.92 (1.23 M) at 25 °C under full immersion in Figure 4.9. Considering SG-1.95 and LG-1.92 have similar IEC, or the hydrophilic content, the water swelled in the membrane would be greater in SG-1.95. These results indicate that short side-chain morphology of SG-X is more affected by water sorption than the long side-chain LG-X.

## Proton transport behavior

Proton is transported through $SO_3H$-bound hydrophilic channels in PEM generated from the hydrophilic/hydrophobic nanophase separation. Insufficient proton transport induces ohmic resistance, reducing performance of PEMFC and PEMWE. The proton transport of the PEM is affected by the acid groups ($-SO_3H$), the water content, and the polymer structure and morphology.

Proton conductivity of SG-X, MG-X, LG-X, and N212 were measured in water, shown in Figure 4.10. The proton conductivity of SG-X, MG-X, and LG-X were higher than 0.105 and 0.189 S $cm^{-1}$ of N212 at 25 °C and 80 °C, respectively.

Below IEC of 1.86 meq $g^{-1}$ at 25 °C, SG-X showed higher proton conductivity (0.128-0.159 S $cm^{-1}$) than LG-X (0.098-0.131 S $cm^{-1}$) in Figure 4.10a.The higher water uptake (67.38-89%) and the hydration number (23.25-26.73 mol $H_2O$ $mol^{-1}$ $–SO_3H$) of SG-X compared to the lower water uptake (51.6-67.89%) and the hydration number (18.49-21.80% mol $H_2O$ $mol^{-1}$ $–SO_3H$) of LG-X induced higher proton conductivity. Above IEC of 1.86 meq $g^{-1}$ at 25 °C, the proton conductivity trend was reversed, where LG-X showed higher proton conductivity (0.17-0.187 S $cm^{-1}$) than SG-X (0.161-0.169 S $cm^{-1}$). Excessive water uptake and dimensional change of SG-X greatly decreased the acid concentration [$–SO_3H$] above IEC of 1.86 meq $g^{-1}$, resulting in decrease of proton conductivity from the acid dilution effect.

Similar proton conductivity tendency was observed below and above the IEC of 1.86 meq $g^{-1}$ at 80 °C in Figure 4.10b. Below IEC of 1.86 meq $g^{-1}$, SG-X showed higher proton conductivity (0.216-0.25 S cm$^{-1}$) than LG-X (0.177-0.224 S cm$^{-1}$), and above IEC of 1.86 meq g$^{-1}$, LG-X showed higher proton conductivity (0.0.26-0.29 S cm$^{-1}$) than SG-X (0.248-0.228 S cm$^{-1}$). At 80 °C, the proton conductivity of SG-1.95 (0.248 S cm$^{-1}$) and SG-2.09 (0.228 S cm$^{-1}$) showed lower proton conductivity than SG-1.85 (0.25 S cm$^{-1}$), despite the higher IEC, suggesting acid dilution effect caused greater influence at higher temperature. LG-X maintained effective proton conductivity even at high temperature and IEC, owing to the low level of water content and the conservation of acid concentration [$-SO_3H$].

Effective proton mobility ($\mu'_{H+}$) as a function of water content ($X_v$) was presented in Figure 4.11. Linear regressions for SG-X, MG-X, and LG-X were calculated, with $R^2$ above 0.98. To remove the effect of acid strengths, the proton mobility at infinite dilution ($X_v$=1.0) was extrapolated, compared with the proton mobility (3.63 × $10^{-3}$ cm$^2$ s$^{-1}$ V$^{-1}$) of free proton in water at 25 °C, infinite dilution. At infinite dilution, the linear regression analysis shows proton mobility of 2.44 × $10^{-3}$ cm$^2$ s$^{-1}$ V$^{-1}$ for SG-X, 2.72 × $10^{-3}$ cm$^2$ s$^{-1}$ V$^{-1}$ for MG-X, and 3.02 × $10^{-3}$ cm$^2$ s$^{-1}$ V$^{-1}$ for LG-X, which are approximately 20% of the proton mobility of free proton. Since SG-X, MG-X, and LG-X share the same chemical structure, the effect of the immobility of the bound $SO_3$- counter-ion, which restricts the mobility of the protons, would be the same. Therefore, the tortuosity regarding the morphology of different side-chain lengths of SG-X, MG-X, and LG-X would affect the proton mobility at infinite dilution. The result suggests that long side-chain graft, LG-X, has more favorable morphology under infinite dilution, being the more appropriate candidate for PEMWE.

Proton transport at reduced humidity depends on the hydration of the PEM, where insufficient hydration level can induce less-developed phase hydrophilic/hydrophobic phase separation. The proton conductivity of SG-X, MG-X, LG-X, and N212 were investigated at 80 °C under reduced humidity of 50% RH (Figure 4.12a) and 80% RH (Figure 4.12b).

Under reduced humidity of 50% RH, N212 showed high proton conductivity of 29.9 mS cm$^{-1}$ despite the low IEC (0.91 meq g$^{-1}$). This suggests N212 was able to maintain high degree of hydration, resulting in proton conducting channels from the hydrophilic/hydrophobic phase separation even at reduced humidification. The hydrocarbon PEMs showed low proton conductivity of 32.9-47.2 mS cm$^{-1}$ for SG-X and 22.5-35.4 mS cm$^{-1}$ for LG-X, possibly from the less-developed phase separation under reduced humidification. SG-X showed higher proton conductivity than LG-X. Comparing hydrocarbon PEMs of similar IEC, SG-1.95 (39.7 mS cm$^{-1}$) was 1.14-fold higher than LG-1.92 (34.8 mS cm$^{-1}$), and SG-2.09 (47.2 mS cm$^{-1}$) was 1.33-fold higher than LG-2.08 (35.4 mS cm$^{-1}$). The higher proton conductivity implies that short side-chain SG-X maintained higher degree of hydration at 50% RH, which could be presumed from higher water uptake and hydration number of

SG-X, as previously discussed.

Under reduced humidity of 80% RH, SG-X, MG-X, and LG-X displayed increased proton conductivity with increased IEC, as in 50% RH. SG-X (139.1-181 mS $cm^{-1}$), MG-X (101.8-180.7 mS $cm^{-1}$), and LG-X (85.7-184.8 mS $cm^{-1}$) showed higher proton conductivity than N212 (69.8 mS $cm^{-1}$) due to higher degree of humidification, enabling better connection between hydrophilic channels in hydrocarbon PEMs. SG-X clearly showed higher proton conductivity than LG-X under IEC of 2.0 meq $g^{-1}$. However, LG-2.08 showed similar proton conductivity of 184.8 mS $cm^{-1}$ compared to 181 mS $cm^{-1}$ of SG-2.09 at higher IEC. Sufficient hydration level and high degree of hydrophilicity induced the high proton conductivity. Since PEMFC is operated at high temperature and low humidity conditions, SG-X, displaying higher proton conductivity at reduced humidification, would be more favorable to PEMFC.

## Hydrogen permeability

Hydrogen permeability is the key parameter in PEMWE regarding the safety and durability. The hydrogen permeability is mainly affected by the diffusion coefficient, solubility, humidification, chemical structure, glass transition temperature ($T_g$), and crystallinity of the polymer. Notably, for PEM, the presence of liquid water and the morphology of hydrophilic/hydrophobic nanophase separation should be considered. The liquid water has higher hydrogen permeability than most of the PEM, and can act as a plasticizer lowering the $T_g$ of PEM. Unlike the proton transport in PEM, hydrogen can permeate through both hydrophilic and hydrophobic domains, and the water-bearing hydrophilic domains are permeated with lower activation energy.

Hydrogen permeability was measured at 80 °C, 100% RH, simulation PEMWE operation, shown in Figure4.13a. N212 showed high hydrogen permeability of 97.46 barrer owing to the highly hydrogen-permeable structure of perfluorosulfonated acid and low $T_g$. The hydrocarbon PEMs showed 1/3 hydrogen permeability for SG-X and 1/4 for LG-X. As the IEC increased, the hydrogen permeability increased, since higher amount of sulfonic acid groups would increase the degree of hydrophilicity, lowering the activation energy of hydrogen permeation. SG-X (24.08-39.48 barrer) showed higher hydrogen permeability than LG-X (21.66-28.38 barrer). Compared at similar IECs, SG-1.95 showed higher hydrogen permeability of 30.34 barrer compared to 24.42 barrer of LG-1.92, and SG-2.09 showed 39.48 barrer compared to 28.38 barrer of LG-2.08. Previously in Figure 4.11, we speculated that LG-X would have less tortuous morphology than SG-X, owing to the higher proton mobility at infinite dilution. Therefore, the higher hydrogen permeability of SG-X is less likely to have originated from the relatively tortuous morphology of hydrophilic domains, but rather from the higher water content observed in Figure 4.7.

Figure of merit (FOM) was drawn to compare the key parameters for PEMWE, dividing the proton conductivity to hydrogen permeability at 80 °C in Figure 4.13b. N212 showed the lowest FOM of 1.94 mS $cm^{-1}$ $barrer^{-1}$ due to the low proton conductivity (0.189 S $cm^{-1}$) and high hydrogen permeability (97.46 barrer). Hydrocarbon PEMs showed higher FOMs, 5.78-9.19 mS $cm^{-1}$ $barrer^{-1}$ for SG-X and 8.17-10.65 mS $cm^{-1}$ $barrer^{-1}$ for LG-X. Below the IEC of 1.6 meq $g^{-1}$, SG-1.61 showed 1.10-fold higher FOM than LG-1.55, owing to the very low proton conductivity (0.177 S $cm^{-1}$) of LG-1.55. Above the IEC of 1.6 meq $g^{-1}$, LG-X exhibited higher FOMs than SG-X. The decrease of FOM in SG-X above the IEC of 1.85 meq $g^{-1}$ resulted from the decrease of proton conductivity by the acid dilution effect. LG-X was less affected by the acid dilution effect, maintaining high FOM. LG-1.95 showed the highest FOM of 10.65 mS $cm^{-1}$ $barrer^{-1}$, owing to the very high proton conductivity (0.29 S $cm^{-1}$) and low hydrogen permeability (24.42 barrer), suggesting LG-X would be a better candidate for PEMWE.

## 4.4. Conclusion

We have conducted investigation on structure-property relationship for aromatic graft PEMs varying the side chain length and the branching point. By varying the side chain length, which affected the morphology, different behaviors on water uptake, dimension change, proton conductivity, and hydrogen permeability were discovered. Graft PEM with short side chain is more suitable for PEMFC from the favorable properties at reduced humidity, and graft PEM with long side chain is more suitable for PEMWE from the excellent properties at hot-water immersed condition.

## 4.5. References

[1] J.M. Thomas, P.P. Edwards, P.J. Dobson, G.P. Owen, Decarbonising energy: The developing international activity in hydrogen technologies and fuel cells, Journal of Energy Chemistry, 51 (2020) 405-415.

[2] H. Nguyen, C. Klose, L. Metzler, S. Vierrath, M. Breitwieser, Fully Hydrocarbon Membrane Electrode Assemblies for Proton Exchange Membrane Fuel Cells and Electrolyzers: An Engineering Perspective, Advanced Energy Materials, 12 (2022) 2103559.

[3] Y. Wang, Y. Pang, H. Xu, A. Martinez, K.S. Chen, PEM Fuel cell and electrolysis cell technologies and hydrogen infrastructure development – a review, Energy & Environmental Science, 15 (2022) 2288-2328.

[4] Y.S. Kim, Polymer Electrolytes with High Ionic Concentration for Fuel Cells and Electrolyzers, ACS Applied Polymer Materials, 3 (2021) 1250-1270.

[5] M. Adamski, N. Peressin, S. Holdcroft, On the evolution of sulfonated polyphenylenes as proton exchange membranes for fuel cells, Materials Advances, 2 (2021) 4966-5005.

[6] D.W. Shin, M.D. Guiver, Y.M. Lee, Hydrocarbon-Based Polymer Electrolyte Membranes: Importance of Morphology on Ion Transport and Membrane Stability, Chemical Reviews, 117 (2017) 4759-4805.

[7] M. Adamski, T.J.G. Skalski, E.M. Schibli, M. Killer, Y. Wu, N. Peressin, B.J. Frisken, S. Holdcroft, Molecular branching as a simple approach to improving polymer electrolyte membranes, Journal of Membrane Science, 595 (2020) 117539.

[8] W.L. Harrison, M.A. Hickner, Y.S. Kim, J.E. McGrath, Poly(Arylene Ether Sulfone) Copolymers and Related Systems from Disulfonated Monomer Building Blocks: Synthesis, Characterization, and Performance – A Topical Review, Fuel Cells, 5 (2005) 201-212.

[9] S.M. Ahn, T.H. Kim, J. Yuk, H.Y. Jeong, D.M. Yu, S.-K. Hong, Y.T. Hong, J.-C. Lee, T.-H. Kim, Perfluorocyclobutyl-containing multiblock copolymers to induce enhanced hydrophilic/hydrophobic phase separation and high proton conductivity at low humidity, Journal of Membrane Science, 641 (2022) 119892.

[10] Y. Li, X. Zhang, G. He, F. Zhang, Sulfonated poly(phenylene sulfide) grafted polysulfone proton exchange membrane with improved stability, International Journal of Hydrogen Energy, 42 (2017) 2360-2369.

[11] K. Kim, B.-K. Jung, T. Ko, T.-H. Kim, J.-C. Lee, Comb-shaped polysulfones containing sulfonated polytriazole side chains for proton exchange membranes, Journal of Membrane Science, 554 (2018) 232-243.

[12] N. Li, C. Wang, S.Y. Lee, C.H. Park, Y.M. Lee, M.D. Guiver, Enhancement of Proton Transport by Nanochannels in Comb-Shaped Copoly(arylene ether sulfone)s, Angewandte Chemie International Edition, 50 (2011) 9158-9161.

**Table 4.1.** General properties of SG-X, MG-X, LG-X, and N212

| **Samples** | **Side chain MW (g mol$^{-1}$)** | **Branching point of main chain (%)** | **IEC (meq g$^{-1}$)** | **Inherent viscosity (dL g$^{-1}$)** | **Tensile strength (MPa)** | **Percentage strain (%)** |
|---|---|---|---|---|---|---|
| **SG-1.61** | 7800 | 3.44 | 1.61 | 2.05 | 38.76 | 117.52 |
| **SG-1.85** | | 3.76 | 1.85 | 1.66 | 31.50 | 99.57 |
| **SG-1.95** | | 4.37 | 1.95 | 2.28 | 30.73 | 256.35 |
| **SG-2.09** | | 5.05 | 2.09 | 2.33 | 36.76 | 123.26 |
| **MG-1.47** | 11000 | 1.93 | 1.47 | 1.66 | 37.03 | 155.76 |
| **MG-1.95** | | 3.09 | 1.95 | 1.5 | 31.99 | 129.97 |
| **MG-2.1** | | 3.40 | 2.1 | 1.46 | 19.19 | 115.70 |
| **LG-1.55** | 15000 | 1.37 | 1.55 | 1.55 | 44.14 | 171.87 |
| **LG-1.73** | | 1.76 | 1.73 | 1.68 | 33.18 | 136.18 |
| **LG-1.92** | | 2.21 | 1.92 | 1.72 | 26.30 | 201.76 |
| **LG-2.08** | | 2.38 | 2.08 | 2.02 | 38.94 | 128.24 |
| **N212** | - | - | 0.91 | - | 27.67 | 540.81 |

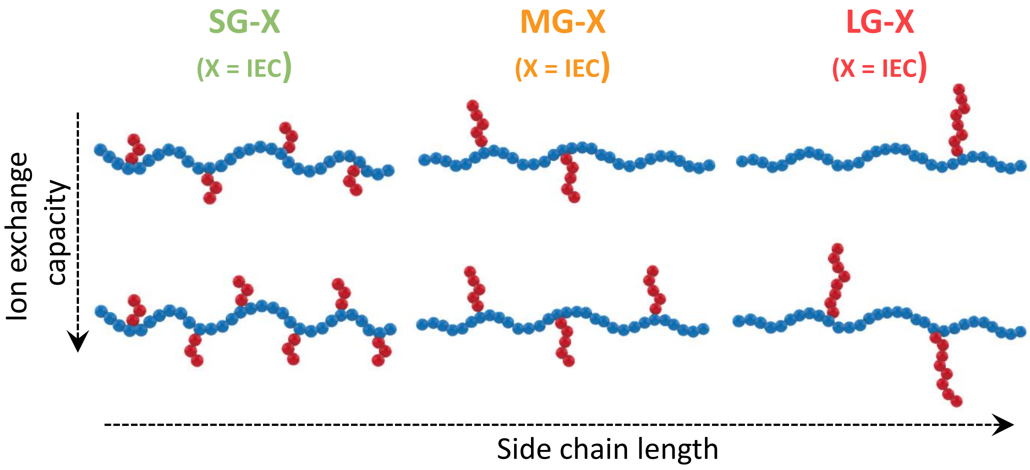

**Figure 4.1.** Schematic drawing of SG-X, MG-X, and LG-X

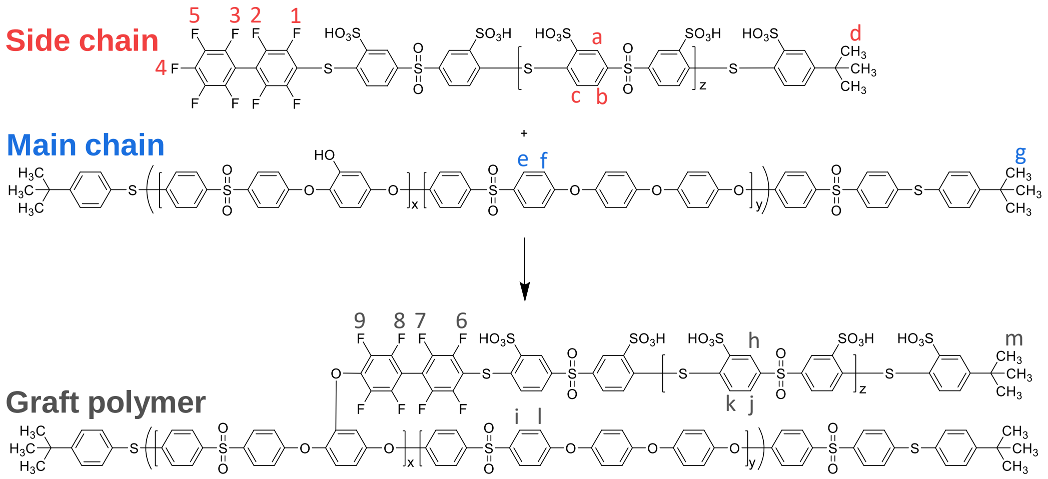

**Figure 4.2.** Synthesis of aromatic graft polymer where hydrophilic side chain is grafted to hydrophobic main chain

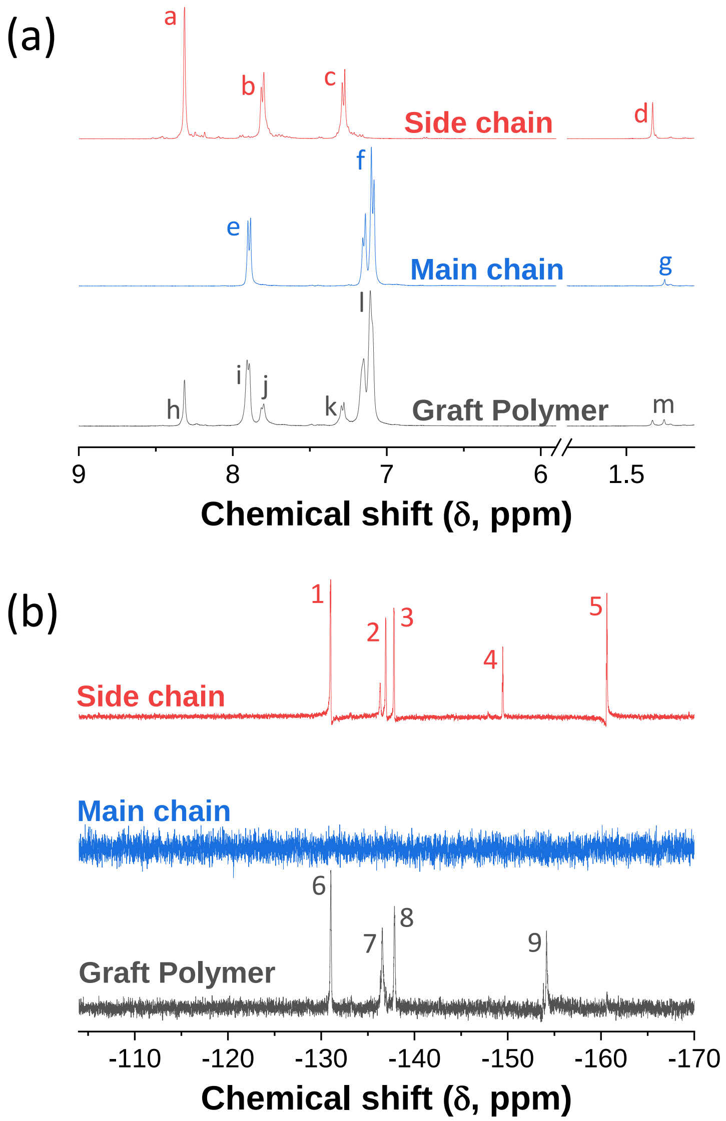

**Figure 4.3.** (a) $^{1}$H and (b) $^{19}$F NMR of side chain, main chain, and graft polymer

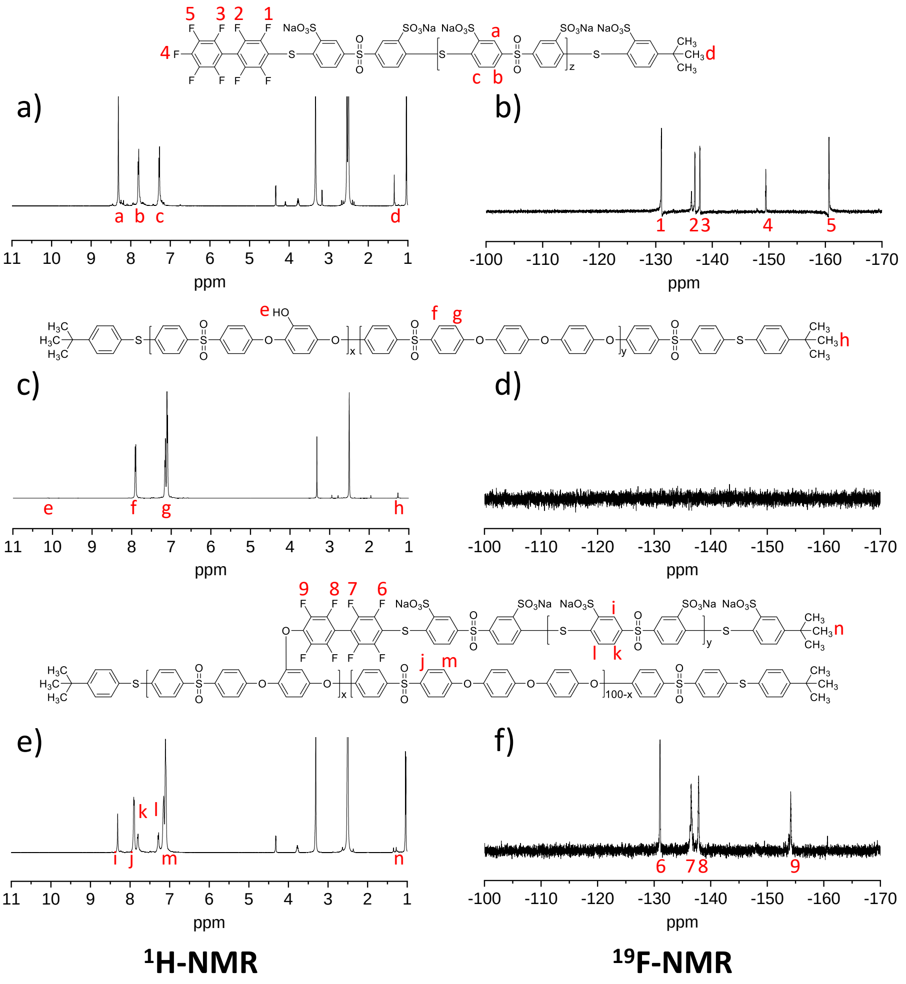

**Figure 4.4.** $^{1}$H NMR of (a) hydrophilic side chain, (b) hydrophobic main chain, and (c) graft polymer; $^{19}$F NMR of (d) hydrophilic side chain, (e) hydrophobic main chain, and (f) graft polymer

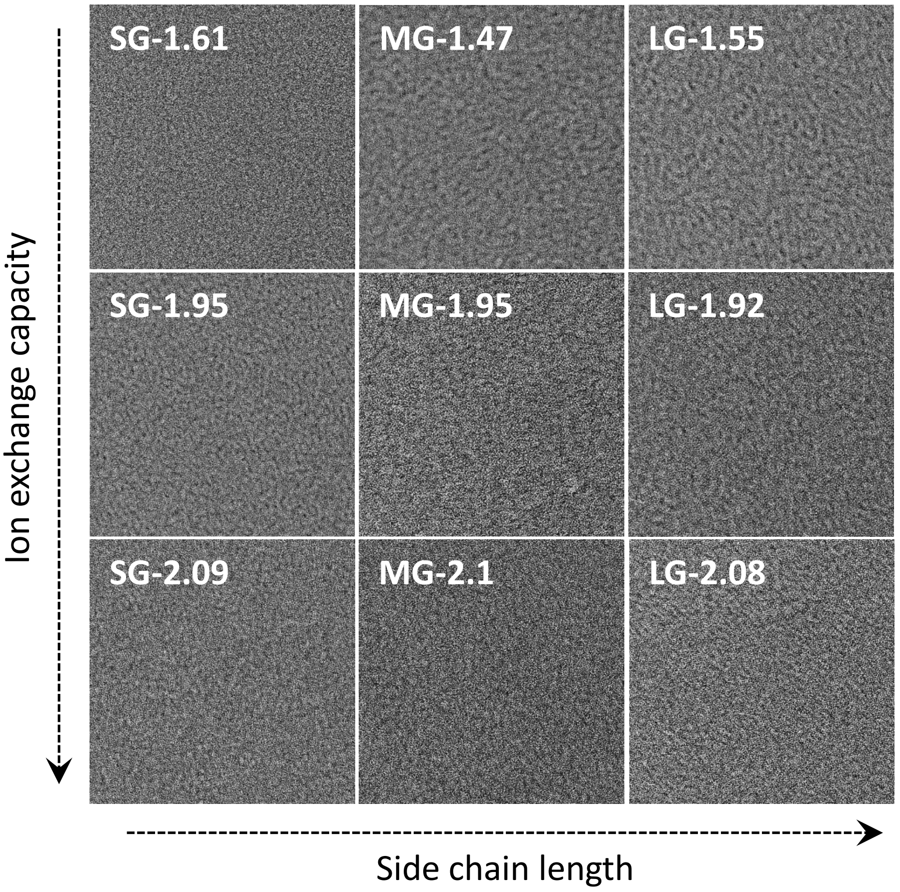

**Figure 4.5.** Lead-stained TEM images of SG-X, MG-X, and LG-X under 50 nm scale (The dark and light domains represent hydrophilic and hydrophobic moieties, respectively.)

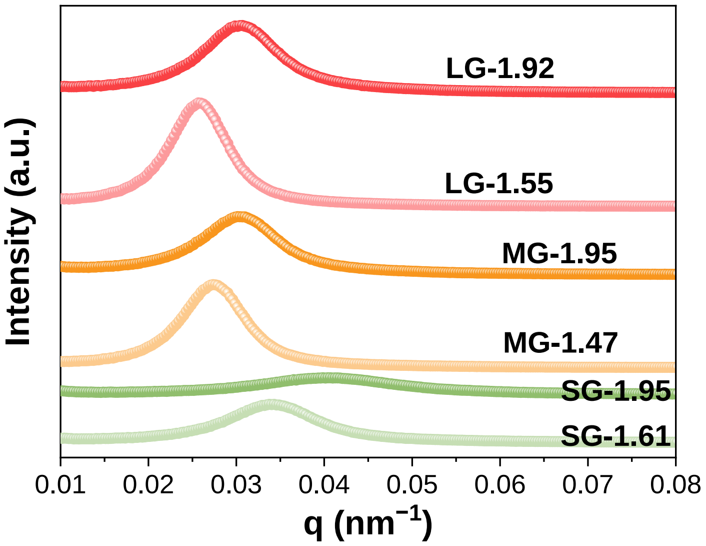

| | d-spacing value (nm), Matrix knee |
|---|---|
| LG-1.92 | 20.47 |
| LG-1.55 | 24.45 |
| MG-1.95 | 20.84 |
| MG-1.47 | 22.96 |
| SG-1.95 | 15.76 |
| SG-1.61 | 18.31 |

**Figure 4.6.** SAXS spectra of SG-1.61, SG-1.95, MG-1.47, MG-1.95, LG-1.55, and LG-1.92 at dried state

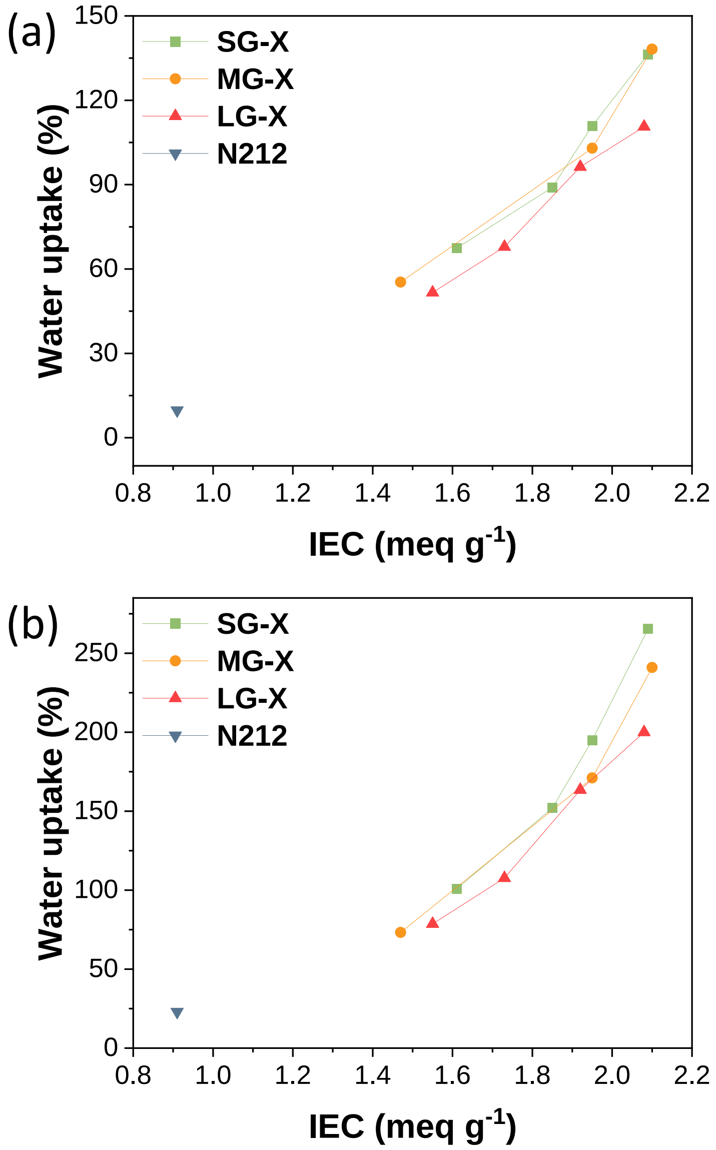

**Figure 4.7.** Water uptake of SG-X, MG-X, LG-X, and N212 at (a) 25 °C and (b) 80 °C immersed in water

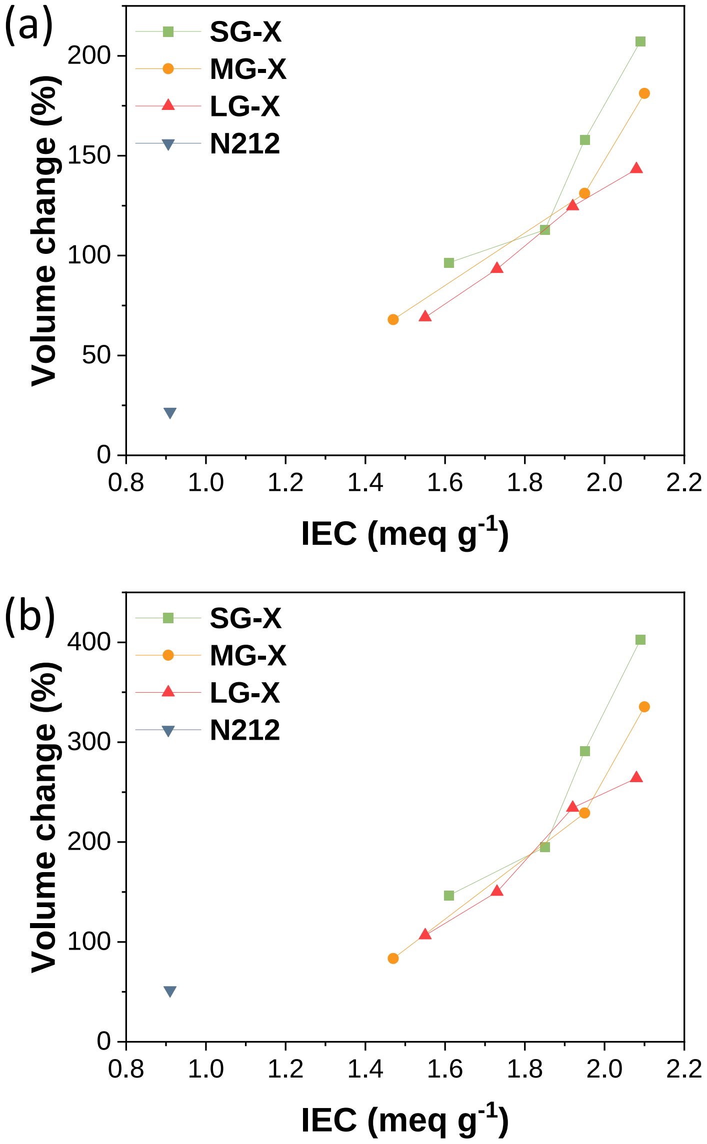

**Figure 4.8.** Volume change of SG-X, MG-X, LG-X, and N212 at (a) 25 °C and (b) 80 °C immersed in water

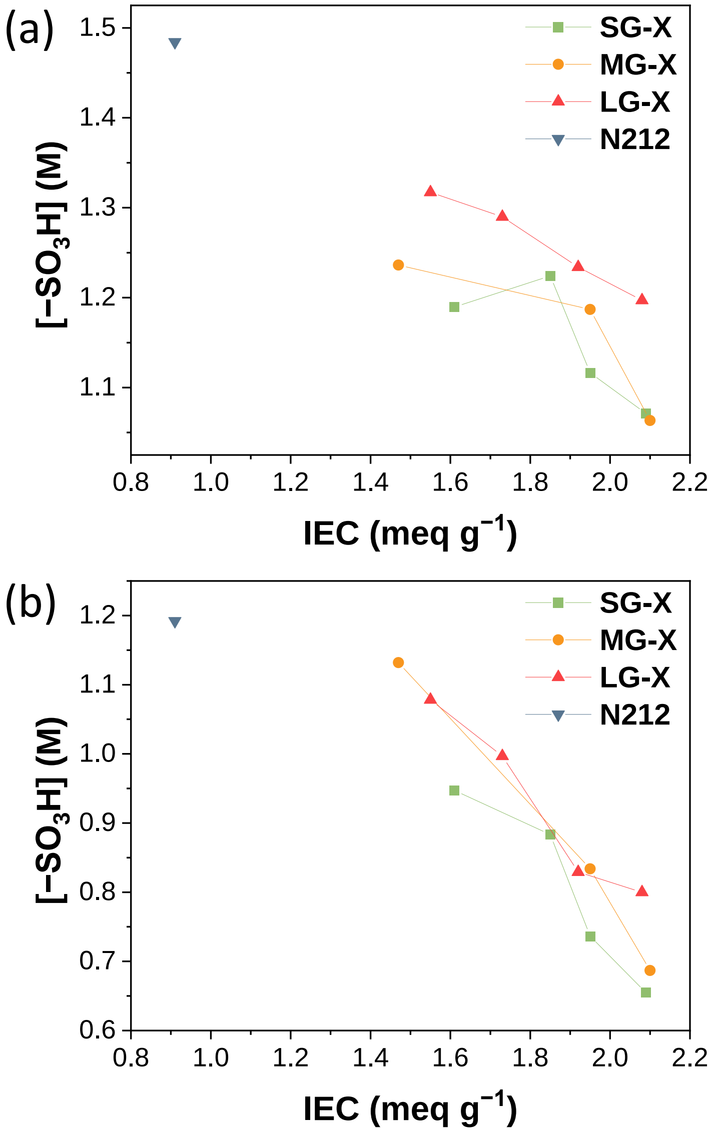

**Figure 4.9.** Acid concentration [–SO$_3$H] of SG-X, MG-X, LG-X, and N212 at (a) 25 °C and (b) 80 °C immersed in water

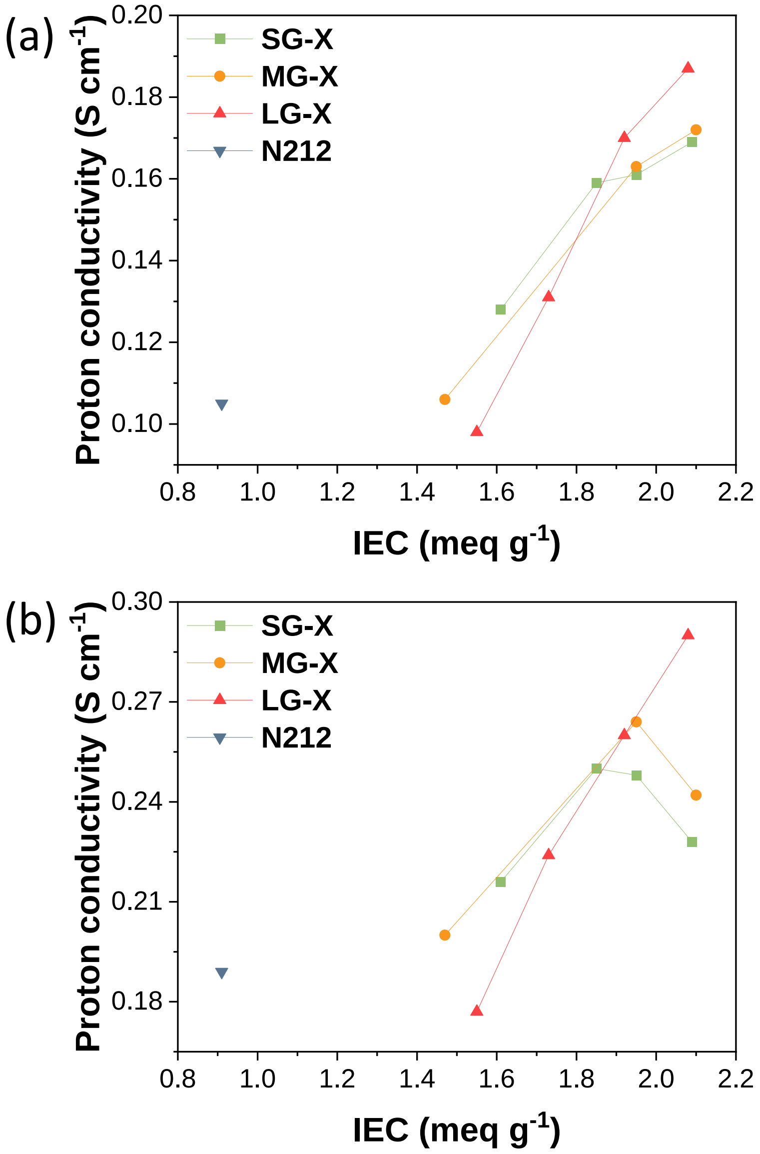

**Figure 4.10.** Proton conductivity of SG-X, MG-X, LG-X, and N212 at (a) 25 °C and (b) 80 °C immersed in water

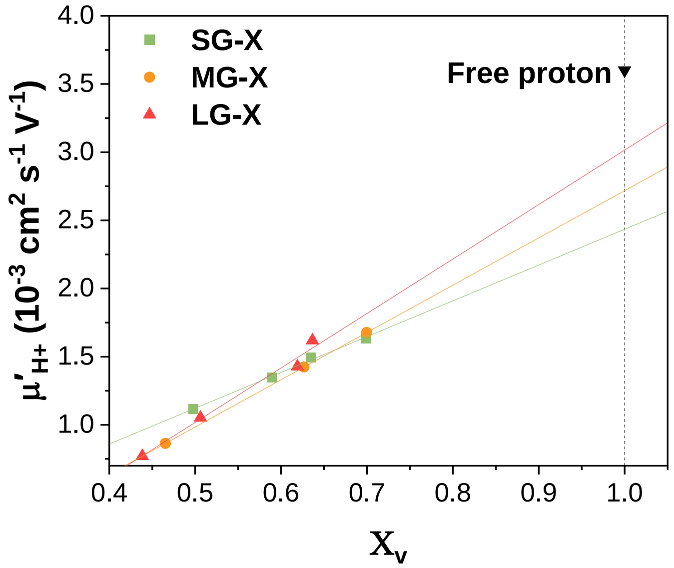

| | $\mu'_{H+}$ at $X_v$ =1.0 ($10^{-3}$ $cm^2$ $s^{-1}$ $V^{-1}$) |
|---|---|
| **SG-X** | 2.44 |
| **MG-X** | 2.72 |
| **LG-X** | 3.02 |
| **Free proton in water at infinite dilution at 25 °C** | 3.63 |

**Figure 4.11.** Calculated proton mobility values ( $\mu_{H+}$) as a function of water content ($X_v$) at infinite dilution ($X_v$=1.0)

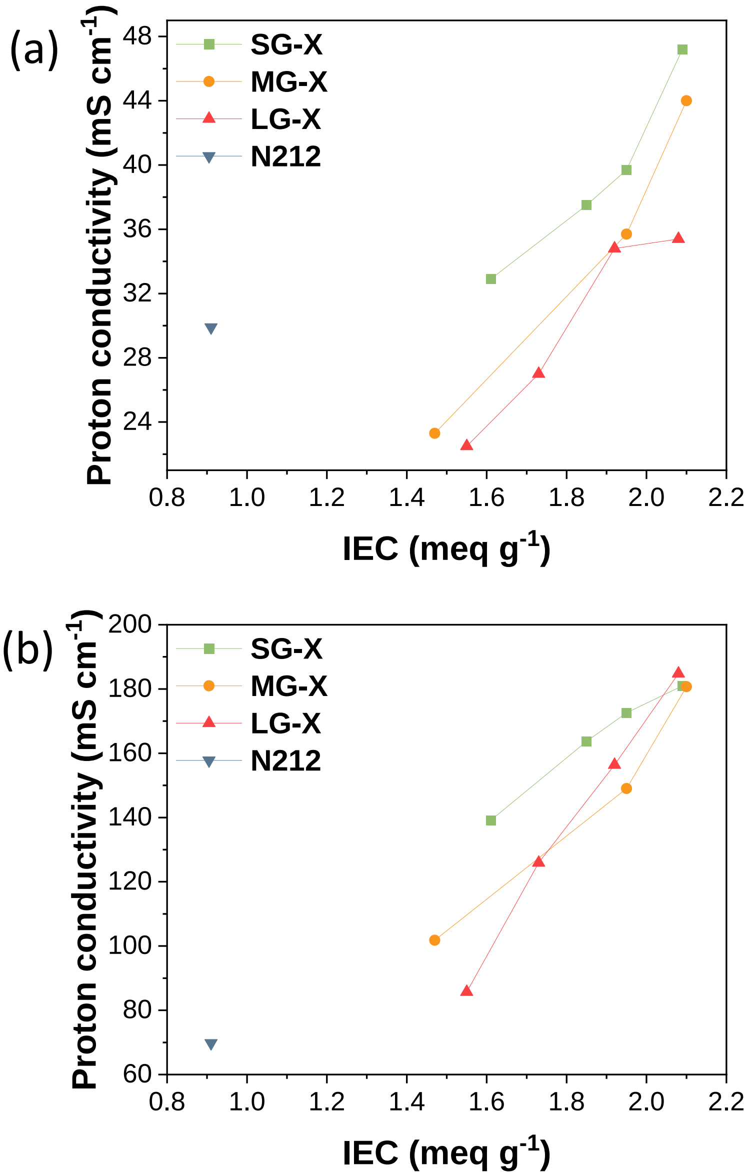

**Figure 4.12.** Proton conductivity of SG-X, MG-X, LG-X, and N212 at 80 °C, reduced humidity of (a) 50% RH and (b) 80% RH

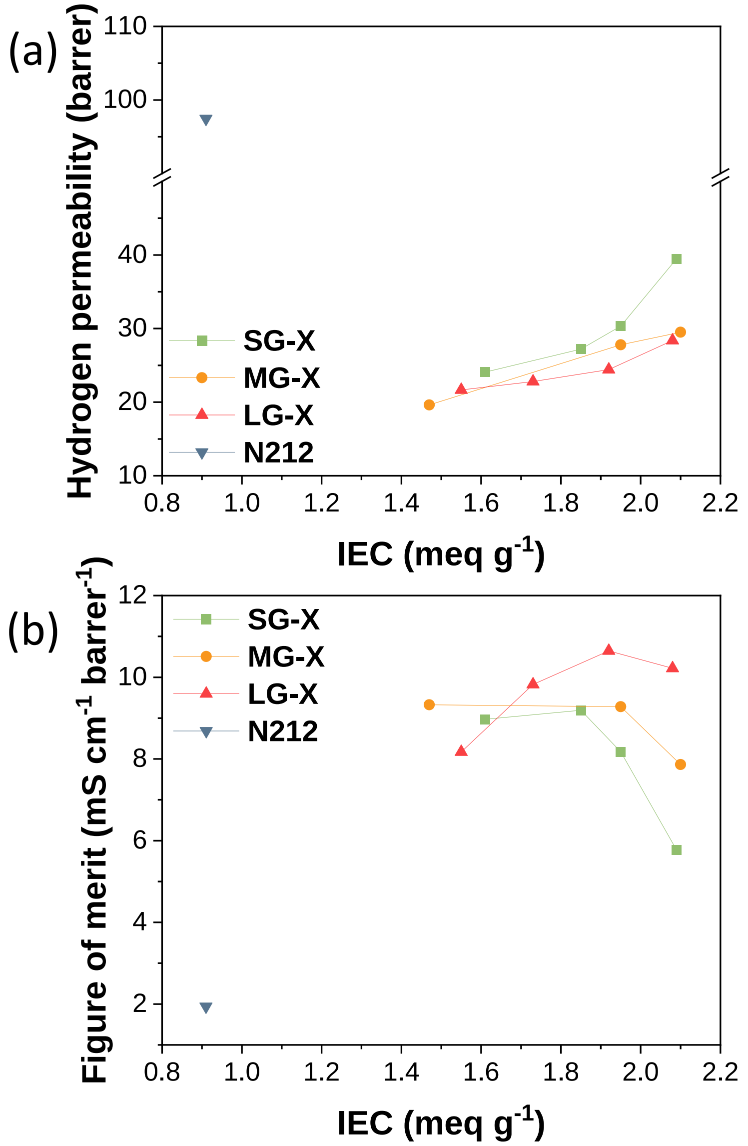

**Figure 4.13.** (a) Hydrogen permeability of SG-X, MG-X, LG-X, and N212 at 80 °C, 100% RH. Hydrogen permeability was detected through a gas chromatography where the humidified hydrogen gas was supplied to one side of the PEM (b) Figure of merit (FOM) of SG-X, MG-X, LG-X, and N212 at 80 °C

# 초 록

본 연구에서는 기 보고된 수소 이온 교환 막 연료 전지 및 수전해용 탄화수소계 이온 교환 막의 친수성-소수성 나노 상 분리를 개선하기 위한 연구를 진행하였다. 첫째, 고도로 술폰화된 폴리(페닐렌 설파이드 술폰) 친수성 올리고머 및 부분적으로 불소화된 퍼플루오로사이클로부틸 (PFCB) 함유 소수성 올리고머를 가진 멀티블록 공중합체를 합성하였다. 친수성 부분과 소수성 부분 사이의 뚜렷한 대조는 매우 발달된 상 분리를 유도하였으며, 이는 이온 교환 막 내의 투과 전자 현미경 이미지에서 관찰되었다. 유연한 에테르기 및 PFCB 기에서 증가된 고분자 사슬 이동성은 어닐링의 용이성을 증가시켰다. 어닐링은 소수성 부분의 폴리머 사슬 패킹을 유도하여 친수성-소수성 나노 상 분리를 향상시켰다. 제조된 PFCB 함유 멀티블록형 이온 교환 막은 기존의 탄화수소계 랜덤형 이온 교환 막에 비해 높은 이온 전도도를 나타냈으며 과도한 치수 팽창이 억제되었다. 또한, 낮은 가습 (상대 습도 50%) 조건에서 최대 41.9 mS $cm^{-1}$의 높은 이온 전도도를 보였다. 32.7 mN $cm^{-1}$ 의 높은 접착 강도도 관찰되었으며, 이는 막 전극 집합체에 사용하는 과불소계 바인더와 구조적 친화성을 증가시켜 강한 계면 호환성을 달성했다. 향상된 친수성-소수성 나노 상 분리는 안정적인 화학적 및 물리적 내구성을 달성하는 것 외에도 100% 및 50% 상대 습도 조건에서 각각 1.13 및 0.61 A $cm^{-2}$ (0.6 V, 65 ° C)의 연료 전지 성능을 달성하였다.

둘째, 고도로 술폰화된 폴리(페닐렌 설파이드 술폰) 측쇄를 폴리(아릴렌 에테르 술폰) 주쇄에 그라프팅하여 좁고 매우 연결된 나노 상 분리를 생성함으로써 방향족 그라프트형 양이온 교환 막을 합성하였다. 그라프트형 이온 교환 막의 독특한 형태학적 물성은 연결성이 우수한 친수성 채널로 인해 높은 이온 전도도를 유지하게 하였고 적절한 도메인 크기로 인해 낮은 수소 투과도를 유발하였다. 또한 그라프트형 이온 교환 막은 우수한 치수 안정성, 기계적 강도 및 열 가수 분해 안정성을 보였다. 수전해 구동에서 과불소계 나피온 212 보다 1.9 V 에서 1.88 배 높은 5300 mA $cm^{-2}$ 의 성능을 보였고 고 전류 밀도 (1 A $cm^{-2}$) 에서 50 시간 동안 전압 손실 없이 높은 내구도를 보였다.

마지막으로, 양이온 교환막 연료 전지 및 수전해 응용을 위해 방향족 탄화수소계 그라프트형 이온 교환 막에 대한 구조-물성 관계에 대한 조사가 수행되었다. 측쇄 길이와 밀도를 최적화하여 연료 전지 적용을 위한 저가습 조건 및 수전해 적용을 위한 고온 물 침지 조건에서 이온 교환 막의 특성에 미치는 영향을 연구하였다. 짧은 측쇄를 가진 그라프트형 이온 교환 막은 저가습 조건에서 높은 이온 전도도를 보이므로 연료 전지 적용에서 보다 유리할 수 있다. 긴 측쇄를 가진 그라프트형 이온 교환 막은 고온 물 침지 조건에서 낮은 팽윤 특성과 수소 투과도를 보이므로 수전해 적용에서 보다 유리할 수 있다.

**주요어: 양이온 교환 막, 친수성-소수성 상 분리, 양이온 교환 막 연료전지, 양이온 교환 막 수전해, 멀티블록 공중합체, 그라프트 공중합체**

**학 번** : 2018-32408